Spectroscopy of Xenon and Xenon-Noble Gas Mixtures for Bose-Einstein Condensation of Vacuum-Ultraviolet Photons

Dissertation
zur
Erlangung des Doktorgrades (Dr. rer. nat.)
der
Mathematisch-Naturwissenschaftlichen Fakultät
der
Rheinischen Friedrich-Wilhelms-Universität Bonn

vorgelegt von

Thilo Falk vom Hövel
aus
Bergisch Gladbach

Bonn 2023

Angefertigt mit Genehmigung der Mathematisch-Naturwissenschaftlichen Fakultät
der Rheinischen Friedrich-Wilhelms-Universität Bonn

1. Gutachter:	Prof. Dr. Martin Weitz
2. Gutachter:	Prof. Dr. Stefan Linden

Tag der Promotion:	15.12.2023
Erscheinungsjahr:	2024

Abstract

Bose-Einstein condensation of photons has first been observed in 2010 by the group of Martin Weitz in Bonn. In the experimental scheme, a photon gas is confined to a wavelength-size microcavity filled with a liquid dye solution that exhibits a thermally equilibrated rovibronic level structure. The photon gas is subject to a thermal contact with the dye solution via repeated absorption and reemission cycles; thereby it is driven into thermal equilibrium. Once the photon number exceeds the system's critical particle number, condensation sets in, with the ground state energy corresponding to the microcavity's low-frequency cutoff, typically equivalent to around 580 nm wavelength. Besides other intriguing properties, a Bose-Einstein condensate of photons is a source of coherent and monochromatic light circumventing the need for an optically inverted active medium, setting it apart from a laser. Accordingly, a realization in the vacuum-ultraviolet spectral regime (100 nm − 200 nm wavelength) appears particularly alluring, as here the construction of lasers is difficult due to the high pump powers required to achieve population inversion.

The present thesis aims at the exploration of xenon as a thermalization mediator for such an application, with this heaviest of all stable noble gases exhibiting a transition wavelength of 146.9 nm on its $5p^6 \rightarrow 5p^5 6s$ transition. In dense environments, this gas forms transient quasimolecules, replicating several features of dye molecules, such as the emergence of a quasimolecular manifold of energetic sublevels and an associated Stokes shift between the spectral profiles of absorption and emission. Experimental results of two-photon excitation spectroscopy of the $5p^6 \rightarrow 5p^5 6p$ and $5p^5 6p'$ transitions are reported, aiming at the identification of suitable pumping schemes for future vacuum-ultraviolet photon condensates. Both the gaseous and supercritical phases are covered, with sample pressures as high as 95 bar. Additionally, results of an experimental scheme are presented, devised to increase the reabsorption of light emitted on the strongly red-shifted second excimer continuum around 172 nm wavelength by providing an auxiliary visible-spectral-range photon field. Corresponding absorption measurements involving a nondegenerate driving of the $5p^6 \rightarrow 5p^5 6p$ two-photon transitions are reported.

Further, results on the spectroscopy of mixtures between xenon and any of the other stable noble gases are presented; such heteronuclear mixtures are considered an alternative candidate for a thermalization mediator. In the samples explored here, xenon contributions are relatively small, around 100 ppm of total sample pressures of up to 90 bar. For such samples, absorption and emission spectra are investigated with particular emphasis on the influence of varying xenon and noble gas contributions. The fulfillment of the Kennard-Stepanov relation is assessed, an important indicator for the suitability of a medium as thermalization mediator for photons.

List of Publications

Publications of the author with particular relevance for the contents of the present thesis:

- T. vom Hövel, F. Huybrechts, E. Boltersdorf, C. Wahl, F. Vewinger, and M. Weitz, *Two-photon excitation and absorption spectroscopy of gaseous and supercritical xenon*, Phys. Rev. A **108**, 012821 (2023)

Further publications related to the present thesis:

- T. Ockenfels, P. Roje, T. vom Hövel, F. Vewinger, and M. Weitz, *Spectroscopy of high-pressure rubidium-noble-gas mixtures*, Phys. Rev. A **106**, 012815 (2022)
- C. Wahl, M. Hoffmann, T. vom Hövel, F. Vewinger, and M. Weitz, *Vacuum-ultraviolet absorption and emission spectroscopy of gaseous, liquid, and supercritical xenon*, Phys. Rev. A **103**, 022831 (2021)

Contents

1 Introduction

Spectroscopy has a long and rich history. Two millennia ago, the Romans observed that a stone found on an island in the Red Sea has the ability to project the colors of a rainbow onto a nearby wall, when illuminated by sunlight [1]. This particular stone was dubbed *iris*, presumably honoring the goddess of the rainbow. Judging from the stone's description, it is likely that it was a naturally-formed prism. Sir Isaac Newton is generally credited with laying the foundations of modern spectroscopy in the 17$^{\text{th}}$ century, although other scientists had investigated the light emitted by the sun before him [2]. Around 1670, Newton not only observed that a prism can separate white light into its constituents; he also discovered the inverted process, combining light of distinct colors to white light [3, 4]. He is generally regarded as the first to use the word *spectrum*. Around 1815, Joseph von Fraunhofer tremendously advanced the field of spectroscopy by introducing a diffraction grating and performing a systematic investigation of the solar spectrum with it [5]. In the otherwise continuous spectrum, he observed a series of suppressed bands at distinct spectral positions, many of which result from absorption in the outer regions of the sun, the so-called photosphere. To this day, these lines are referred to as Fraunhofer lines, although they had already been observed 13 years earlier by William Wollaston [6]. He, however, attributed them to natural boundaries between the different colors of light.

This brief (and by no means complete) glimpse at the origins of spectroscopy contrasts with the relatively young existence of Bose-Einstein condensation, the centenary of whose prediction is yet to be marked. In 1924, Satyendranath Bose sent an article to Albert Einstein [7], in which he used quantum statistics of photons to derive Planck's law. Impressed by Bose's derivation, Einstein translated the work into German language and published it under the title "Plancks Gesetz und Lichtquantenhypothese" (Planck's law and the hypothesis of light quanta) [8]. He further extended the novel approach to *atomic* gases and published a quantum theory of monoatomic ideal gases [9, 10]. In it, he states that upon increasing the particle density, at a low (but finite) temperature, a "condensation" of particles into the energetic ground state occurs [11]:

> I assert that in this case a steadily growing number of molecules compared to the total density will go over into the 1$^{\text{st}}$ quantum state (state without kinetic energy). [...] A separation sets in; one part ≪condenses,≫ the rest remains a ≪saturated ideal gas.≫

Interestingly enough, Einstein himself was doubtful about the feasibility of an experimental observation of this effect. Indeed, after this theoretical prediction it took about seven decades until a Bose-Einstein condensate could be realized. Only after the advent of lasers in the 1960s

[12, 13] and associated cooling techniques for matter in the 1970s [14] sufficiently elevated phase space densities could be reached. In July of 1995, scientists around Eric Cornell and Carl Wieman were able to cool a gas of rubidium-87 atoms to a temperature of only 170 nK, allowing them for the first time to observe a Bose-Einstein condensate experimentally [15]. Only a few months later, in November of 1995, scientists around Wolfgang Ketterle achieved a Bose-Einstein condensate of sodium-23 atoms [16]. Ever since, Bose-Einstein condensation has been realized in many different systems. In addition to a wide range of atomic species [17–19], it was observed in molecules [20, 21] and quasiparticles such as magnons [22] and exciton-polaritons [23, 24]. In the realization of Bose-Einstein condensates of atomic gases, photons played an outstanding role, as the cooling of atomic gases would not have been possible without light-involving techniques such as laser cooling. Hence, it suggests itself to wonder whether Bose-Einstein condensation can also be achieved in a photon gas. Due to vanishing interparticle interaction, this represents the closest real-world approximation to an ideal Bose gas. It appears logical to begin the contemplation of photon Bose-Einstein condensation at black-body radiation, the arguably most ubiquitous photon gas, in which the mean spectral density n of a state of frequency ω is solely determined by the temperature T of the emitter [25],

$$n\left(\omega, T\right) = \frac{u\left(\omega, T\right)}{\hbar\omega} = \frac{\omega^2/\pi^2 c^3}{\exp\left(\frac{\hbar\omega}{k_\mathrm{B}T}\right) - 1} \,.$$

Here, $u\left(\omega, T\right)$ corresponds to the spectral energy density (Planck's law [26]). Due to the nature of its provenance from thermal emitters, black-body radiation is inherently in thermal equilibrium. Integrating over all possible frequencies, though, one finds the system's total particle number to be a monotonous function of the ensemble temperature,

$$\frac{N}{V} = \int_0^\infty n(\omega, T)\mathrm{d}\omega = \frac{2\zeta(3)}{\pi^2}\left(\frac{k_\mathrm{B}}{\hbar c}\right)^3 T^3 \;\to\; 0 \quad \text{for} \quad T \;\to\; 0\,.$$

Clearly, upon approaching the system's energetic ground state ($T \to 0$), no photons would be left to undergo a phase transition into the Bose-Einstein condensate (the photons vanish in the walls of the black body). This line of arguing illustrates that Bose-Einstein condensation is not possible in a photon gas governed by the statistics of black-body radiation [27].

It becomes apparent that for the experimental realization of a Bose-Einstein condensate of photons, both a nontrivial energy ground state and, due to the lack of interaction, a particle-number conserving thermalization process need to be introduced. Early work from around the turn of the millennium envisaged the confinement of photons in a nonlinear Fabry-Perot resonator [28], attempting to introduce a thermalization mechanism via four-wave mixing in photon-photon collisions. Although promising, these attempts did not lead to the experimental observation of a Bose-Einstein condensate of photons. It was a different approach by the group of Martin Weitz in Bonn, that in 2010 led to the observation of a thermalized photon gas [29] and the

observation of a Bose-Einstein condensate of photons shortly after [30]. The centerpiece of these experiments is a high-finesse optical microcavity with a concave mirror topography and a mirror spacing in the order of the optical wavelength of the light confined therein. The standing-wave condition imposes a low-energy cutoff wavelength, providing a nontrivial energy ground state for the photons to condense into. Thermalization of the photon gas is achieved by filling the microcavity with a liquid dye solution, which fulfills the thermodynamic Kennard-Stepanov relation. This links the spectral profiles of absorption and emission by a Boltzmann-like frequency scaling, indicating a thermalized occupation distribution of the dye molecules' rotational and vibrational (rovibronic) levels. In repeated absorption and reemission cycles, the photons are brought into thermal contact with the dye solution and thermalize to its temperature (usually room temperature). Typical cutoff energies in these experiments correspond to wavelengths around 580 nm, with the thermal tail of the energy distribution (comprising the modes energetically above the ground state) extending over multiple thermal energy units $k_\mathrm{B}T$. Based on this experimental platform, various studies have been conducted, such as on calorimetry [31], coherence [32] and the properties of thermalized and condensed photon gases in bespoke potential landscapes [33–35]. Microcavity-based photon Bose-Einstein condensation has also been realized in experiments at Imperial College [36], Utrecht University [37] and University of Twente [38]. Moreover, Photon Bose-Einstein condensation has been observed in semiconductor systems [39, 40] and fibers [41].

A Bose-Einstein condensate of photons serves as a source of coherent optical emission without the need for a population inversion [32], setting it apart from a usual laser. Correspondingly, its realization in the vacuum-ultraviolet spectral regime (VUV; 100 nm − 200 nm) appears particularly alluring. In this wavelength range, it is notoriously difficult to operate (continuous-wave) lasers [42, 43] due to the required high pump intensities, as electronic states' radiative lifetimes scale as $1/\omega^3$, with ω the optical frequency. To extend the wavelength range of photon Bose-Einstein condensates from the presently accessible visible spectral range to the vacuum-ultraviolet, though, a different thermalization medium needs to be identified, as dye molecules can no longer be employed due to a lack of suitable transitions. In previous work [44, 45] by Christian Wahl, the use of xenon was suggested, whose $5p^6 \rightarrow 5p^5 6s$ transition at a wavelength of 146.9 nm lies squarely in the VUV. In dense xenon samples (with pressures above a few hundred millibars), the atoms can no longer be treated individually and the formation of transient quasimolecules of two atoms is energetically favored. These exhibit an energetic level substructure resembling that of dye molecules, leading to a Stokes-shifted emission around 172 nm. Exploring xenon samples in the gaseous, supercritical and liquid phases, the fulfillment of the Kennard-Stepanov relation was validated [46], fulfilling an important requirement of a prospective thermalization medium in experiments on photon Bose-Einstein condensation. With this, xenon can generally be considered a suitable candidate for a thermalization medium for the Bose-Einstein condensation of VUV photons. Yet, another key finding was that the large Stokes shift between absorption and emission of around 25 nm leads to a low absorption strength in the emission wavelength region. In a future xenon-filled microcavity (which would exhibit a much smaller finesse than current

ones in the visible spectral range), this would prevent the occurrence of multiple repeated cycles of absorption and reemission during the photon storage time, impeding sufficient thermal contact between a photon gas and the thermalization medium.

The experimental work of the present thesis continues the exploration of xenon as a thermalization medium. The main focus lies on the identification of suitable conditions for an increased spectral overlap between the absorption and emission profiles in xenon environments. This can broadly be separated into two approaches. One approach envisages a bridging of the energetic gap between the absorption and the emission transitions by providing an auxiliary photon field. The other approach involves the exposure of the xenon gas to an environment of another noble gas; such mixtures are reported to exhibit a reduced Stokes shift compared to pure-xenon samples. Furthermore, with regard to future experiments with a photon gas confined to a xenon-filled microcavity, an exploration of the most efficient excitation wavelengths has been conducted.

Structure of the Present Thesis

This thesis begins with an introduction into the principles of photon Bose-Einstein condensation in Chap. 2. Here, both the implementation of a system with a nontrivial energy ground state and the establishment of a thermalization mechanism for the photons will be covered. The thermodynamic Kennard-Stepanov relation will be derived and its relevance for the thermalization of photons will be illuminated. Subsequently, Chap. 3 will give an overview about the physics of diatomic quasimolecules, as relevant for the context of this work. Particular attention will be dedicated to the noble gas xenon, as samples based on this element are currently considered the most promising candidate as a thermalization medium for photons in the VUV. Chapter 4 will present the experimental environment, as used for the measurements presented throughout this work; including first characterizing measurements of key experimental platforms. Experimental results on two-photon spectroscopy of xenon's UV-transitions will be presented in Chap. 5, probing excitation mechanisms and the above-mentioned scheme to increase the reabsorption probability for photons emitted by the xenon system. Experimental results of spectroscopic investigations of xenon-noble gas mixtures, a different candidate system, will be presented in Chap. 6. The thesis closes with a conclusion and an outlook on the possible future of these experimental endeavors in Chap. 7.

2 Bose-Einstein Condensation of Photons

As already outlined in the introductory chapter, two major conceptual challenges need to be addressed for the realization of a Bose-Einstein condensate of photons. First, a platform is needed that can provide a nontrivial energy ground state for the photons to condense into. Second, a particle number-conserving thermalization process is needed, as the emergence of Bose-Einstein condensation is restricted to particle ensembles in thermal equilibrium. In this chapter, the approach to address both challenges for the case of *visible* photons will be presented, following the original treatise by Jan Klärs [47]. This will lay the conceptual groundwork for an understanding of the approach adopted for vacuum-ultraviolet photons, which will be presented in the subsequent chapter.

2.1 A Two-Dimensional Quantum Gas of Light

At the heart of experiments on photon Bose-Einstein condensation is a microcavity consisting of two highly reflective mirrors. This platform effectively leads to a two-dimensional environment for the photons; the corresponding dispersion relation will be derived in the following, illustrating how in this system a nontrivial energy ground state is created. Subsequently, the statistics of ideal Bose gases will be invoked to calculate the system's critical particle number as the threshold above which condensation occurs.

2.1.1 Dispersion Relation of Photons in a Microcavity

The typical experimental platform for the observation of Bose-Einstein condensation of photons is a microcavity consisting of two concave, mutually facing mirrors with a spacing in the order of 1 µm, as shown in Fig. 2.1(a). A photon of frequency ω confined to such a microcavity has the energy

$$E = \hbar\omega = \frac{\hbar c}{n}\sqrt{k_r^2 + k_z^2}\,, \tag{2.1}$$

where $\hbar$ is the reduced Planck constant, n is the refractive index of the medium inside the microcavity and $k_r = |\vec{k_r}|$ and k_z denote the transversal and longitudinal photon wave vectors, respectively. The photons are subject to standing-wave boundary conditions imposed by the mirrors, such that the longitudinal wave vector can be written as

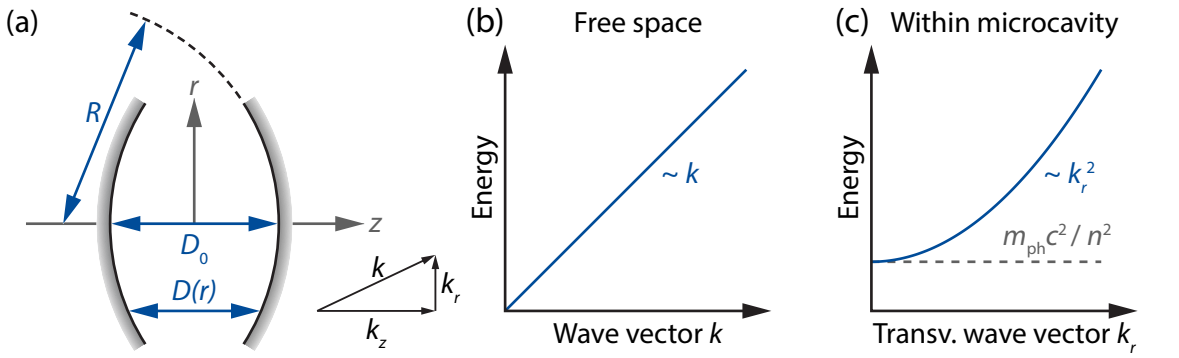

Figure 2.1: Microcavity environment – **(a)** Sketch of the microcavity geometry, constituted by two concave mirrors with a radius of curvature R and separated by a distance D_0 on the optical axis. **(b)** Linear dispersion relation of photons in free space. With the photon energy being proportional to the wave vector, only a trivial ground state with vanishing energy exists. **(c)** Quadratic (i.e. matter-like) dispersion relation of photons confined to a microcavity as considered here, as described by Eq. (2.9). Due to the microcavity environment, the photon energy for a vanishing transversal wave vector is now finite. Further, for a curved resonator geometry as shown in (a), the system becomes formally equivalent to that of a massive particle trapped in a harmonic oscillator potential.

$$k_z(r) = \frac{q\pi}{D(r)} \,, \tag{2.2}$$

where q is the longitudinal mode number and $D(r)$ is the mirror spacing at a distance $r = |\vec{r}|$ from the optical axis, assuming rotational symmetry. Inserting Eq. (2.2) into Eq. (2.1) leads to

$$E(r, k_r) = \frac{\hbar c}{n} \sqrt{k_r^2 + \left(\frac{q\pi}{D(r)}\right)^2} \,, \tag{2.3}$$

which, assuming $k_r \ll k_z$ as part of a paraxial approximation, can be simplified to

$$E(r, k_r) \simeq \frac{\hbar c}{n} \frac{q\pi}{D(r)} \left(1 + \left(\frac{D(r)}{q\pi}\right)^2 \frac{k_r^2}{2}\right) \,. \tag{2.4}$$

Using the Pythagorean theorem, the mirror spacing can be expressed as

$$D(r) = D_0 - 2 \cdot \left(R - \sqrt{R^2 - r^2}\right) \overset{r \ll R}{\approx} D_0 - \frac{r^2}{R} \,, \tag{2.5}$$

where D_0 is the mirror spacing on the optical axis and R is the radius of curvature of the mirrors. In the last step of Eq. (2.5), an expansion for small distances r from the optical axis has been

performed ($r \ll R$). Inserting Eq. (2.5) into Eq. (2.4) leads to

$$E(r, k_r) \simeq \frac{\hbar c q \pi}{n\,(D_0 - r^2/R)} + \frac{k_r^2}{2}\frac{\hbar c}{n}\frac{D_0 - r^2/R}{q\pi} \,. \tag{2.6}$$

Eventually utilizing that $r^2/R \ll D_0$, the dispersion relation becomes

$$E(r, k_r) \simeq \frac{\pi \hbar c q}{n D_0} + \frac{\hbar c D_0}{2\pi n q} k_r^2 + \frac{\pi \hbar c q}{n D_0^2 R} r^2 \,. \tag{2.7}$$

Introducing an effective photon mass m_{ph} and a trap frequency Ω,

$$m_{\mathrm{ph}} \coloneqq \frac{\pi \hbar n q}{c D_0} \qquad \text{and} \qquad \Omega \coloneqq \frac{c}{n\sqrt{D_0 R/2}} \,, \tag{2.8}$$

this can be rewritten to

$$E(r, k_r) = \frac{m_{\mathrm{ph}} c^2}{n^2} + \frac{\hbar^2 k_r^2}{2 m_{\mathrm{ph}}} + \frac{m_{\mathrm{ph}}}{2}\Omega^2 r^2 \,. \tag{2.9}$$

This result is formally equivalent to the nonrelativistic dispersion relation of a massive particle of mass m_{ph} confined to a two-dimensional harmonic trap exhibiting a trap frequency Ω. The first term corresponds to the rest energy due to the nonvanishing effective photon mass. The second term describes the kinetic energy arising from the photon momentum in the transversal plane of the microcavity (depending on the transversal wave vector k_r). The third and last term represents the potential energy of the photons in the microcavity (depending on the distance r from the optical axis), imprinted by the mirror curvature. From Eq. (2.9) it becomes evident how the microcavity environment has modified the photon dispersion relation. No longer being linear (as is the case for free photons, see Fig. 2.1(b)), the scaling between (transversal) wave vector and energy is now quadratic and photons propagating along the optical axis ($r = 0$) with vanishing transversal excitation ($k_r = 0$) exhibit a ground state (cutoff) energy of $E_{\mathrm{cutoff}} = m_{\mathrm{ph}} c^2/n^2$, as illustrated in Fig. 2.1(c). With typical experimental parameters ($n = 1.43$, $q = 7$, $D_0 = 1.4\,\mu\mathrm{m}$, $R = 1\,\mathrm{m}$), the effective photon mass is in the order of $m_{\mathrm{ph}} = 7.7 \times 10^{-36}\,\mathrm{kg}$, about ten orders of magnitude smaller than the mass of a rubidium atom. The trap frequency $\Omega = 2\pi \times 40\,\mathrm{GHz}$, in contrast, is around nine orders of magnitude larger than in typical experiments on atomic Bose-Einstein condensates. The ground state energy based on this effective photon mass corresponds to a cutoff wavelength around 570 nm, i.e. in the green-to-yellow part of the visible spectrum. The cutoff wavelength is directly determined by the mirror distance via the standing-wave condition. A short mirror spacing in the order of a micrometer is essential, such that the free spectral range $\Delta\lambda_{\mathrm{FSR}} = \lambda_{\mathrm{cutoff}}^2/2nD_0$ is of a similar magnitude as the emission bandwidth $\Delta\lambda_{\mathrm{emis}}$ of the dye molecules used for the thermalization process (which will be illustrated in Sec. 2.2).

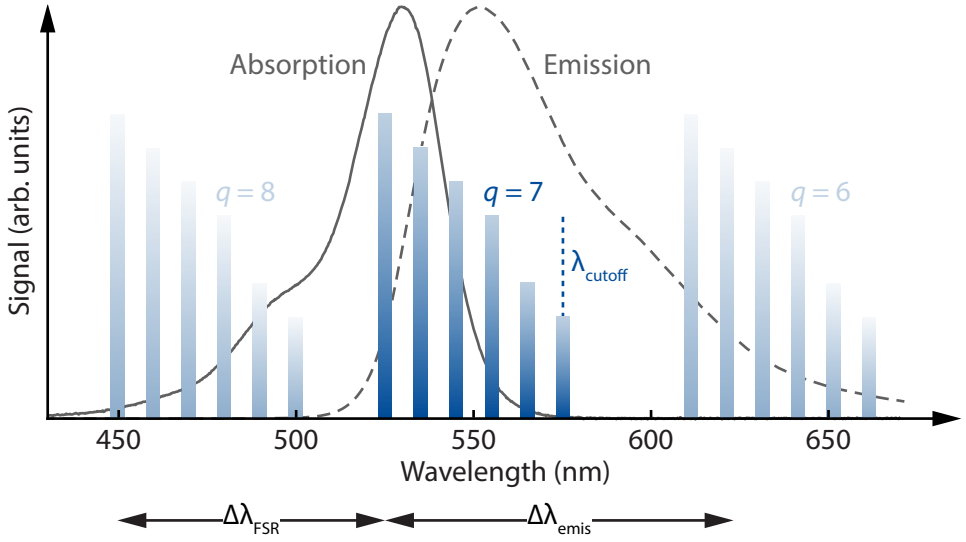

Figure 2.2: Cavity mode spectrum (blue) and absorption and emission spectrum of Rhodamine 6G dye molecules (gray). Vertical bars indicate the transversal cavity modes; blocks of adjacent vertical bars represent the longitudinal modes with mode number q. The free spectral range $\Delta\lambda_{\mathrm{FSR}}$ is of similar magnitude as the emission bandwidth of the dye $\Delta\lambda_{\mathrm{emis}}$, such that the dye molecules predominantly emit into one longitudinal mode (here, $q = 7$). This ensures the two-dimensionality of the system by essentially freezing out the longitudinal degree of freedom.

This way, the dye emission predominantly populates one longitudinal mode, establishing a clear low-energy ground state at the wavelength $\lambda_{\mathrm{cutoff}}$. Thereby, the longitudinal degree of freedom is essentially frozen out, as illustrated by Fig. 2.2, subjecting the photon gas to the condition of two-dimensionality. To adapt the scheme presented here to an application in the vacuum-ultraviolet spectral regime, cutoff wavelengths around 150 nm need to be realized. This can either be achieved via a change of the mirror distance D_0 or, alternatively, via an operation at larger longitudinal mode numbers q. One implementation for such a VUV-suitable microcavity will be presented in App. A.

2.1.2 Statistics of an Ideal Quantum Gas

In the quantum realm, the state of a particle is described by a wavefunction $\psi(\vec{x}, t)$, replacing the classical approach of the macroscopic world. In 1924, Louis de Broglie presented the notion that all particles can show a wave-like character and applied the concept of wave-particle duality, previously known only for photons, also to massive particles [48]. He introduced a characteristic wavelength (which later became known as the de Broglie-wavelength),

$$\lambda_{\mathrm{dB}} = \frac{h}{p}\,, \tag{2.10}$$

where h is Planck's constant and p is the particle's momentum. The thermal de Broglie-

wavelength, usually defined as [49]

$$\lambda_{\mathrm{th}} = \frac{h}{\sqrt{2\pi m k_{\mathrm{B}} T}} , \tag{2.11}$$

with the Boltzmann constant k_{B} and the system temperature T, is a useful quantity for assessing whether a system is governed by classical or quantum physics. For a system to be determined by the laws of classical mechanics, λ_{th} needs to be much smaller than the average particle distance d. As λ_{th} increases (by lowering the temperature), quantum effects become ever more relevant. Upon reaching the condition $\lambda_{\mathrm{th}} \gtrsim d$, the thermal wavepackets overlap, making it necessary to account for the quantum nature of the system. In this case, quantum statistics needs to be considered, differing significantly between integer-spin particles (bosons), where the Bose-Einstein distribution

$$n_{T,\mu}^{\mathrm{BE}}(E) = \frac{g(E)}{\exp\left(\frac{E-\mu}{k_{\mathrm{B}}T}\right) - 1} \tag{2.12}$$

is applicable, and half-integer-spin particles (fermions), where the Fermi-Dirac distribution

$$n_{T,\mu}^{\mathrm{FD}}(E) = \frac{g(E)}{\exp\left(\frac{E-\mu}{k_{\mathrm{B}}T}\right) + 1} \tag{2.13}$$

is applicable. Both $n_{T,\mu}^{\mathrm{BE}}(E)$ and $n_{T,\mu}^{\mathrm{FD}}(E)$ denote the occupation number of a state with energy E and corresponding degeneracy $g(E)$ in a system of temperature T and chemical potential μ. In the nonquantum limit of high temperatures, i.e. $\lambda_{\mathrm{th}} \lesssim d$, both the Bose-Einstein distribution and the Fermi-Dirac distribution can be approximated by the Boltzmann distribution

$$n_{T,\mu}(E) = \frac{g(E)}{\exp\left(\frac{E-\mu}{k_{\mathrm{B}}T}\right)} . \tag{2.14}$$

2.1.3 Photon Statistics in Two Dimensions: The Route toward Condensation

As shown above, photons confined to the microcavity can be treated as equivalent to a two-dimensional gas of massive particles in a harmonic potential. Accordingly, the (single-particle) energy is given by

$$E(n_x, n_y) = \frac{m_{\mathrm{ph}} c^2}{n^2} + \hbar\Omega(n_x + n_y + 1) , \tag{2.15}$$

where n_x and n_y denote the number of transversal excitations in each dimension. This expression

can be rescaled by subtracting the constant ground state energy contribution $m_{\mathrm{ph}}c^2/n^2 + \hbar\Omega$, leading to the transversal excitation energy

$$u(n_x, n_y) \coloneqq E(n_x, n_y) - \frac{m_{\mathrm{ph}}c^2}{n^2} - \hbar\Omega = \hbar\Omega(n_x + n_y) \; . \tag{2.16}$$

The occupation number of a state with the (transversal) excitation energy u is given by the Bose-Einstein distribution

$$n^{\mathrm{BE}}_{T,\mu}(u) = \frac{g(u)}{\exp\left(\frac{u-\mu}{k_{\mathrm{B}}T}\right) - 1} \; . \tag{2.17}$$

As stated by Eq. (2.16), the degeneracy $g(u)$ increases linearly with the excitation energy u,

$$g(u) = 2\left(\frac{u}{\hbar\Omega} + 1\right) \; , \tag{2.18}$$

where the factor 2 accounts for the degree of freedom associated with the polarization. The total particle number N is obtained by summation over all transversal excitations $u = 0,\ \hbar\Omega,\ 2\hbar\Omega,\ ...,$

$$N = \sum_u n^{\mathrm{BE}}_{T,\mu}(u) \; . \tag{2.19}$$

This sum includes all particles in the system, both those with vanishing transversal excitation ($u = 0$) and those with $u > 0$. Given the constraint set by Eq. (2.19), an increase of the particle number toward the critical particle number N_{c} (above which condensation into the energetic ground state occurs) leads to an increase of the chemical potential to zero from below, $\mu \to 0^-$. In this case, however, the contribution to N of particles with $u = 0$ diverges, $n^{\mathrm{BE}}_{T,\mu\to 0^-}(u = 0) \to \infty$. Therefore, in the calculation of the critical particle number, the contribution of particles at $u = 0$ has to be excluded,

$$N_{\mathrm{c}} = \sum_{u\neq 0} n^{\mathrm{BE}}_{T,\mu\to 0^-}(u) = \sum_{u\neq 0} \frac{g(u)}{\exp\left(\frac{u}{k_{\mathrm{B}}T}\right) - 1} \; . \tag{2.20}$$

At this point, quasicontinuous energy levels are assumed, implying that $\hbar\Omega \ll k_{\mathrm{B}}T$. This way, the summation can be replaced by an integration,

$$N_{\mathrm{c}} \simeq \frac{1}{\hbar\Omega}\int_0^\infty \frac{g(u)}{\exp\left(\frac{u}{k_{\mathrm{B}}T}\right) - 1}\mathrm{d}u \simeq 2\left(\frac{k_{\mathrm{B}}T}{\hbar\Omega}\right)^2 \int_0^\infty \frac{z}{\exp(z) - 1}\mathrm{d}z \; . \tag{2.21}$$

In the last step, the substitution $z := u/k_\mathrm{B}T$ was applied. With the value of the integral given by the Riemann zeta function $\zeta(2)$, one obtains a critical photon number N_c and a critical temperature T_c of

$$N_\mathrm{c} \simeq \frac{\pi^2}{3}\left(\frac{k_\mathrm{B}T}{\hbar\Omega}\right)^2 \qquad \text{and} \qquad T_\mathrm{c} \simeq \frac{\hbar\Omega}{\pi k_\mathrm{B}}\sqrt{3N}\,, \tag{2.22}$$

respectively. The trap frequency Ω includes the geometric parameters of the microcavity and inserting Eq. (2.8) into Eq. (2.22) leads to

$$N_\mathrm{c} \simeq \frac{\pi^2}{6}\left(\frac{k_\mathrm{B}Tn}{\hbar c}\right)^2 D_0 R \qquad \text{and} \qquad T_\mathrm{c} \simeq \frac{\hbar c}{\pi k_\mathrm{B} n}\sqrt{\frac{6N}{D_0 R}}\,. \tag{2.23}$$

Investigations of photon Bose-Einstein condensation as treated here are normally conducted at room temperature ($T = 295\,\mathrm{K}$). With a typical set of geometric microcavity parameters ($n = 1.43$, $q = 7$, $D_0 = 1.4\,\mu\mathrm{m}$, $R = 1\,\mathrm{m}$), the critical particle number is in the order of $N_\mathrm{c} \approx 78\,000$. In the experiment, an initial photon population in the microcavity is created by irradiating the dye molecules with a green laser beam (532 nm wavelength). Adjusting the optical power of this pump beam allows to tune the photon number within the microcavity. Once the photon number exceeds the critical particle number N_c, condensation to the mode at the low-energy cutoff sets in. To conclude this discussion, it is worth highlighting that the harmonic potential imposed by the curved mirrors constituting the microcavity is essential for the occurrence of photon Bose-Einstein condensation in two dimensions. A photon not constrained by any kind of potential (corresponding to the case of two uniformly plane mirrors) exhibits a density of states that is independent of the particle energy [47],

$$\mathcal{D} = \frac{mA}{\pi\hbar}\,. \tag{2.24}$$

Here, A is the area the particle can move in. Inserting this into Eq. (2.21) as the degeneracy, the integral no longer converges ($N_\mathrm{c} \to \infty$), illustrating that Bose-Einstein condensation in two dimensions is contingent on the presence of a suitable potential-inducing environment.

2.2 Fluorescence-Induced Thermalization Mechanism

So far, this chapter on the Bose-Einstein condensation of photons has only illustrated the creation of a system with a nontrivial energy ground state and a tailored photon dispersion relation. All the while, the existence of a process which thermally equilibrates the photon gas was taken as a given, without considering the details of said process. This gap will be filled in this section. In the experiments on photon Bose-Einstein condensation considered here, a particle number-

conserving thermalization mechanism is introduced by establishing a thermal contact between the photon gas confined to the microcavity and a liquid dye solution. Starting with an investigation of the involved molecular states on a single-dye-molecule level, the following section will illustrate universal properties of the optical spectra of dye molecules, which are substantial for its ability to mediate thermalization in a photon gas.

2.2.1 The Physics of Dye Molecules and Kennard-Stepanov Relation

Figure 2.3 shows a Jablonski diagram, an idealized visualization of the energetic states of a single dye molecule, as relevant for the explanation of its properties in the context of photon Bose-Einstein condensation. The dye molecule exhibits an electronic ground state S_0 and a number of electronic excited states, which are either singlet states, denoted by S_1 and S_2, or triplet states, denoted by T_1. Each of these electronic states exhibits a number of rovibronic sublevels, numbered by ν, ν' and ν'', respectively. In typical dye molecules, the energy difference between S_0 and S_1 is in the order of 2 eV [50], much larger than the thermal energy at room temperature ($k_\mathrm{B} \cdot 295\,\mathrm{K} \approx 25\,\mathrm{meV}$), rendering the thermal excitation of the higher electronic states extremely unlikely $\left(\exp\left(-2\,\mathrm{eV}/25\,\mathrm{meV}\right) \approx 10^{-35}\right)$. Rather, transitions to the excited electronic states are driven by photons. After such an excitation, the rovibronic level configuration of the dye molecule changes rapidly on a timescale of $10^{-14}\,\mathrm{s}$, due to frequent collisions with surrounding dye and solvent molecules. Considering an ensemble of dye molecules excited to one particular electronic state (usually only S_1 is relevant), the occupation of their rovibronic levels is thermally equilibrated after $10^{-12}\,\mathrm{s}$ and can accordingly be described by a Boltzmann distribution. The radiative lifetime of the electronic excited states is in the order of $10^{-9}\,\mathrm{s}$, such that the ensuingly emitted fluorescence photons come from thermally equilibrated rovibronic manifolds. As a consequence, the Boltzmann distribution is imprinted onto the cavity photons, allowing for the thermalization of the photon gas while conserving the photon number (neglecting losses from a nonunity quantum yield). In the emission process, typically a higher rovibronic level of the electronic ground state S_0 is populated, but rapid collisions lead to an adoption of a Boltzmann distribution in the associated rovibronic manifold as well. To complete the picture, the case of phosphorescence shall be briefly considered, describing the radiative relaxation from an electronic triplet state T_1 (after it has been populated via intersystem crossing) to the electronic ground state S_0. Generally, these transitions are dipole-forbidden due to a changing spin multiplicity, leading to much longer radiative lifetimes of phosphorescence processes (up to a few milliseconds for dye molecules) justifying the tacit omission of phosphorescence in the further treatment of the thermalization process.

The absorption and emission spectra of dye molecules to which these properties apply are known to show a range of universal features:

- Stokes shift [51]: The emission spectrum is shifted to higher wavelengths, i.e. lower energies, with respect to the absorption spectrum.

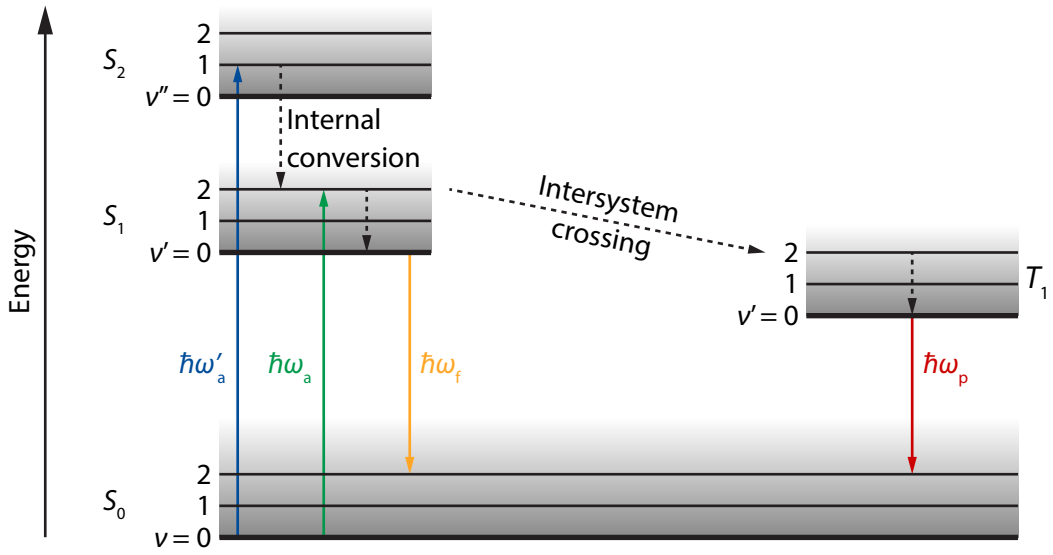

Figure 2.3: Jablonski diagram showing the energy spectrum of a model dye molecule (adapted from [50]). Electronic singlet states are denoted by S_0, S_1 and S_2, an electronic triplet state is denoted by T_1. Each electronic state exhibits a manifold of rovibronic sublevels, labeled ν, ν' and ν''. Optical transitions between electronic states are represented by colored solid arrows. The blue and green arrows indicate absorption events, in which the dye molecule is excited from the S_0 ground state to the S_1 and S_2 states, respectively. The yellow arrow indicates a fluorescence event, in which the dye molecule relaxates from the S_1 state to the S_0 ground state. The red arrow indicates a phosphorescence event, in which the dye molecule relaxates from the T_1 state to the S_0 ground state in a spin-forbidden transition. Collisional (i.e. nonradiative) relaxation processes within and among electronic states are indicated by dashed arrows.

- Kasha's rule [52]: The shape and the spectral position of the emission spectrum are independent of the excitation wavelength.
- Mirror rule: Absorption and emission spectra are mirror images of each other.

The first two observations can be traced back to the internal conversion processes leading to a thermally equilibrated distribution of the rovibronic levels. In the process, rovibronic excitation energy is (on average) dissipated to the surrounding heat bath. As the eventual equilibrium distribution of the rovibronic levels is governed only by the temperature as an external parameter of the Boltzmann distribution, the exact rovibronic level that has initially been occupied right after the excitation is of no relevance. The third observation roots in the fact that the energy spacing between the rovibronic levels within the S_0 and S_1 electronic states is similar, as the nuclear geometry is not significantly altered by electronic transitions. Absorption usually results in a population of higher rovibronic levels of S_1. After rapid thermalization, the subsequent emission originates from the lowest rovibronic level and leaves the molecule in a higher rovibronic level of S_0. Hence, dominant features in the absorption spectrum will also be reflected in the emission spectrum.

An important consequence of the thermalization process is encompassed in the so-called Kennard-

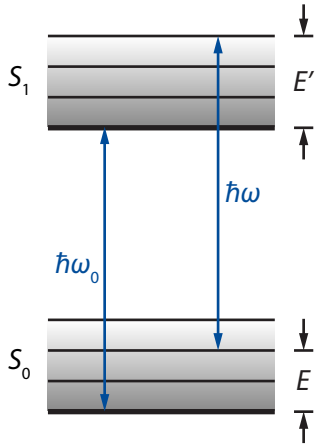

Figure 2.4: Simplified Jablonski diagram for the derivation of the Kennard-Stepanov relation, Eq. (2.25). In this idealized picture, only two electronic (singlet) levels S_0 and S_1 of a dye molecule are considered.

Stepanov relation, a universal relation that links the absorption $\alpha(\omega)$ and fluorescence $\varepsilon(\omega)$ of dye molecules by a Boltzmann-like frequency scaling [53–55],

$$\frac{\varepsilon\left(\omega\right)}{\alpha\left(\omega\right)} \propto \omega^3 \cdot \exp\left(-\frac{\hbar\omega}{k_\mathrm{B}T}\right) . \tag{2.25}$$

In the following, this relation will be derived, following the approach from [56]. For this, a simplified Jablonski diagram is considered, as shown in Fig. 2.4, exhibiting only two electronic singlet states S_0 and S_1. The ratio between fluorescence and absorption strength can be expressed as

$$\frac{\varepsilon\left(\omega\right)}{\alpha\left(\omega\right)} \propto \frac{\int \mathcal{D}'(E')A(E',\omega)p'(E')\mathrm{d}E'}{\int \mathcal{D}(E)B(E,\omega)p(E)\mathrm{d}E} . \tag{2.26}$$

Here, $\mathcal{D}$ and $\mathcal{D}'$ denote the densities of states of the rovibronic levels, p and p' represent the probabilities for a rovibronic level with energy E or E' (relative to the energy of the lowest rovibronic level) to be occupied and $B(E,\omega)$ and $A(E',\omega)$ are the Einstein coefficients for absorption and spontaneous emission (stimulated emission is neglected for now). The occupation of the rovibronic manifold of S_0 right before an absorption event is assumed to be Boltzmann-distributed, $p(E) = \exp\left(-E/k_\mathrm{B}T\right)$. Similarly, for the upper electronic state $p'(E') = \exp\left(-E'/k_\mathrm{B}T\right)$ is assumed, as the emission rate is much smaller than the thermalization rate. Further invoking the Einstein A-B-relation,

$$\mathcal{D}'(E')A(E',\omega)\mathrm{d}E' = \frac{2\hbar\omega^3}{\pi c^2}\mathcal{D}(E)B(E,\omega)\mathrm{d}E , \tag{2.27}$$

Eq. (2.26) becomes

$$\frac{\varepsilon(\omega)}{\alpha(\omega)} \propto \frac{2\hbar\omega^3}{\pi c^2} \frac{\int \mathcal{D}(E) B(E,\omega) \exp\left(-E'/k_\mathrm{B}T\right) \mathrm{d}E}{\int \mathcal{D}(E) B(E,\omega) \exp\left(-E/k_\mathrm{B}T\right) \mathrm{d}E} \,. \tag{2.28}$$

Energy conservation further imposes

$$\hbar\omega + E = \hbar\omega_0 + E' \,, \tag{2.29}$$

where $\hbar\omega_0$ corresponds to the energy gap between the lowest rovibronic levels of S_0 and S_1 (Fig. 2.4). This allows to rewrite Eq. (2.28) as

$$\frac{\varepsilon(\omega)}{\alpha(\omega)} \propto \frac{2\hbar\omega^3}{\pi c^2} \exp\left(-\frac{E'-E}{k_\mathrm{B}T}\right) = \frac{2\hbar\omega^3}{\pi c^2} \exp\left(-\frac{\hbar(\omega-\omega_0)}{k_\mathrm{B}T}\right) \,. \tag{2.30}$$

The prefactor ($\propto \omega^3$) is often neglected due to its much weaker dependency on the frequency than that of the exponential term. Absorbing the constant $\exp(\hbar\omega_0/k_\mathrm{B}T)$ in the proportionality sign, Eq. (2.30) becomes equivalent to Eq. (2.25), the Kennard-Stepanov relation. This equation is essential for assessing whether the level occupation within a rovibronic manifold of a fluorophore is thermally equilibrated. In this thesis, the Kennard-Stepanov relation will become relevant to gauge the suitability of prospective thermalization mediators in the VUV spectral range. Typically, to assess whether the Kennard-Stepanov relation is fulfilled, the quantity $\log(\alpha/\varepsilon)$ is plotted against the photon energy and a function according to Eq. (2.25) is fitted to the data. In Fig. 2.5, this is visualized for different dyes. For Rhodamine 6G, as widely used in experiments on photon Bose-Einstein condensation, Coumarin 314 and Perylene diimide, the data can well be described by the functions, indicating the fulfillment of the Kennard-Stepanov relation over a wide spectral range (the thermal energy $k_\mathrm{B}T$ corresponds to a wavelength range of about 6 nm around a center wavelength of 550 nm). From each fit, a temperature can be extracted, which in the following will be referred to as *spectral temperature* T_s. Generally, a positive deviation of the spectral temperature from ambient temperature (which here is $T = 295\,\mathrm{K}$) is considered a consequence of a nonunity quantum yield [57, 58]. In the case of Chlorophyll B, the agreement between the data and the fit function is slightly inferior, indicating a (partial) violation of the Kennard-Stepanov relation, which has been attributed to the emission from excited triplet states [59]. Beyond dye molecules, the Kennard-Stepanov relation has also been validated in other systems, such as dense rubidium-noble gas mixtures [60], rare earth-doped glasses [55] and semiconductor systems [61].

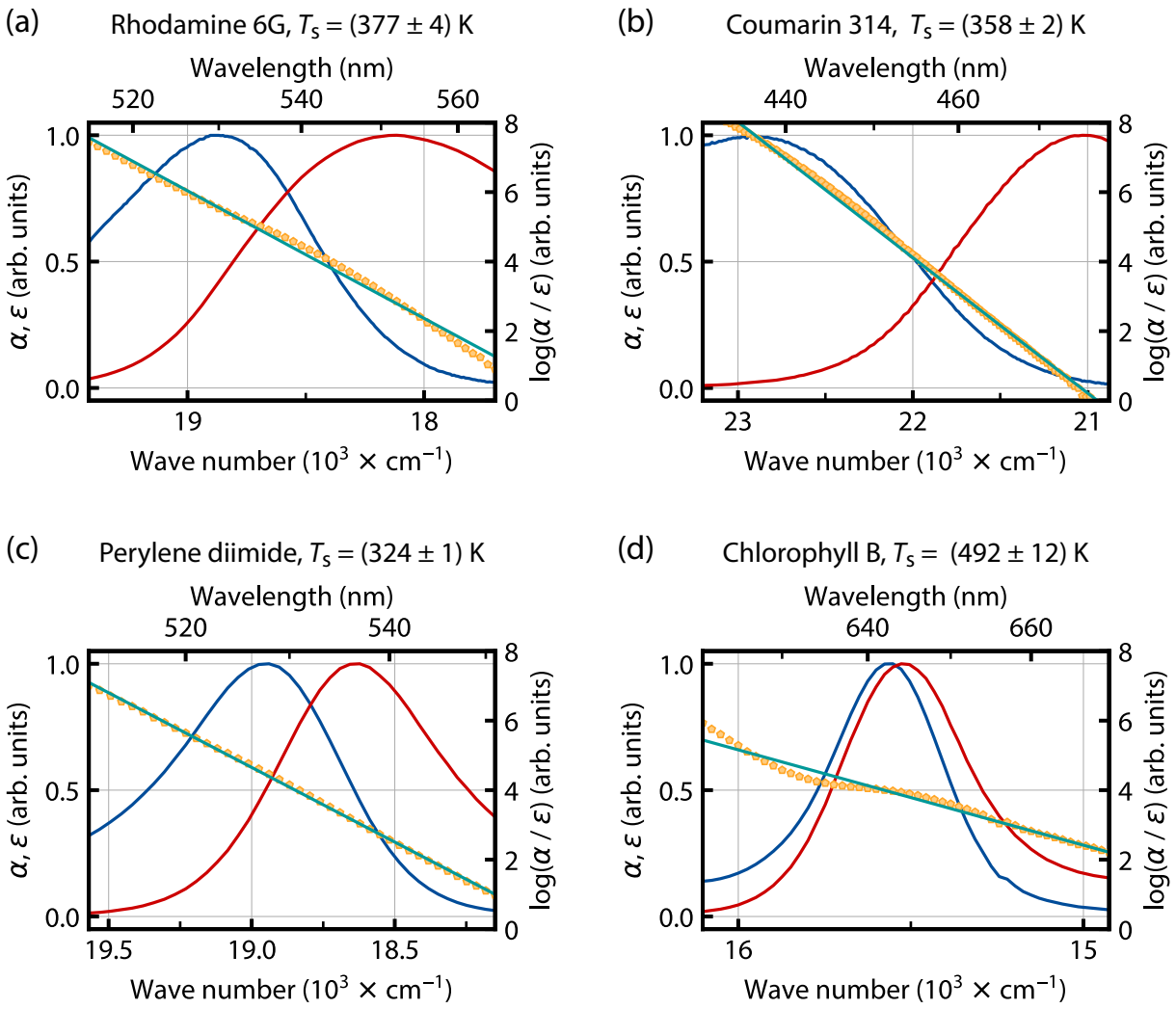

Figure 2.5: Kennard-Stepanov analysis for different dyes, based on absorption (blue) and emission profiles (red) from literature [63]. For each dye, the wave-number-resolved quantity $\log(\alpha/\varepsilon)$ (yellow) is computed and a function according to Eq. (2.25) is fitted to the data (cyan; note the inverted wave-number scale). From this fit, the spectral temperature T_s is obtained. Agreement between the data and the fit function validates the Kennard-Stepanov relation.

2.2.2 Markov Chain and Thermalization of Photons

Thermalization describes a process through which a system reaches a thermal equilibrium with its environment via successive changes of its (internal) configuration. Formally, such a process can be treated as a Markov chain, considering a random walk in the configuration space, where a state C' resulting from a transition only depends on the prior state C and the transition rate $R(C \to C')$ [62]. In this discrete model, the change of the time-dependent probability $p_C(t)$ for the system to be in configuration C is governed by the probability flows into and out of this configuration,

$$p_C(t+1) - p_C(t) = \sum_{C'} p_{C'}(t) R(C' \to C) - \sum_{C'} p_C(t) R(C \to C') \; . \tag{2.31}$$

Demanding that the system configuration asymptotically approaches a thermalized equilibrium distribution, $p_C(t \to \infty) \stackrel{!}{=} \exp\left(-E_C/k_\mathrm{B}T\right)$, this becomes

$$0 = \sum_{C'} \left(\exp\left(\frac{-E_{C'}}{k_\mathrm{B}T}\right) R(C' \to C) - \exp\left(\frac{-E_C}{k_\mathrm{B}T}\right) R(C \to C') \right) \; . \tag{2.32}$$

This equation has multiple solutions. A particular one is the *detailed-balance condition*, where the probability inflows and outflows cancel mutually (no net flow between any two configurations),

$$0 = \exp\left(\frac{-E_{C'}}{k_\mathrm{B}T}\right) R(C' \to C) - \exp\left(\frac{-E_C}{k_\mathrm{B}T}\right) R(C \to C') \qquad \forall\, C,\, C' \; . \tag{2.33}$$

Alternatively, introducing the energy difference $\Delta E = E_{C'} - E_C$, this can be written as

$$\frac{R(C \to C')}{R(C' \to C)} = \exp\left(-\frac{\Delta E}{k_\mathrm{B}T}\right) \qquad \forall\, C, C' \; . \tag{2.34}$$

This equation states that a system, in which the transition rates $R(C \to C')$ and $R(C' \to C)$ between different configurations fulfill Eq. (2.34), will eventually adopt a thermal equilibrium distribution.

This finding will now be applied to the thermalization of a photon gas, identifying different system configurations C and C' as different mode configurations of the light field and identifying the transition rates $R(C \to C')$ and $R(C' \to C)$ as the absorption and fluorescence rates $\alpha(\omega)$ and $\varepsilon(\omega)$. For this, the case of photons confined to a (macroscopic) dye solution-filled container is considered, as depicted in Fig. 2.6. The walls of the container are assumed to be perfectly reflecting and only two small holes in the walls allow photons to enter or leave the container. It is further assumed that the dye molecules exhibit unity quantum yield, such that transitions between different configurations occur only radiatively. Initial excitation of the dye molecules with light guided through the hole into the container and subsequent fluorescence leads to a specific configuration of the radiation field,

$$C = |n_0^C, n_1^C, ..., n_i^C, ..., n_j^C, ...\rangle \; . \tag{2.35}$$

Here, n_i^C denotes the photon number in mode i for the configuration C. By a cycle of absorption from mode i and reemission into mode j $(i \neq j)$, the configuration C' is reached,

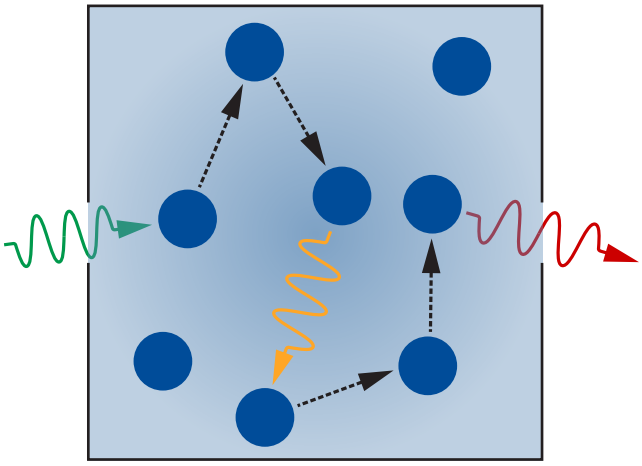

Figure 2.6: Illustration of the thermalization process of photons in a liquid dye solution (blue, individual molecules represented by circles). Short-wavelength photons (green) are absorbed by dye molecules, generating initial excitation to a high rovibronic level. In collisions with surrounding molecules, the occupation of the rovibronic levels is driven into thermal equilibrium, dissipating energy and leading to the wavelength of a subsequently emitted photon to be red-shifted (yellow). The process repeats several times, until eventually a photon is emitted at a wavelength the dye solution is transparent for (red), allowing it to escape from the macroscopic container.

$$\begin{aligned} C' &= |n_0^{C'}, n_1^{C'}, ..., n_i^{C'}, ..., n_j^{C'}, ...\rangle \\ &= |n_0^{C}, n_1^{C}, ..., n_i^{C} - 1, ..., n_j^{C} + 1, ...\rangle \ . \end{aligned} \tag{2.36}$$

The transition rate $R(C \to C')$ from configuration C to C' is governed by the absorption from mode i and the emission into mode j. Considering both spontaneous and stimulated processes, it can be written as

$$R(C \to C') \propto \underbrace{n_i^C \alpha(\omega_i)}_{\text{Absorption}} \cdot \underbrace{(n_j^C + 1)\varepsilon(\omega_j)/\hbar\omega_j \mathcal{D}(\omega_j)}_{\text{Emission}} \ . \tag{2.37}$$

Here, $\alpha(\omega_i)$ is the absorption coefficient and $\varepsilon(\omega_j)$ is the spectral energy density per fluorescence event. Normalizing the latter to the factor $\hbar\omega_j \mathcal{D}(\omega_j)$ removes the photon energy $\hbar\omega_j$ and the density of states $\mathcal{D}(\omega_j) = \omega_j^2/\pi^2 c^3$, such that the spectral emission probability into mode j remains. Analogously, the rate of the inverted transition (involving absorption from mode j and emission into mode i) is found to be

$$\begin{aligned} R(C' \to C) &\propto n_j^{C'} \alpha(\omega_j) \cdot (n_i^{C'} + 1)\varepsilon(\omega_i)/\hbar\omega_i \mathcal{D}(\omega_i) \\ &\propto (n_j^C + 1)\alpha(\omega_j) \cdot n_i^C \varepsilon(\omega_i)/\hbar\omega_i \mathcal{D}(\omega_i) \ . \end{aligned} \tag{2.38}$$

The ratio between the transition rates from Eqs. (2.37) and (2.38),

$$\frac{R(C \to C')}{R(C' \to C)} = \frac{\alpha(\omega_i)\varepsilon(\omega_j)\omega_i^3}{\alpha(\omega_j)\varepsilon(\omega_i)\omega_j^3} \,, \tag{2.39}$$

is independent of the occupation number of the respective modes. Invoking the Kennard-Stepanov relation from Eq. (2.30), this becomes

$$\frac{R(C \to C')}{R(C' \to C)} = \exp\left(\frac{\hbar(\omega_i - \omega_0)}{k_\mathrm{B}T}\right) \cdot \exp\left(-\frac{\hbar(\omega_j - \omega_0)}{k_\mathrm{B}T}\right) = \exp\left(-\frac{\hbar(\omega_j - \omega_i)}{k_\mathrm{B}T}\right) \,, \tag{2.40}$$

fulfilling the detailed balance condition from Eq. (2.34). Put differently, a light field which is in thermal contact with a medium whose absorption and emission spectra fulfill the Kennard-Stepanov relation, eventually adopts a thermalized equilibrium distribution.

Coming back to the photon container introduced at the beginning of this section, it now becomes evident that after an infinite number of absorption and subsequent reemission cycles the photon gas would theoretically adopt a thermalized energy distribution. However, with every cycle the observed emission spectrum is gradually red-shifted, accompanied by a reduced absorption of the radiation by the dye solution. Eventually, this leads to a breakdown of the thermal contact between photon gas and dye molecules, resulting in an incomplete thermalization. This again illustrates the relevance of the microcavity environment in experiments on Bose-Einstein condensation of photons, as its low-energy cutoff curtails the allowed wavelength range for photons confined to the cavity, such that a sufficient thermal contact between the photon gas and the dye molecules is maintained throughout.

2.3 Requirements of a Prospective Thermalization Mediator

So far, this chapter has illustrated the foundations of the Bose-Einstein condensation of photons. Most importantly, the provision of a nontrivial energy ground state (via a wavelength-size microcavity) and the introduction of a particle number-conserving thermalization process (via thermal contact with a liquid dye solution) have been illuminated. In experiments on Bose-Einstein condensation of visible-spectral-range photons, the presented scheme is generally implemented by filling the microcavity with a Rhodamine 6G dye solution, whose molecules are initially excited using laser radiation at a wavelength of 532 nm. The photons inside the microcavity need to undergo multiple cycles of absorption and subsequent reemission before they leave the cavity, such that a thermalization of the photon gas can occur (typical storage times are in the order of 250 ps [64]). In previous work, it was shown that about three such cycles are necessary [47]. The dielectric mirrors used for photon BEC experiments in the visible spectral range exhibit reflectivities in excess of 99.998 % for center wavelengths around 540 nm, leading to a finesse of

$\mathcal{F} = \pi\sqrt{R}/(1-R) \approx 100\,000$. This allows for the employment of relatively dilute dye solutions (a typical concentration is $3\,\mathrm{mmol\,L^{-1}}$, with an absorption coefficient of about $0.5\,\mathrm{cm^{-1}}$ at the typical cutoff wavelength of 580 nm [63]). For these, the quantum yield is in the order of 95 % [65]; high enough to consider this thermalization process photon number-conserving.

In the vacuum-ultraviolet spectral range, mirror reflectivities are generally much lower; commercially available mirrors based on dielectric coatings achieve maximum reflectivities of about 97 % [66]. A microcavity comprising two such mirrors correspondingly exhibits a finesse in the order of $\mathcal{F} = 100$, three orders of magnitude smaller than those in the visible spectral range. The correspondingly smaller storage time needs to be compensated by a larger absorption probability per round trip. The number of absorption and reemission cycles N for a given finesse can be calculated as [46]

$$N = \mathcal{F}\left(1 - \exp\left(-\alpha L\right)\right) \ , \tag{2.41}$$

where α is the absorption coefficient of the thermalization medium and L is the mirror distance. Solving Eq. (2.41) for α results in

$$\alpha = \ln\left(\frac{\mathcal{F}}{\mathcal{F} - N}\right) L^{-1} \ . \tag{2.42}$$

An a priori demand that the photons in the VUV-range microcavity are subject to the same number of absorption and reemission cycles ($N = 3$) and the assumption of a similar mirror distance ($L \approx 1\,\mu\mathrm{m}$) yields an absorption coefficient of $\alpha \approx 300\,\mathrm{cm^{-1}}$. In other words, this is the necessary absorption coefficient a prospective thermalization medium needs to exhibit to convey the thermalization mechanism for visible photons into the vacuum-ultraviolet spectral regime.

3 The Physics of Diatomic Molecules

The last chapter has illustrated how a thermalization mechanism is implemented in experiments on the Bose-Einstein condensation of photons, based on the thermal contact between the photon gas and a liquid dye solution. For the realization of a similar system with photons in the vacuum-ultraviolet spectral range (100 nm − 200 nm), a different thermalization medium has to be identified, as no dye molecules with suitable transitions in this wavelength range are known. Moreover, this wavelength range corresponds to photon energies above 6 eV, far exceeding the binding energies of typical dye molecules, leading to their dissociation under irradiation.

Noble gases, in contrast, are not subject to these limitations. Xenon, whose consideration as thermalization medium was suggested previously [46], possesses an atomic resonance at 146.9 nm, well within the VUV spectral range (other, lighter noble gases have transitions at even shorter wavelengths). At first glance, the consideration of an atomic species as a thermalization medium might appear counterintuitive, as such a system does not exhibit an energetic substructure beyond its electronic levels. This would be in contrast to the finding of Chap. 2, that a medium employed for the thermalization of photons needs to have a (rovibronic) level substructure, as only in this case the detailed-balance condition can be fulfilled. As will be shown throughout this chapter, however, in dense noble gas environments the constituents can no longer be treated individually; this leads to the emergence of properties resembling those of molecules. This chapter will illuminate the binding mechanisms leading to the formation of such quasimolecules and their consequences for the potential energy curves, using a model dimer system. These observations will then be applied to the specific case of xenon and xenon-noble gas mixtures. Lastly, an overview will be given about previous spectroscopic measurements of xenon and xenon-based mixtures with relevance to the investigations of this work.

3.1 A Model Noble Gas Dimer System

Due to their fully occupied outer electron shell, noble gas atoms are known for their reluctance to form bonds, as compared to, for example, the highly reactive alkalis with a single electron in the outermost shell. However, given appropriate conditions, there nevertheless exist certain mechanisms that can facilitate bond formation also for noble gas atoms [67]. As will be elaborated on, these form the foundation for the prospect of xenon to be used as a thermalization medium in experiments on the Bose-Einstein condensation of VUV photons. The following discussion will be limited to the case of two interacting noble gas atoms, as the likelihood of an n-body encounter decreases with the number n of involved particles.

3.1.1 Van der Waals-Bonding

On temporal average, the electron cloud of a noble gas atom A in the electronic ground state exhibits a spherically symmetric distribution around its nucleus, leading to a vanishing *permanent* dipole moment and hence a vanishing permanent dipole-dipole interaction between two noble gas atoms. On closer examination, though, the electron distribution continuously deviates from the average spherically symmetric distribution. At any given time, there is a *transient* dipole moment, induced by a nonsymmetric charge distribution of the electrons around the nucleus and accompanied by an electric field E_A. If now a second atom B is exposed to the field E_A, a dipole moment p_B is induced, that is in turn accompanied by an electric field E_B which influences atom A, leading to a mutual interaction. A transient quasimolecule formed by two atoms approaching and interacting in this way is referred to as *dimer*. The corresponding potential $V(r) \propto -1/r^6$ is attractive, but only relevant on very short internuclear distances. Typically, it is relatively weak compared to other bonding mechanisms. For example, for H_2 and O_2, the binding energy rooted in the van der Waals-bonding amounts to only 0.6 meV and 4.6 meV, respectively [68]. As a comparison, the total atomization energies of dihydrogen and dioxygen are 4.5 eV and 5.1 eV [69]. In dimerized compounds of noble gases, the binding energy increases from the lightest species, He_2 (0.9 meV), over Ne_2 (3.7 meV), Ar_2 (12.4 meV) and Kr_2 (17.3 meV) to Xe_2 (24.4 meV) [70, 71]. As this is below the thermal energy at room temperature (25 meV), no reports are available about the formation of stable xenon-xenon dimers at room temperature.

3.1.2 Covalent Bonding

The situation changes, if one of the noble gas atoms is in an electronic excited state. Now, the electron distribution around the nucleus is no longer radially symmetric, as one electron has been elevated to a higher shell. This increases the electron density between the two atoms, leading to a directional electrostatic attraction between the shared electrons and the nuclei. In other words, the single electron mediates an attraction between the two atoms (covalent bond), leading to the formation of an excited quasimolecule called *excimer* (excited dimer). The much stronger attraction between its constituents leads to a significantly higher binding energy, making the thermal dissociation of such a compound highly unlikely (in the case of a xenon-xenon excimer, the binding energy is around 507 meV [72]). This implies that the (radiative) lifetime of an excimer is dictated by the lifetime of the associated electronic state of its excited constituent.

3.1.3 Potential Energy Diagram

The bonding mechanisms introduced so far lead to some universal properties in the scattering behavior of noble gas atoms (although several of the principles discussed here can also be applied to non-noble gas systems with slight modifications). These are depicted in Fig. 3.1, showing the potential energy of a dimer system formed by two noble gas atoms as a function of their

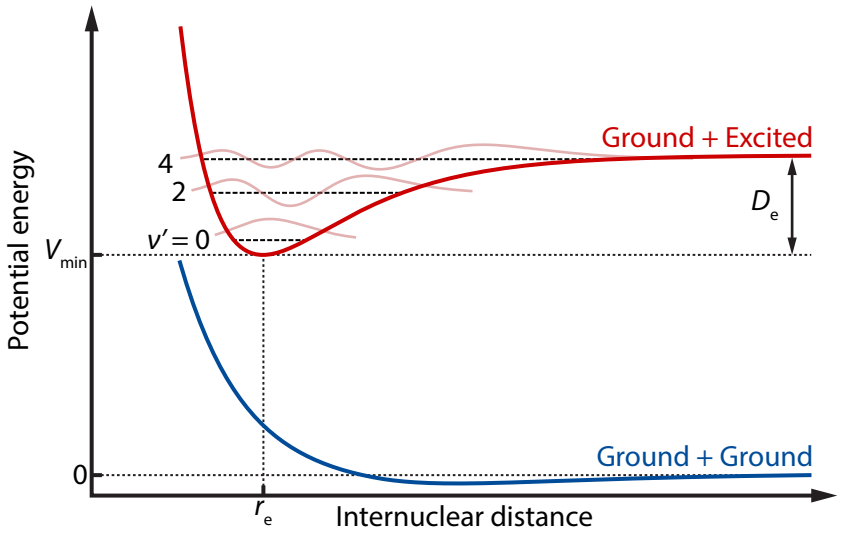

Figure 3.1: Potential energy diagram of a model dimer system, here considered as consisting of two scattering noble gas atoms. The dimer ground state (blue) is formed by two atoms in their respective electronic ground states. The excited state (excimer; red) is formed by one atom in the electronic ground and one atom in an electronic excited state. While the ground state exhibits only a weakly pronounced potential well without any bound levels, the excited state exhibits a strongly pronounced potential well. This allows the emergence of bound levels within this part of the potential energy curve, indicated as black dashed lines and labeled ν'. Select wavefunctions of levels within this quasimolecular collisional manifold are also shown. The quantities V_{min}, r_{e} and D_{e} are parameters of the Morse potential, Eq. (3.1).

internuclear distance. For the case of both atoms being in the electronic ground state, at large internuclear distances the potential energy curve is flat and the two atoms can be considered isolated from each other. As the atoms approach each other, at some point they begin to interact via the van der Waals-force, which leads to the formation of a shallow potential well. As the kinetic energy of the constituent particles is higher than the corresponding binding energy, no stable dimers result from this. For even smaller internuclear distances, the potential energy curve exhibits a steep potential barrier. This is caused by the Pauli exclusion principle, preventing the completely filled electron clouds from overlapping. As a result, both atoms are repelled from each other and separate until they can again be considered isolated upon reaching the region where the potential energy curve is flat. It is worth noticing that in this scenario no equilibrium distance can be stated, as, for a thermal gas, the atoms continually approach and separate again. The short-distance reversal point of this motion corresponds to the internuclear distance where the potential energy equals the constituents' kinetic energy.

The situation is different for the case of an excimer, i.e. a dimer with one of the constituent atoms in an electronic excited state (excimers consisting of *two* excited atoms are not considered here, due to typically rather low densities of excited atoms – for typical experimental parameters, the photon density is at least three orders of magnitude smaller than the atom density). Again, for large internuclear distances, the atoms can be considered isolated. As the atoms approach each other, however, the compound is subject to a much stronger binding due to the newly formed

covalent bond, allowing for the formation of a quasistable excimer. Equally as in the case with two atoms in the ground state, at even smaller internuclear distances a steep potential barrier arises, caused by the Coulomb repulsion of the approaching atoms. The pronounced potential well, whose minimum position is usually referred to as equilibrium position, in this case leads to the occurrence of bound levels with discretely spaced energies. The entirety of these levels, in the following also called *quasimolecular (collisional) manifold*, is the equivalent of the dimer system to the rovibronic manifolds of the dye molecules treated in Chap. 2.2.1.

The potential energy curves of noble gases are usually described quantitatively by Morse potentials, introduced in 1929 [73, 74], of the form

$$V(r) = D_\mathrm{e} \cdot \left(1 - \exp\left(-\alpha\left(r - r_\mathrm{e}\right)\right)\right)^2 + V_\mathrm{min} \; . \tag{3.1}$$

Here, D_e denotes the dissociation energy (i.e. the depth of the potential well) at the equilibrium position r_e. The parameter α determines the width of the potential well. The energy offset V_min corresponds to the energy level of the potential minimum, such that $V(r \to \infty) = V_\mathrm{min} + D_\mathrm{e}$ is the asymptotic energy for large internuclear distances (equivalent to the energy level of an undisturbed atom). Typically, it is not possible to use one set of parameters $(D_\mathrm{e}, \alpha, r_\mathrm{e}, V_\mathrm{min})$ to describe the real potential energy curve of a certain excimer state, such that for different ranges of internuclear distances different parameter sets are to be used. With the potential $V(r)$, the Schrödinger equation can be solved analytically, leading to the eigenenergies of the level ν within this quasimolecular collisional manifold [67],

$$E_\nu = \hbar\omega_0 \cdot \left(\nu + \frac{1}{2}\right) - \frac{\hbar^2\omega_0^2}{4D_\mathrm{e}} \cdot \left(\nu + \frac{1}{2}\right)^2 \; , \tag{3.2}$$

relative to the nadir of the potential well. The oscillator frequency $\omega_0 = \alpha\sqrt{2D_\mathrm{e}/\mu}$ depends on the reduced mass $\mu = (m_1 \cdot m_2) \,/\, (m_1 + m_2)$ of the constituents, with m_1 and m_2 their individual masses. Although Eq. (3.2) bears resemblance to the eigenenergies of a harmonic oscillator, it becomes evident that the energy difference between two consecutive levels decreases for higher quantum numbers ν. For eigenenergies below the dissociation energy D_e, this energy difference remains finite, such that only a finite number of levels exists within the bound part of the potential energy curve (although the energy spacing between two adjacent levels decreases with increasing ν). Outside the bound regions of the potential energy diagram, i.e. for energies in excess of the dissociation energy, a continuum of levels exists, with infinitesimally small energy spacings between any two levels. Numerically, these can be accounted for by approximating the unbound region of the potential energy curve by a box potential. Its boundaries are defined by the steep potential barrier at short internuclear distances and by a hypothetical, infinitely high potential barrier at large internuclear distances.

3.1.4 Franck-Condon Principle and (Second) Excimer Continuum

Potential energy curves are essential for an understanding of the shape of optical spectra of quasimolecular dimer systems. Here, it is conceptually outlined how such spectra can be inferred from potential energy curves, using the example of an emission spectrum. The Franck-Condon principle states that transitions occur instantaneously, i.e. without change of the internuclear coordinates during a transition, corresponding to vertical lines in the potential energy diagram [50]. Initially, a calculation of the spatially-resolved wavefunctions $\psi_\nu(r)$ and $\psi_{\nu'}(r)$ of the levels within the quasimolecular collisional manifolds of the ground and excited dimer states is necessary. In the excited state, these correspond to the thermally stable bound levels ν' within the potential well. The ground state, as considered here, due to its shallow potential well only exhibits thermally unstable levels. These, in addition to a continuum of levels with energies above the dissociation energy, can also be treated as levels ν of a quasimolecular collisional manifold with associated wavefunctions $\psi_\nu(r)$ [75]. The obtained wavefunctions are determining the probability ρ to find the two scattering particles at a distance $r = r_0$,

$$\begin{aligned} \rho\left(r_0, \nu\right) &= \left|\psi_\nu\left(r_0\right)\right|^2 = \psi_\nu\left(r_0\right)\psi_\nu^*\left(r_0\right) \\ \rho\left(r_0, \nu'\right) &= \left|\psi_{\nu'}\left(r_0\right)\right|^2 = \psi_{\nu'}\left(r_0\right)\psi_{\nu'}^*\left(r_0\right) \ . \end{aligned} \tag{3.3}$$

The probability for a fluorescent transition between a level ν_0' of the excited state manifold and a level ν_0 of the ground state manifold is given by the squared absolute value of the wavefunction overlap,

$$P\left(r, \nu_0, \nu_0'\right) = \left|\psi_{\nu_0}\left(r\right)\psi_{\nu_0'}\left(r\right)\right|^2 \ . \tag{3.4}$$

The total contribution of this particular $\nu_0' \rightarrow \nu_0$-transition is obtained by integrating over the internuclear distance r [67],

$$P(\nu_0', \nu_0) = \int P\left(r, \nu_0, \nu_0'\right) \mathrm{d}r \ . \tag{3.5}$$

This transition yields a contribution to the emission spectrum at the energy $E_0 = \Delta E(\nu_0, \nu_0')$. This procedure is repeated for all other transitions with different (ν', ν)-combinations, yielding contributions at other transition energies. Eventually, a weighting function has to be applied to the individual contributions to the spectrum, accounting for the nonuniform occupation of the various levels ν' under consideration. Assuming a thermally equilibrated occupation of the levels in the excited state's quasimolecular manifold, as caused by frequent collisions between dimers and surrounding atoms, a Boltzmann-distribution $p(E_{\nu'}) = \exp\left(-E_{\nu'}/k_\mathrm{B}T\right)$ is adequate.

Emission stemming from the thermalized quasimolecular manifold of the excited state is histor-

ically referred to as *second excimer continuum*. Experimentally, however, in some situations the emission spectrum exhibits features that cannot be explained by the above-described picture of complete thermalization within the excited state's quasimolecular manifold. At very low gas pressures, it is unlikely that an excited atom encounters another atom to form a dimer, such that it is likely to relaxate to the ground state with emission on the atomic line (corresponding to the asymptotic case of large internuclear distances in the potential energy diagram). At slightly higher pressures, it is possible that an excited atom encounters another and that they form a dimer, without, though, actually reaching the strongly bound region of the potential energy curve. Emission from these higher-energetic levels is referred to as *first excimer continuum*. In the emission spectra, it results in a broad spectral contribution, stretching between the atomic line and the second excimer continuum[1].

3.2 Xenon as a Prospective Thermalization Mediator

Xenon is the heaviest stable noble gas, with an atomic number of 54 and an isotope-weighted atomic mass of 131.29 u [77]. It was first identified in 1898 by William Ramsay and Morris William Travers [78], who named it after the Greek ξένος ("stranger"). Although its abundance in the universe is on roughly the same level as that of elements such as rubidium and nickel [79], it is the rarest stable element on earth. This discrepancy, interestingly poorly understood [80], leads to xenon being the most expensive noble gas. Despite its rarity, the colorless and odorless gas is used in a wide range of applications, as diverse as vehicle headlights, laser flash lamps, scintillation material in particle detectors [81], space propellant [82] and anesthetics [83].

Figure 3.2 shows the phase diagram of xenon. Under normal temperature and pressure conditions (NTP, $T_{\mathrm{NTP}} = 293.15\,\mathrm{K}$, $p_{\mathrm{NTP}} = 1\,\mathrm{atm}$ [84]), xenon is in the gaseous phase. The critical point, constituting the intersection of the gaseous and liquid phases and the supercritical regime is located at $T_{\mathrm{crit}} = 289.73\,\mathrm{K}$ and $p_{\mathrm{crit}} = 58.42\,\mathrm{bar}$ [77]. The triple point, meanwhile, constituting the intersection of the gaseous, liquid and solid phases, is located at $T_{\mathrm{trip}} = 161.41\,\mathrm{K}$ and $p_{\mathrm{trip}} = 0.82\,\mathrm{bar}$. First-order phase transitions (involving a discontinuity of an order parameter such as the density [25]) occur between the gaseous, liquid and solid phases. Transitions from the gaseous and liquid phases into the supercritical regime, in contrast, are characterized by a continuous change of the order parameter. Reaching the solid phase requires either temperatures below 161 K or pressures above 1000 bar. Both being experimentally very challenging, most previous investigations of xenon have focused on the gaseous, liquid and supercritical regimes, as will be illustrated in more detail in Sec. 3.3.

[1] Continuing the sequential labeling of the continua, the *third excimer continuum* describes emission bands at even higher wavelengths, which are generally attributed to the emission by singly ionized noble gas atoms [76].

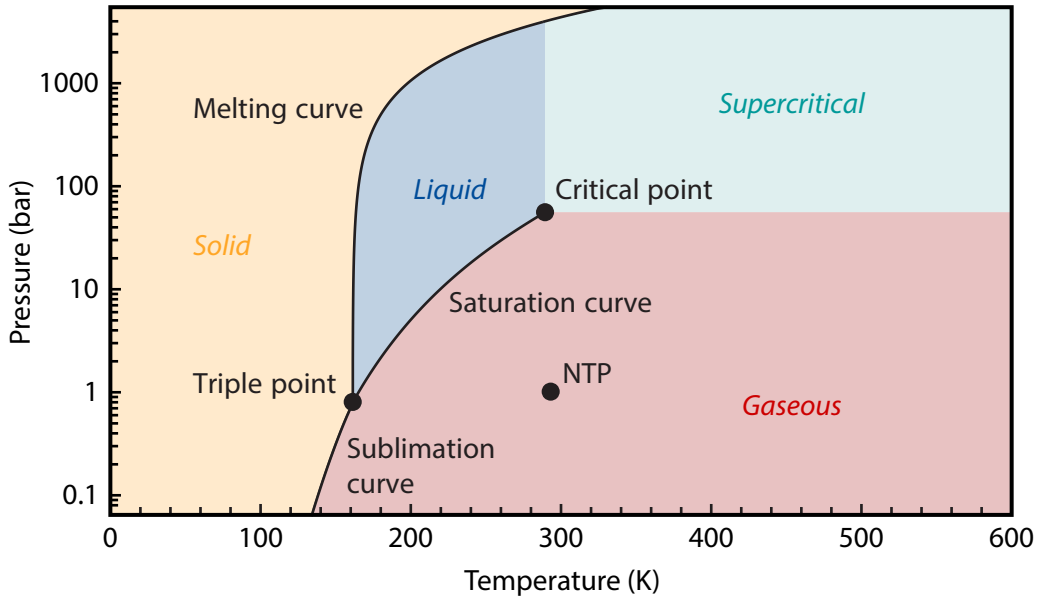

Figure 3.2: Phase diagram of xenon, data from [77, 85]. NTP (normal temperature and pressure) conditions correspond to a temperature of 293.15 K and a pressure of 1 atm. Solid black lines indicate first-order phase transitions between adjacent regimes.

3.2.1 Potential Energy Diagram

With the concepts of dimer formation introduced in Sec. 3.1, it is now possible to contemplate the suitability of xenon as a thermalization mediator for VUV photons. The discussion will include both the homonuclear system (i.e. pure-xenon environments) and the heteronuclear system (i.e. xenon-noble gas mixtures).

Homonuclear System

The discussion begins at the *atomic* energy levels of xenon, as visualized in Fig. 3.3(a). From the $5p^6$ ground state, the lowest-energy dipole-allowed one-photon transition is the $5p^6 \rightarrow 5p^5 6s[3/2]_1$ transition (atomic states in this thesis are denoted using Racah notation, see App. B). It has a transition energy of 8.44 eV, corresponding to a transition wavelength of 146.9 nm, well within the VUV spectral regime [86]. The lowest-energy allowed two-photon transition is the $5p^6 \rightarrow 5p^5 6p[5/2]_2$ transition with a transition energy of 9.68 eV, corresponding to the energy of two photons at a wavelength of 256.0 nm. Energetically close to this $5p^5 6p[5/2]_2$ state are two more even-angular-momentum states within the $5p^5 6p$ configuration. At even higher energies, there are two even-angular-momentum states within the $5p^5 6p'$ configuration (the $5p^5 6p$ and $5p^5 6p'$ configurations differ in the angular momenta of their respective parent ions).

The atomic states listed so far form the basis for the quasimolecular states of the homonuclear xenon-xenon dimer system, as illustrated by the potential energy diagram in Fig. 3.3(b), showing

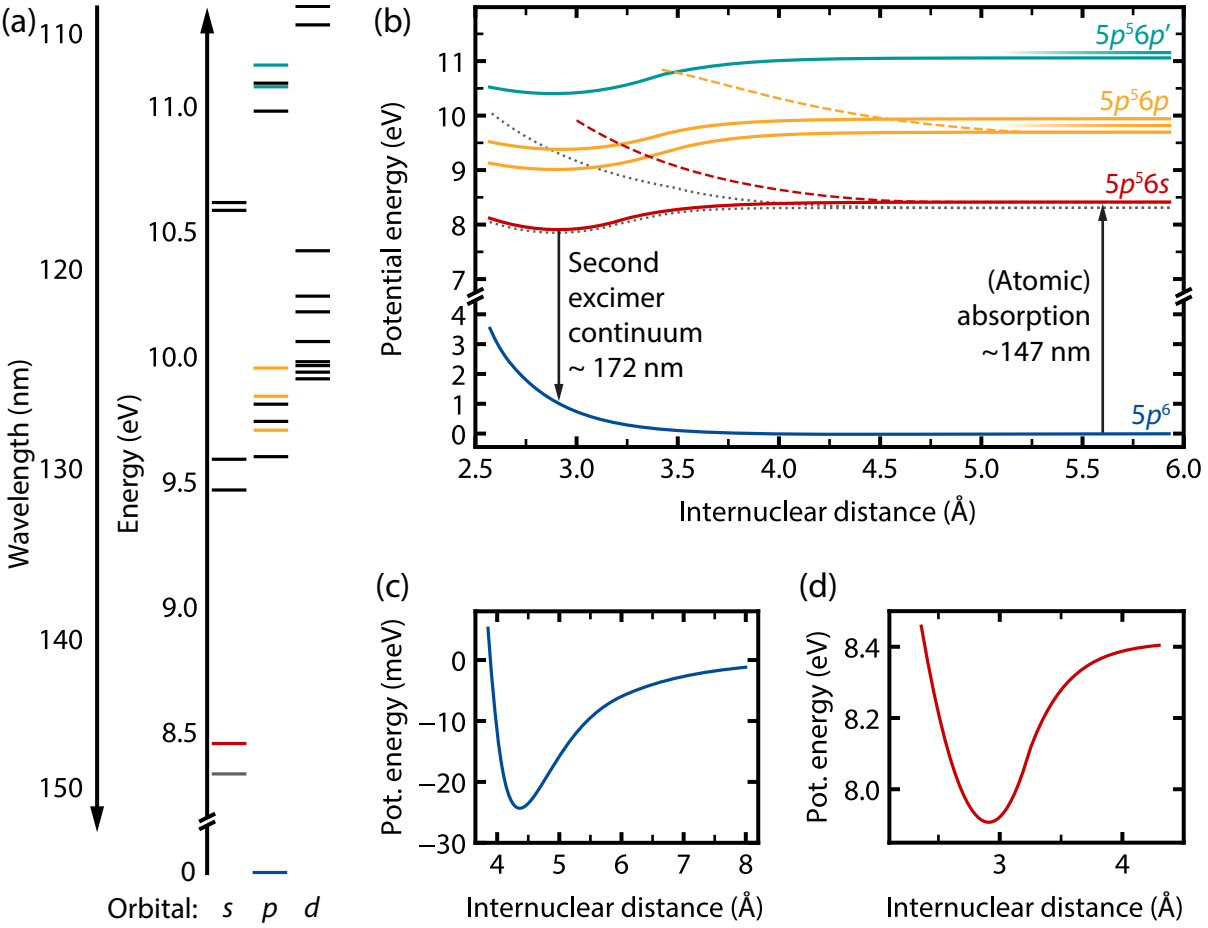

Figure 3.3: Energy levels of xenon and associated quasimolecules [71, 72, 86] – **(a)** Energy diagram of the energy levels of *atomic* xenon, categorized by the shell (s, p, d) of the valence electron. All electronic states up to the ionization limit are shown. As a reference, the wavelength axis indicates the transition wavelength between a given state and the $5p^6$ electronic ground state. **(b)** Potential energy diagram of xenon-xenon dimers, showing the dimerized energy levels relevant for this work. The colors correspond to the colors used in the atomic energy diagram (a). For the excited states, solid lines represent attractive manifestations of the potential energy curves, whereas dashed lines represent repulsive manifestations. The gray dotted line indicates the potential energy curves associated with the metastable $5p^5 6s[3/2]_2$ state. **(c)** Magnification of the shallow potential well of the dimer state associated with the atomic $5p^6$ ground state. **(d)** Magnification of the pronounced potential well of the first excimer state, associated with the atomic $5p^5 6s$ state.

only the configurations relevant for this thesis. The dimerized ground state is constituted by two atoms in the electronic ground state $5p^6$. The associated potential energy curve is repulsive, preventing the formation of stable dimers of atoms in this state (a zoom-in on a very shallow potential well is shown in Fig. 3.3(c), which, however, is not pronounced enough for the formation of stable dimers). The potential energy curve of the first excimer state is constituted by one atom in the $5p^6$ and $5p^5 6s[3/2]_1$ states each. This potential energy curve exhibits a pronounced potential well, magnified in Fig. 3.3(d), with a depth of 507 meV (corresponding to around 20 $k_\mathrm{B}T$ at room temperature) and an equilibrium distance of 2.9 Å. Energetically just below the $5p^5 6s[3/2]_1$ state lies the $5p^5 6s[3/2]_2$ state, which is commonly referred to as a *metastable* state.

It exhibits the same electron configuration but differs in the total angular momentum ($J = 2$), rendering a direct optical excitation of this state from the ground state dipole-forbidden. It can, however, be populated via potential curve crossings from higher-lying excimer states (although such processes are suppressed, as they violate parity or angular momentum conservation). In the following, the $5p^5 6s[3/2]_1$ state will be abbreviated as $5p^5 6s$, omitting the angular momentum configuration for simplicity. Energetically above the $5p^5 6s$ configuration lie the $5p^5 6p$ and $5p^5 6p'$ configurations, with only the states with even total angular momentum ($J = 0, 2$) shown in Fig. 3.3(b). Qualitatively, these resemble the potential energy curve of the $5p^5 6s$ configuration, with pronounced potential energy wells at equilibrium distances around 2.9 Å.

Previous work [46] suggested the exploitation of the second excimer continuum emission on the $5p^5 6s[3/2]_1 \rightarrow 5p^6$ transition in dense xenon ensembles for the thermalization of photons. Considering an ensemble of excimers in the $5p^5 6s$ state, the occupation of the levels forming within the bound part of the potential energy curve is expected to be thermally equilibrated in frequent collisions between excimers and surrounding xenon atoms. Similarly as with the rovibronic levels in dye molecules, this could then enable the thermalization of photons emitted on transitions from this manifold to the dimer ground state. In Sec. 3.3, evidence from previous investigations will be presented, indeed indicating a thermalization of this quasimolecular collisional manifold. However, the large potential-well depth of the excimer state's potential curve (in combination with the incline of the ground state's potential curve at small internuclear distances) leads to a large Stokes shift. This causes the emission on the second excimer continuum, which is centered around 172 nm, to be spectrally too remote from the absorption on the $5p^6 \rightarrow 5p^5 6s$ transition. Although spectrally broad, with a full width at half maximum (FWHM) of about 13 nm, the spectral overlap between absorption and emission is rather small (the spectral emission profile does not extend into the spectral region with significant absorption strength). As a consequence, in a microcavity environment based on the best mirrors currently available in the VUV spectral range, the reabsorption probability during the photon storage time would be too low to establish a sequence of closed-loop cycles of absorption and subsequent reemission events, as necessary for the complete thermalization of photons[2]. This constitutes the main drawback of the homonuclear xenon system.

Heteronuclear Systems

Heteronuclear noble gas mixtures might alleviate the problem of insufficient (re)absorption, as their excimer potential wells are reported to be much shallower than that in the homonuclear xenon system [87, 88]. This is expected to cause a reduced Stokes shift between absorption and emission, assuming favorably shaped (i.e. flat) ground state potential energy curves. In the context of this work, heteronuclear dimers encompass mixtures between xenon and one of the other stable noble gases (helium, neon, argon or krypton). In such mixtures, xenon is the optically active constituent, with excitation on the (atomic) absorption line near 146.9 nm.

[2] Using Eq. (2.41), an absorption coefficient of around $10\,\mathrm{cm}^{-1}$, as roughly given in the spectral overlap region [46], corresponds to an average cycle number of 0.1.

Figure 3.4 exemplarily shows the potential energy diagram of the xenon-argon system. Here, the ground state is constituted by one xenon atom in the $5p^6$ ground state and one argon atom in the $3p^6$ ground state. The (first) excimer state is constituted by one xenon atom in the $5p^5 6s$ excited state and one argon atom in the $3p^6$ ground state. The corresponding potential energy curves of the homonuclear xenon-xenon system (same data as in Fig. 3.3(b)) are indicated for comparison. It is evident that for the xenon-argon system the potential well of the excimer state is much shallower than in the xenon-xenon system. This can be understood from the mechanism of covalent bonding: due to the reduced number of occupied electron orbitals in an argon atom, each electron is more strongly bound to the nucleus. Consequentially, the "shared" electron in the covalent bond can mediate only a weaker attraction. The ground state potential energy curve in the heteronuclear dimer system closely resembles that of the ground state in the homonuclear dimer system, only differing in the slope of the potential energy barrier at small internuclear distances. All told, it is expected that the Stokes shift in such a heteronuclear system is much smaller than in the homonuclear xenon-xenon system. This renders heteronuclear dimer systems an attractive candidate as a thermalization mediator for VUV photons, as here the emission on the *heteronuclear* second excimer continuum could become subject to a stronger reabsorption probability within the gas mixture.

3.3 Previous Spectroscopic Investigations of Xenon Dimer Systems

In [46], addressing the same experimental context as the present thesis, the absorption and emission on the $5p^6 \leftrightarrow 5p^5 6s$ transition of dense xenon dimer environments was investigated. It was observed that the long-wavelength edge of the absorption profile (red absorption edge) shifts by multiple nanometers when the sample pressure is increased, which was attributed to the shape of the potential energy curves and a smaller (average) internuclear distance for increased densities [89, 90]. More quantitatively, the characteristic wavelength $\lambda_{100\,\mathrm{cm}^{-1}}$ was introduced, denoting the spectral position at which an absorption coefficient of $\alpha = 100\,\mathrm{cm}^{-1}$ is reached. The corresponding value increased from $\lambda_{100\,\mathrm{cm}^{-1},\,20\,\mathrm{bar}} = 153.7\,\mathrm{nm}$ at a sample pressure of 20 bar to $\lambda_{100\,\mathrm{cm}^{-1},\,130\,\mathrm{bar}} = 160.1\,\mathrm{nm}$ at the highest investigated pressure of 130 bar. The emission profile for a pressure of 10 bar was observed to be centered around 172.2 nm with a FWHM of 13.3 nm; this could be identified as the emission on the second excimer continuum [91]. Increasing the pressure, the center emission wavelength shifted gradually to a value of 175.3 nm upon reaching the critical point at 58.4 bar. This shift cannot be explained by the shape of the potential energy curves, but a similar observation had been made previously in liquid xenon samples [92]. For even higher pressures, the center emission wavelength did not shift any further. With these spectroscopic data, the Kennard-Stepanov relation, Eq. (2.25), could be validated for pressures as high as 130 bar at room temperature, well within the supercritical regime. This suggests that xenon can broadly be considered a prospective thermalization medium for the Bose-Einstein condensation of VUV photons; despite the relatively large spectral gap between the absorption and the emission profiles. In the following, a brief overview about the work of other research

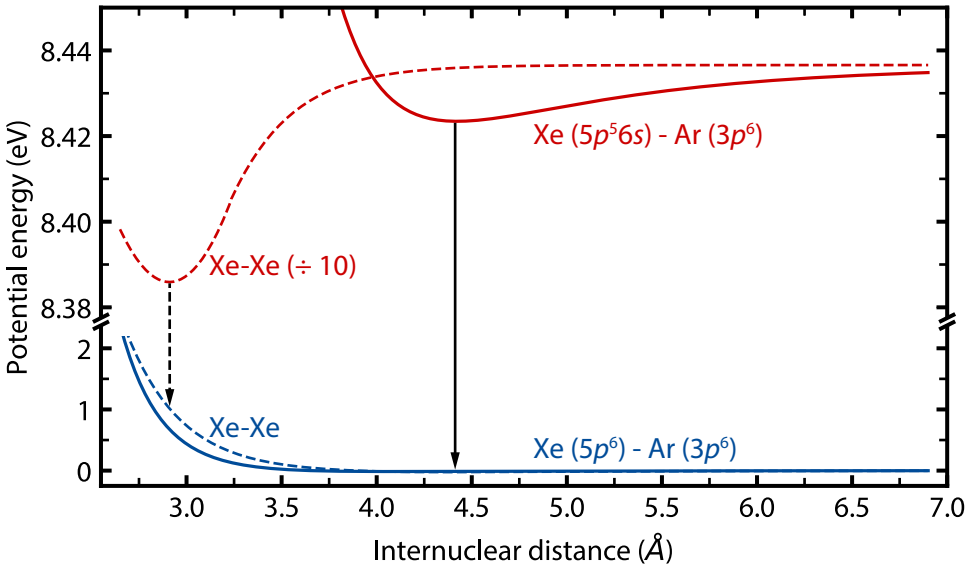

Figure 3.4: Potential energy diagram of the heteronuclear xenon-argon system (blue and red solid lines) [87]. The quasimolecular states are formed by a xenon atom, either in the electronic $5p^6$ ground state or $5p^5 6s$ excited state, and an argon atom in the $3p^6$ ground state. The potential curves of the homonuclear system are additionally shown for comparison (dashed lines, data from Fig. 3.3). For the potential energy curve of the homonuclear excimer (dashed red line), the depth of the potential well, D_e in Eq. (3.1), has been scaled down by a factor of ten (while conserving the asymptotic energy level) to allow for a visualization on the same scale as for the potential curve of the heteronuclear excimer. The vertical arrows indicate radiative relaxation from the excited to the ground state at the equilibrium distances of the homo- and heteronuclear excimer systems, respectively.

groups with relevance for the investigations of the present thesis will be given.

3.3.1 Homonuclear Xenon System

Two-photon spectroscopy is a tool widely applied for the investigation of xenon (and other species), as it allows to tremendously extend the experimentally accessible spectroscopy range. Degenerate (involving two identical photons) two-photon excitation of the $5p^6 \rightarrow 5p^5 6p$ and $5p^5 6p'$ allowed transitions has previously been recorded for pressures as high as 13 bar [72, 93–96]. Exploiting higher-order multipole contributions, forbidden transitions have also been probed [97, 98]. In most cases, the detection is realized by monitoring the second excimer continuum emission around 172 nm or the infrared radiation stemming from intermediate transitions after initial excitation. Further, multiphoton ionization spectroscopy has been performed based on two-photon-resonant states for both atomic and diatomic xenon [99–102]. Literature on *nondegenerate* two-photon spectroscopy (involving two different photons) is generally less abundant. It is mainly used in photoionization experiments [103, 104]. Spectroscopic investigations below the ionization threshold are not known. The available literature is, however, limited to pressures of a few bar, at which point the line broadening of the spectral profiles is below the thermal energy at room temperature. This indicates the need to perform two-photon spectroscopy also of dense samples, as will be presented in Chap. 5.

3.3.2 Heteronuclear Xenon Systems

Heteronuclear mixtures between xenon and the lighter noble gases argon and krypton are abundantly covered by previous studies due to their early consideration as active media for lasers in the VUV spectral range, with much attention devoted to kinetic studies after excitation [105–107]. VUV emission spectra of the xenon-argon and xenon-krypton systems have been investigated in [88], revealing continuous emission features around 150 and 156 nm, respectively. These measurements were conducted using condensed targets of either argon or krypton, which were then "bombarded" by xenon atoms excited to the metastable $5p^5 6s[3/2]_2$ state in an electric discharge. Other work [108, 109] reports an emission spectrum of argon-xenon mixtures composed by two distinct emission features, one around 147 nm and one around 173 nm – interestingly, no emission around 150 nm is observed, which might be rooted in the fundamentally different excitation scheme (based on alpha particles impinging onto a sample target). It is shown that the emission feature around 173 nm becomes stronger as the relative xenon contribution is increased; accordingly, this spectral component is attributed to the formation of homonuclear xenon-xenon dimers. Discharge-based measurements [110] in the xenon-neon system reveal an emission feature at 148.7 nm, which has been tentatively attributed to the emission of a xenon-neon excimer state. To the best of the author's knowledge, no VUV emission spectra of xenon-helium mixtures are currently available. Absorption measurements have been recorded for mixtures between xenon and all the lighter noble gases [87, 111, 112], showing strongly asymmetric absorption profiles with rapidly declining red edges. The blue edges, besides dropping off much less rapidly, exhibit a number of discrete bands, which are attributed to the formation of heteronuclear quasimolecules.

These measurements show that heteronuclear mixtures between xenon and other noble gases exhibit features that cannot be explained by the optical properties of atomic or dimerized xenon alone, strongly suggesting the formation of heteronuclear quasimolecules. The available literature, though, only covers the low-pressure regime, with total sample pressures in the range below 1 bar. Many of the studies on VUV emission spectra are based on the excitation of higher-lying electronic states or even nonoptical excitation schemes such as electric discharges. As a consequence, the obtained emission spectra might exhibit features which would not be observed in other, spectroscopically more precise excitation channels. All in all, although useful for a rough estimation of beneficial parameter ranges, the available literature is only partially comparable to the conditions (likely) prevailing in a future microcavity environment for Bose-Einstein condensation of VUV photons. This highlights the need to conduct spectroscopic investigations of dense xenon-noble gas systems; corresponding measurements will be presented in Chap. 6.

4 Experimental Environment

This chapter will provide an overview about the experimental platforms and techniques employed to conduct the measurements presented in this thesis. Due to the nature of the investigated spectral regime, all spectroscopic experiments need to be conducted in a vacuum environment, which will be briefly introduced in the beginning, along with other mechanical instrumentation, such as high-pressure cells. Subsequently, the optical instrumentation, such as laser systems and other light sources will be covered. The chapter closes with a presentation of available photon-detection units.

4.1 Vacuum Environment

Radiation in the vacuum-ultraviolet spectral regime (100 nm − 200 nm) is subject to absorption by atmospheric gases, prominently manifested in the Schumann-Runge bands, a set of distinct absorption lines of (molecular) oxygen between 176 nm and 192 nm [113–115]. Hence, the experiments presented in this thesis are conducted in an atmosphere-free environment, realized in vacuum chambers made from stainless steel [46, 116]. On two sides, the vacuum chambers are equipped with polycarbonate windows that can be removed for manual access for alignment purposes. KF-standard vacuum flanges allow for attachment of auxiliary components, such as pumps, pressure gauges, viewports and electrical feedthroughs. An optical breadboard installed at the bottom of the vacuum chamber facilitates the precise positioning of high-pressure cells and optical components in its interior. A gas feedthrough allows to connect the high-pressure cell(s) inside the vacuum chamber to the gas piping system outside of it.

The vacuum chambers are evacuated by a two-stage pump system. A dry-running scroll pump (*Pfeiffer Vacuum* HiScroll 6 or HiScroll 18) employed as backing pump allows to reach pressures in the 10^{-1} mbar range. A subsequent turbomolecular pump (*Pfeiffer Vacuum* HiPace 80 or *Leybold* Turbovac 360CSV) brings vacua in the 10^{-4} mbar range within reach (generally classified as high vacuum). Pressures are monitored with Pirani pressure gauges. Starting from atmospheric pressure, it takes between 30 minutes and 3 hours to reach vacua in which measurements are feasible, depending on the specific chamber and pump configuration. The attenuation of VUV radiation at a residual chamber pressure of $p = 1 \times 10^{-4}$ mbar can be estimated by assuming it to be dominated by oxygen and that the light propagates for a distance of $l = 100$ cm from its creation to its detection. The maximum absorption coefficient of air (at 1 bar pressure) is around $\alpha_{\mathrm{air,1\,bar}} = 300\,\mathrm{cm}^{-1}$ at a wavelength of 140 nm. Considering the share of oxygen in the atmosphere, this translates into an absorption coefficient of $\alpha = 6.3 \times 10^{-6}\,\mathrm{cm}^{-1}$ or a residual attenuation of less than 0.1 %, clearly negligible for the experiments conducted here.

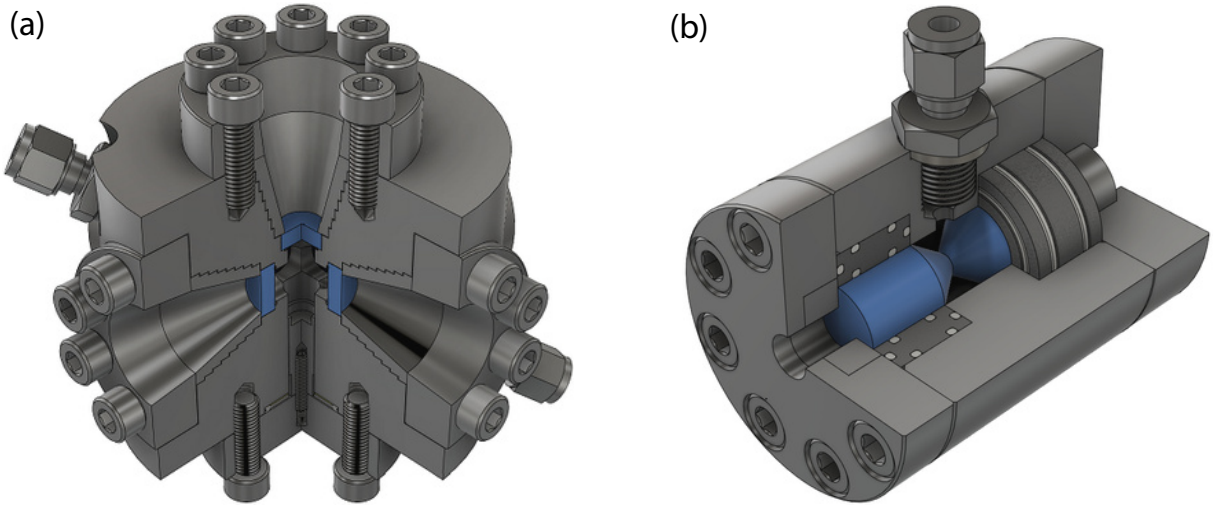

Figure 4.1: High-pressure cells used for spectroscopic measurements presented in this thesis, with windows highlighted in blue color [118] – **(a)** Five-window cell with realizable optical path lengths between 5 mm and 20 mm (using combinations of plane and step windows). **(b)** Two-window cell with an optical path length of 200 µm.

4.2 High-Pressure Cells

The most controllable approach to conduct investigations of gaseous samples is the use of high-pressure cells to confine the samples over extended periods of time[1]. In the following, the two different high-pressure cells used for the experiments presented here will be illuminated individually, as they exhibit fundamentally different geometries. More details about these high-pressure cells can be found in [46, 117].

4.2.1 Five-Window Cell

The body of the high-pressure cell shown in Fig. 4.1(a) is made out of stainless steel and has six lateral openings. The opening on the bottom of the cell is covered with a blank flange, using a nickel gasket for sealing[2]. The remaining five openings (on the top and on either side of the cell, each apart by an angle of 90°) are designed to accommodate windows for optical access. The windows exhibit a diameter of 15 mm and a thickness of 5 mm and are kept in place by stepped inserts, which in turn are pressed toward the cell by flanges. The sealing is realized between the cell body and the windows, employing commercially available c-shaped rings from the supplier *GFD Dichtungssysteme*. The high-pressure cell further exhibits two ports for connection to the gas piping system (Sec. 4.3).

In the scope of this work, the cell is equipped with either magnesium fluoride (MgF_2; *Korth*

[1] An occasionally used alternative are gas jets expanding from small-aperture nozzles. These, however, have the drawback of a continuously needed flow of gas, greatly raising the overall gas consumption.
[2] The cell was originally designed for a different experimental setup, where convenient manual access to the inner part of the cell without removing any of the windows was imperative.

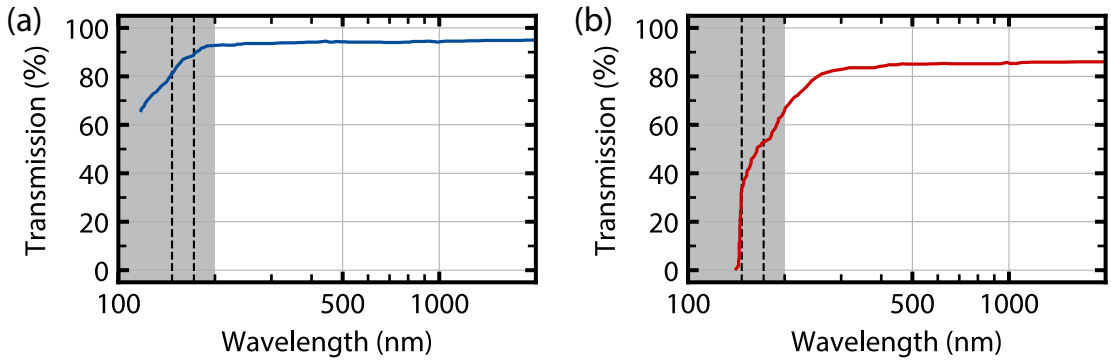

Figure 4.2: Transmission profiles of available window materials [119, 120] – **(a)** Magnesium fluoride (MgF_2) exhibits a relatively high transmissivity throughout the VUV, visible and infrared spectral ranges (shown here for an 81 mm-thick sample). The gray area indicates the VUV spectral range between 100 nm and 200 nm. The black dashed lines indicate the spectral positions of xenon's (atomic) absorption, at 146.9 nm, and second excimer continuum emission, at 172 nm, respectively. **(b)** Sapphire (Al_2O_3) generally exhibits a lower transmissivity than MgF_2, particularly in the VUV (shown here for a 10 mm-thick sample).

Kristalle) or sapphire (Al_2O_3, *CrysTec*) windows, the latter being much more robust as the former, with moduli of rupture of 60 and 1200 MPa, respectively [119, 120]. However, with a transmission range spanning from around 118 nm far into the infrared, only the windows made from MgF_2 allow for optical access throughout the VUV spectral range (Fig. 4.2). The transmissivity of sapphire windows, in contrast, drops rapidly for wavelengths below 200 nm. Hence, all cell openings through which VUV radiation is to be guided are equipped with MgF_2-windows. The other openings are equipped with sapphire windows, particularly those only used for alignment purposes or visible inspection during measurements. In this configuration, the high-pressure cell can withstand gas pressures of up to 100 bar; a limitation dominated by the rupture strength of the used MgF_2-windows.

The most evident advantage of using a five-window cell as described here is the ability to monitor radiation generated in the gas through a lateral window under an angle of 90° relative to the direction of the incoming excitation beam. This tremendously reduces the amount of stray light collected by the detection unit, significantly increasing the quality of the obtained data. Using a window geometry as described above, the high-pressure cell exhibits two intersecting optical axes, each with an optical path length of 2 cm. Using off-the-shelf step windows, however, different optical path lengths can be realized, bringing about multiple benefits. On the one hand, in absorption measurements different regions of an absorptive spectral feature can be resolved (the shorter the optical path length, the higher the maximum resolvable absorption coefficient). On the other hand, in emission measurements, the distance that emitted radiation has to traverse through gas can be drastically reduced. This is of utmost importance when investigating emission features in the spectral vicinity of absorptive features, as reabsorption processes on the path from the origin of the emitted light to the cell window could significantly alter the observed emission spectrum.

Although versatilely employable, the five-window cell has the disadvantage that optical path lengths in the sub-millimeter range as needed for absorption measurements (Sec. 6.2) are experimentally hardly realizable, as these would require additional step windows tailored to a certain target optical path length. Besides the fact that these can be obtained only at great expense, experience suggests that configurations with two opposing step windows less than 1 mm apart are very susceptible to rupture, due to high transversal stress upon filling the cell with gas.

4.2.2 Two-Window Cell

The cell shown in Fig. 4.1(b) was constructed to address some of the five-window cell's shortcomings. It is equally made from stainless steel, but has only two, mutually opposing openings. In each opening, an insert made from carbon-reinforced PTFE (Teflon) is located, in turn accommodating a 30 mm-long, 20 mm-wide cylindrical window conically tapered on the inward-facing end. A flange is used on either side of the cell to press the PTFE-window assembly toward the cell. The sealing is realized by multiple PTFE rings circumventing the windows and the PTFE inserts at various positions. A lateral hole in the cell body allows for connection to the gas piping system. In the current configuration, the optical path length between the inner window facets is 200 µm. The window tip's conical shape mitigates the transversal stress exerted on the windows by gas flowing into the cell during the filling process, rendering this design superior to one based on the use of step windows for the realization of sub-millimeter optical path lengths. This high-pressure cell has been proven to withstand gas pressures as high as 150 bar.

4.3 Gas Piping System and High-Pressure Generation

For all spectroscopic investigations in this thesis, xenon gas from the supplier *Air Liquide* is used. Its grade is 4.8, implying a purity of 99.998 %, the main contaminants being krypton, argon and nitrogen [121]. The gas bottles have a volume of 1 L and exhibit a factory-provided filling pressure of around 56 bar. To direct the flow of gas from the bottle to the high-pressure cells, a gas piping system with components from the manufacturer *Gyrolok* is used. The maximum pressure ratings of the 6 mm-outer-diameter stainless steel pipes (2000 bar), the valves (356 bar) and the pressure gauges (250 bar) each far exceed the pressure range accessible with the utilized high-pressure cells.

4.3.1 Homonuclear Samples

Figure 4.3 shows the gas piping system employed for the preparation of homonuclear xenon samples, as investigated in Chap. 5. Since this work aims to also investigate xenon samples at pressures exceeding the (initial) bottle pressure, a technique to fill the high-pressure cell to pressures beyond the current gas bottle pressure is needed. For this, a sample cylinder (*Hoke*

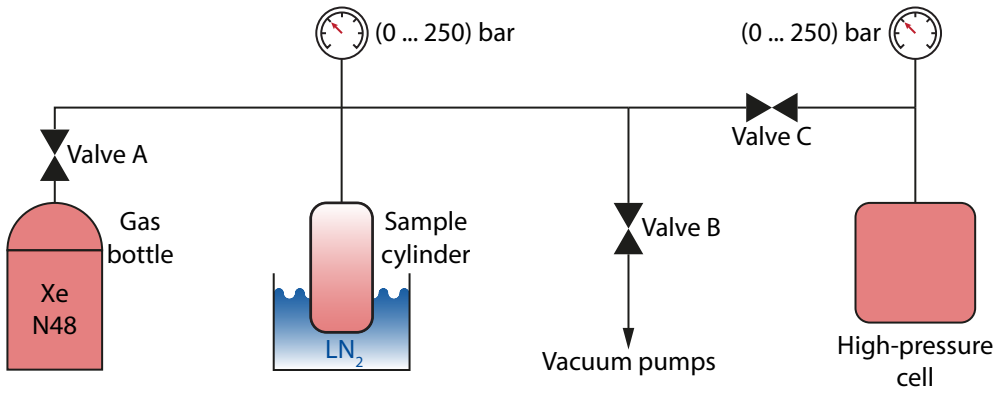

Figure 4.3: Gas piping system for the preparation of *homonuclear* xenon samples. Valve A is located directly at the gas bottle. To achieve pressures beyond that in the gas bottle, the xenon-filled sample cylinder can be immersed in liquid nitrogen (LN_2), leading to a local increase of the gas density. Upon heating the sample cylinder to ambient temperature with valve A closed, the pressure in the high-pressure cell exceeds the initial pressure in the gas bottle. The pressure gauges have a measurement range from 0 to 250 bar. Prior to being filled with gas, the gas piping system is evacuated using the same vacuum pumps as for the evacuation of the vacuum chambers.

4HSY30) with a volume of 30 mL is utilized. Initially, the whole gas piping system is evacuated using the same pump system as for the evacuation of the vacuum chambers (Sec. 4.1), with valves B and C being open. Subsequently, valve B is closed and valve A, located directly at the xenon gas bottle, is opened and the gas piping system including the high-pressure cell is filled with xenon gas. As the volume of the gas bottle is much larger than that of the gas piping system, the pressure in the latter is now close to the initial pressure in the gas bottle. Subsequently, valve C is closed, sealing off the high-pressure cell from the rest of the gas piping system. The sample cylinder is now cooled down by immersion in liquid nitrogen (LN_2), leading to a local density increase of xenon in its interior and the formation of liquid or even solid xenon. After a certain time, valve A is closed and valve C is opened. The sample cylinder is now heated back to ambient temperature and the xenon expands; now, however, with the gas bottle sealed off from the gas piping system, into a much smaller volume. Using this technique, if necessary in successive iterations, pressures well within the supercritical regime (beyond 58.4 bar) can be achieved. The limits of this approach are given by the maximum pressure rating of the sample cylinder, 124 bar.

4.3.2 Heteronuclear Samples

Figure 4.4 shows the gas piping system for the preparation of heteronuclear gas mixtures, as investigated in Chap. 6. The main difference compared to that for the preparation of homonuclear xenon samples is an additional branching to a gas bottle containing a non-xenon noble gas and an additional low-pressure gauge near the high-pressure cell. The latter is needed as mostly mixtures with small xenon contributions in the order of a few millibar are to be investigated. The gauge has a measurement range from −1 bar to 0 bar, relative to ambient pressure (it dis-

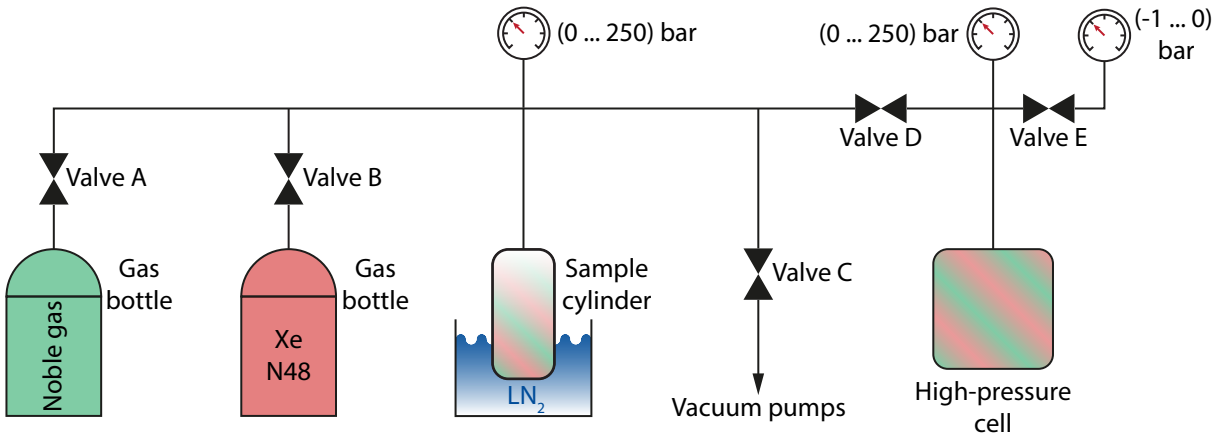

Figure 4.4: Gas piping system for the preparation of *heteronuclear* xenon-noble gas samples. Valves A and B are located directly at the respective gas bottles. Unless otherwise stated, the pressure gauges have a measurement range from 0 to 250 bar. The low-pressure gauge with a measurement range from −1 bar to 0 bar is used to fill small amounts of xenon into the gas piping system.

plays −1 bar for a fully evacuated system). For the preparation of gas mixtures, the ratio of the compartment volumes on either side of valve D needs to be known, as it governs the expansion of gas contents from one compartment into the other. This ratio is determined experimentally, but is for now assumed to be 1/3 for illustrative purposes. The following steps illuminate the preparation of heteronuclear xenon-noble gas mixtures, using the example of a xenon-helium mixture with a xenon concentration of 200 ppm and a total pressure of 75 bar:

1. With the valves C, D and E open, the whole gas piping system is evacuated (valves A and B are located right at the gas bottles).

2. Valve C is closed and valve B is opened, filling the gas piping system to a xenon pressure of 60 mbar, using the low-pressure gauge. Valve B is closed again.

3. Valves D and E are closed and valve C is opened, removing the xenon from the gas piping system (but not the high-pressure cell).

4. Valve C is closed and valve A is opened, filling the gas piping system (except for the high-pressure cell) to a helium pressure of 100 bar. At this point, valve D separates the gas piping system, filled with helium, and the high-pressure cell, filled with xenon. Valve A is closed again.

5. Valve D is opened, allowing the two previously compartmentalized gases to mix. Helium flows into the high-pressure cell and xenon flows into the gas piping system. In the resulting mixture, the helium partial pressure is $3/4 \cdot 100\,\text{bar} = 75\,\text{bar}$, the xenon partial pressure is $1/4 \cdot 60\,\text{mbar} = 15\,\text{mbar}$, resulting in a relative xenon concentration of 200 ppm (the negligibly small contribution of the xenon partial pressure to the total sample pressure is tacitly ignored).

The scale division of the low-pressure gauge is 20 mbar, at first glance seeming to prevent the accurate preparation of mixtures with xenon contributions below $1/4 \cdot 20\,\text{mbar} = 5\,\text{mbar}$. However, this obstacle can be overcome, by conducting the procedure repetitively *without* filling any buffer gas into the gas system in step 4. With every iteration, the amount of xenon in the high-pressure cell is reduced in a controlled way, in this example by a factor of 4. In the experiments on heteronuclear mixtures between xenon and other noble gases, the xenon contributions correspond to partial pressures significantly below 1 bar, easily achievable without immersing the xenon-filled sample cylinder in liquid nitrogen. The gas bottles of the noble gases helium, neon and argon have volumes of 10 L and exhibit a factory-provided filling pressure of 200 bar, more than sufficient to prepare gas mixtures with total pressures in the order of 100 bar. Krypton, after xenon the heaviest stable and equally scarce noble gas, is available only in gas bottles with a volume of 1 L and a filling pressure of 80 bar. As its boiling temperature, 120 K, is above that of nitrogen, 77 K [77], the technique of immersing the krypton-filled sample cylinder in liquid nitrogen can be applied equally as with xenon. The purity grades of these noble gases (also from the supplier *Air Liquide*) are comparable to that of xenon.

4.4 Laser and OPO System

For most of the spectroscopic investigations presented in this thesis, a combination of a Q-switched Nd:YAG laser system and an optical parametric oscillator (OPO) system is used. The laser system (*Spectra Physics* Quanta Ray PRO 250-10) generates radiation at 1064 nm wavelength with a pulse energy of 1400 mJ, a pulse length (FWHM) of 10 ns and a repetition rate of 10 Hz. The radiation at 1064 nm wavelength is guided through two subsequent harmonic-generation stages including nonlinear KD*P crystals. In the first stage, the radiation is frequency-doubled in a type-I second-harmonic generation (SHG) process. In the second stage, the resulting light at 532 nm wavelength is then combined with the residual radiation at 1064 nm wavelength in a sum-frequency generation (SFG) process. After the SHG and SFG processes, radiation at a wavelength of 355 nm and a pulse energy of 450 mJ is available, propagating collinearly with the beam components at 532 nm and 1064 nm wavelength.

The beam encompassing radiation at the three stated wavelengths is then guided to an OPO system (*GWU* primoScan ULD/400), which – besides the actual OPO crystal – contains several other optical components, as illustrated in Fig. 4.5. Once inside the OPO housing, a dichroic mirror splits off the beam component at 355 nm wavelength and transmits the components at 532 nm and 1064 nm wavelength. A share of around 60 % of the light at 1064 nm wavelength is subsequently split off for other instances of sum-frequency generation processes within the OPO system (see below); the remainder leaves the OPO system together with the component at 532 nm wavelength and is available for other applications. The radiation at 355 nm wavelength is used to optically pump the system's centerpiece, the barium-borate OPO crystal. In a parametric process exploiting the crystal's nonlinear optical properties [122], an incoming photon at 355 nm wavelength is converted into a pair of two photons, the lower-energetic of which is histor-

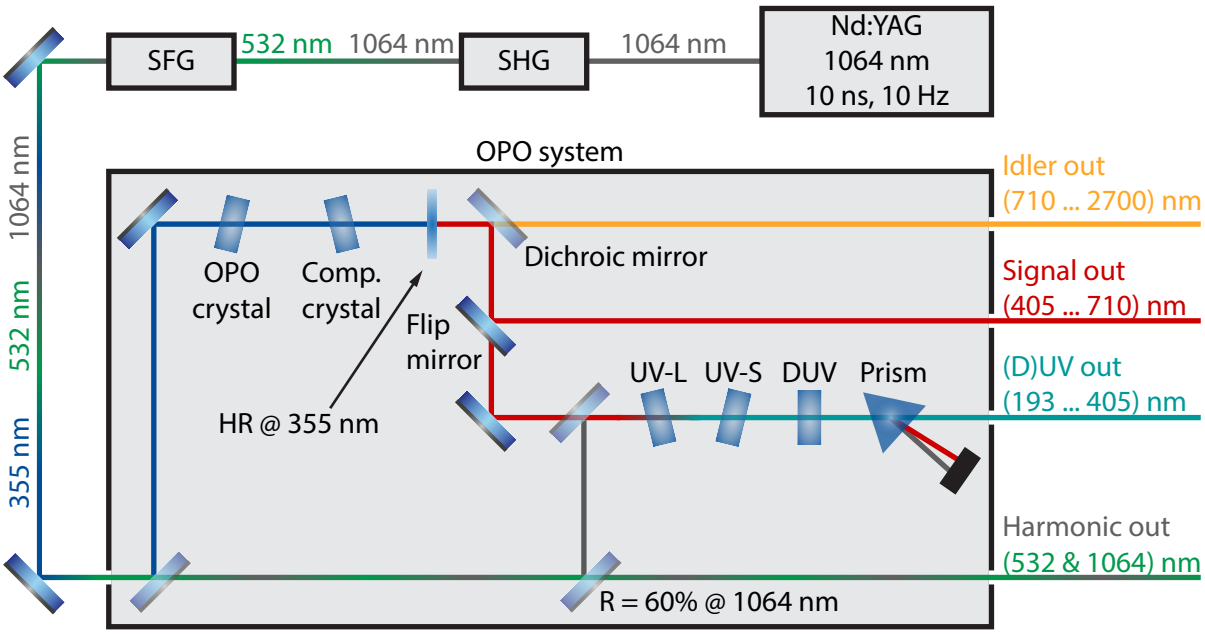

Figure 4.5: Schematic of the laser and optical parametric oscillator (OPO) system. Radiation at 1064 nm wavelength from a Q-switched Nd:YAG laser is frequency-doubled and -tripled in nonlinear KD*P crystals. The beams at the three wavelengths are guided collinearly to the OPO system, where the beam component at 355 nm wavelength is split off and used to pump the OPO crystal. The radiation generated here, covering the wavelength range from 405 nm to 2700 nm, traverses a compensation crystal oriented opposedly to the OPO crystal. Subsequently, the beam is spectrally divided by a dichroic mirror with a separation wavelength of 710 nm, after which the idler component (710 nm − 2700 nm) leaves the system. The signal component can either be coupled out as well or be superimposed with radiation at 1064 nm wavelength and subsequently guided through multiple nonlinear crystals (UV-L, UV-S, DUV) to generate radiation in the 193 nm to 405 nm range. A prism eventually separates the remaining (D)UV, signal and 1064 nm beams and only the (D)UV component is guided out of the OPO system.

ically referred to as “idler”, whereas the higher-energetic one is referred to as “signal” photon. While energy conservation imposes the constraint $1/\lambda_{\text{signal}} + 1/\lambda_{\text{idler}} = 1/355\,\text{nm}$, the specific ratio between λ_{signal} and λ_{idler} is governed by the phase matching condition. Here, phase matching for a particular combination of target wavelengths is fulfilled by tuning the crystal angle relative to the direction of the incoming pump beam. In this way, gap-free tunable radiation in the wavelength range from 405 nm to 2700 nm can be achieved (710 nm, twice the pump wavelength, constitutes the boundary between signal and idler range). This light is guided through a compensation crystal made out of quartz glass, mirroring the orientation of the OPO crystal, so as to compensate for any transversal angle deflection due to nonnormal incidence of the pump beam onto the front facet of the OPO crystal. Subsequently, signal and idler beam are separated by a dichroic mirror, after which the idler beam leaves the OPO system without further manipulation. The signal beam can either be coupled out equally or, alternatively, be superimposed with the beam at 1064 nm wavelength previously separated. The combination of both beams is guided through three additional nonlinear crystals. The first crystal (UV-L) enables access to the wavelength range from 250 nm to 405 nm, either via second-harmonic generation of two

signal photons or, alternatively, via sum-frequency generation of a signal photon and a photon at 1064 nm wavelength. The following crystal (UV-S) covers the 210 nm to 250 nm wavelength range, via second-harmonic generation of two signal photons. The last crystal (DUV) allows access to the 193 nm to 210 nm wavelength range via sum-frequency generation of a UV-photon in the 210 nm to 250 nm range generated in the UV-S crystal and a photon at 1064 nm wavelength. A Pellin-Broca prism separates the (D)UV, signal and 1064 nm beams, and the latter two are guided into a beam trap, such that only the (D)UV light leaves the OPO system.

4.5 Third-Harmonic Generation in Dilute Gases

Although the radiation provided by the laser and OPO system presented in the previous section spans both the visible and near-infrared spectral ranges in their entirety, at short wavelengths its tunability range is limited to wavelengths just below 200 nm. With this, it well covers the wavelength range required to excite xenon samples in degenerate two-photon processes, allowing for spectral investigations such as those presented in Sec. 5.1. However, a direct excitation of xenon on its $5p^6 \rightarrow 5p^5 6s$ transition (i.e. without involvement of any higher-lying states) is not possible. To bring such measurements within experimental reach, the necessary radiation around 147 nm wavelength has to be generated in a nonlinear process from radiation accessible with the laser and OPO system. Nonlinear crystals, although generally widely employed for high-harmonic generation, cannot be used for this, as the transmission ranges of even the most UV-transparent crystals do not extend to the target wavelengths around 147 nm. An alternative is the third-harmonic generation (THG) in gases [123]. Whereas even-order harmonic generation is infeasible in gases with only one optically active atomic species due to the vanishing even-order susceptibility, the odd-order and in particular the third-order susceptibility $\chi^{(3)}$ are nonzero. Assuming the fundamental (Gaussian) beam to be focused into the gas volume, the power $\mathcal{P}_{\mathrm{harm}}$ obtained from third-harmonic generation can be found to be [124, 125]

$$\mathcal{P}_{\mathrm{harm}} \propto \frac{|\chi^{(3)}|^2}{\lambda_{\mathrm{harm}}^4} \mathcal{P}_{\mathrm{fund}}^3 |F_1(b\Delta k)|^2 \,. \tag{4.1}$$

Here, λ_{harm} is the wavelength of the light generated in third-harmonic generation and $\mathcal{P}_{\mathrm{fund}}$ is the incident power at the fundamental wavelength. The quantity $F_1(b\Delta k)$ accounts for the phase matching between fundamental and third-harmonic light, with b the confocal parameter of the focused beam and $\Delta k = k_{\mathrm{harm}} - k_{\mathrm{fund}}$ the wave vector mismatch between third-harmonic and fundamental light. In the tight-focusing limit, with $b \ll L$, where L is the length of the nonlinear medium, $F_1(b\Delta k)$ can be evaluated to be [126]

$$|F_1(b\Delta k)|^2 = \begin{cases} \pi^2 (b\Delta k)^2 e^{b\Delta k}, & \Delta k < 0 \\ 0, & \Delta k \geq 0 \,. \end{cases} \tag{4.2}$$

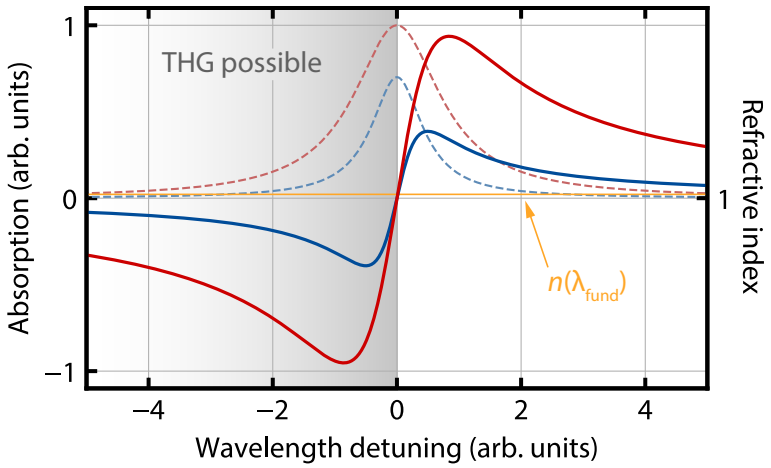

Figure 4.6: Illustration of the absorption and refractive index around an atomic resonance. Absorption profiles are indicated by dashed lines, the corresponding refractive indices are indicated by solid lines [127]. The blue curves correspond to a sample with comparably low density (and associated weak absorption), the red curves correspond to one with a comparably high density (and associated stronger absorption). The spectral range accessible by third-harmonic generation (gray area) is limited by the phase matching condition, requiring the refractive index at the harmonic wavelength to be smaller than the refractive index $n\,(\lambda_{\mathrm{fund}})$ at the fundamental wavelength [123].

The phase matching condition $\Delta k \overset{!}{<} 0$ signifies that the harmonic light needs to propagate faster than the fundamental light through the medium. Otherwise, in an illustrative picture, the harmonic wave would be overtaken by the fundamental wave and destructive interference among successively generated harmonic wave trains would inhibit the built-up of a persistent harmonic wave. In other words, the condition is met if the refractive index at the harmonic wavelength is smaller than the refractive index at the fundamental wavelength. Although this is not possible in spectral regions with only normal dispersion ($\mathrm{d}n/\mathrm{d}\lambda < 0$), the situation changes around resonances, which entail spectral regions with anomalous dispersion ($\mathrm{d}n/\mathrm{d}\lambda > 0$). As illustrated by Fig. 4.6, the phase matching condition can be fulfilled on the short-wavelength (blue) side of a resonance. In this work, the approach of third-harmonic generation of blue light around 441 nm wavelength in a low-pressure xenon environment was chosen, exploiting the blue side of the $5p^6 \rightarrow 5p^5 6s$ transition for negative dispersion (such that wavelengths below 147 nm can be accessed). The phase matching $F_1(b\Delta k)$ for a certain fundamental wavelength is optimized by tuning of the gas pressure (typically up to 300 mbar). The assembly used for this purpose, in the following referred to as THG cell, is shown in Fig. 4.7(a). The xenon gas is confined to a modified CF16-crosspiece (*Vacom* X16-316) welded to a drilled-through KF50-flange, which in turn is attached to the vacuum chamber. Along one axis, the THG cell is equipped with a borosilicate window (*Vacom* VPCF16B-L) on one opening and a MgF_2-window (*Korth Kristalle*) on the opposite opening, with an optical path length of $L = 10$ cm in between. Along the other axis, one opening is used for the connection to the gas piping system and the opposite opening houses a borosilicate window for visual inspection.

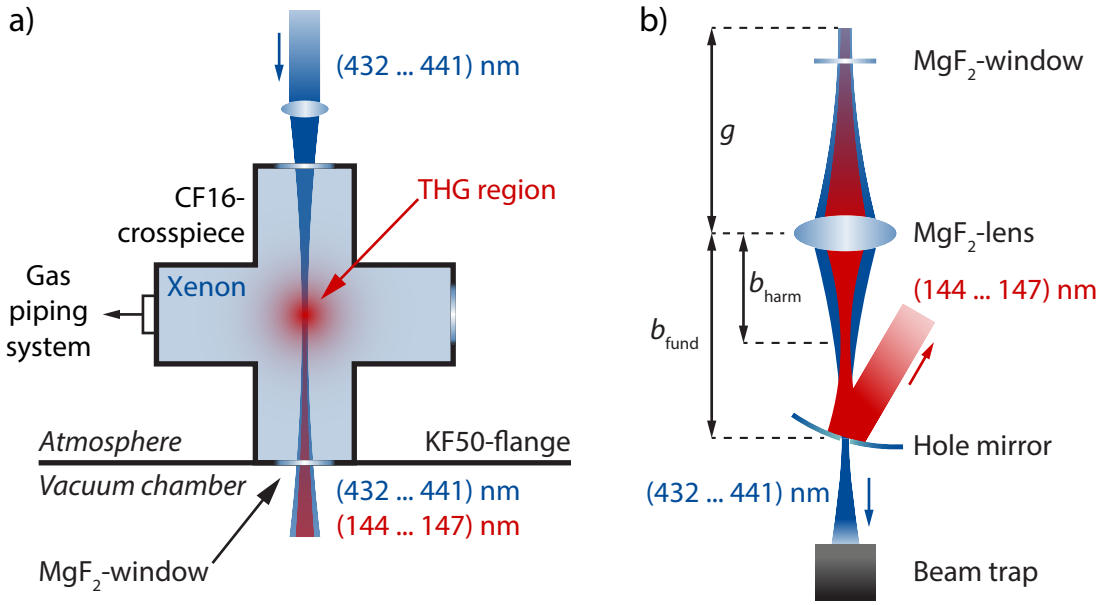

Figure 4.7: Sketch of the experimental setup for the generation of radiation between 144 nm and 147 nm wavelength – **(a)** Centerpiece is a modified CF16-crosspiece attached to a vacuum chamber via a KF50-flange and filled with xenon gas. Along the vertical axis, a beam of blue light with a wavelength between 432 nm and 441 nm coming from the OPO system is guided through a borosilicate window and focused into the cell's center, where it is converted to VUV light in a third-harmonic generation (THG) process. Both the THG and the fundamental blue beam pass through a MgF_2-window into the vacuum chamber. The other two ports of the cell house a window for visual inspection and a connection to the gas piping system. **(b)** Separation of the harmonic light from the fundamental blue light. A MgF_2-lens is placed at a distance g from the center of the THG cell (drawing not to scale). Its chromatic dispersion leads to different focal positions (b_{fund} and b_{harm}, respectively) for the two beams, allowing for their separation with a centrally-pierced mirror ("hole mirror"). The (unwanted) fundamental blue light is guided into a beam trap, the harmonic light is collimated and available for measurements.

Blue light in the wavelength range from 432 nm to 441 nm is focused into the center of the THG cell using an achromatic lens with a focal length of 100 mm (*Thorlabs*). With a beam diameter of 10 mm in front of the lens, a spot size of 6 µm is reached at the center of the THG cell; corresponding to a confocal parameter around $b = 0.5$ mm, clearly fulfilling the tight-focusing limit. Within this focus region, light in the wavelength range from 144 nm to 147 nm can be generated, which then leaves the THG cell together with the fundamental blue light through the MgF_2-window into the vacuum chamber. The conversion efficiency of the THG is rather low (in literature, efficiencies in the order of 10^{-5} are reported [103]), resulting in the need to separate the weak THG light from the comparatively strong fundamental blue light. This proves experimentally challenging, as bandpass filters for light in the VUV typically offer transmissivities around 30 %, while rejection factors for visible light are at best $1/1000$. Hence, even two consecutive filters could only barely suppress the fundamental blue light sufficiently, not even considering the inevitable suppression of VUV light. Further, with the energy density of the fundamental blue light being close to the laser-induced damage threshold of available bandpass filters, a frequent replacement of these delicate optical components would be necessary.

Here, a different approach was chosen, based on the chromatic dispersion of a MgF_2-lens (*Thorlabs*) and subsequent beam separation in a centrally-pierced mirror [46], as shown in Fig. 4.7(b). Within the vacuum chamber, the copropagating beams around 441 nm and 147 nm wavelength, pass through a MgF_2-lens, whose chromatic dispersion leads to both beams being focused to different planes. The focal length $f(\lambda)$ at a certain wavelength λ is given by the lensmaker's equation (in thin-lens approximation),

$$\frac{1}{f(\lambda)} = ((n(\lambda) - 1)\left(\frac{1}{R_1} - \frac{1}{R_2}\right), \tag{4.3}$$

with R_1 and R_2 the radii of curvature of the lens surfaces. The refractive index $n(\lambda)$ in turn is governed by the Sellmeier equation [127],

$$n(\lambda)^2 - 1 = \frac{0.48755108\,\lambda^2}{\lambda^2 - 0.04338408^2} + \frac{0.39875031\,\lambda^2}{\lambda^2 - 0.09461442^2} + \frac{2.3120353\,\lambda^2}{\lambda^2 - 23.793604^2}\,. \tag{4.4}$$

The numerical constants are a material property of MgF_2 [128]. The plano-convex lens used here has a nominal focal length of 75 mm at the design wavelength of 633 nm and a radius of curvature of the convex side of $R_1 = 28.3\,\text{mm}$ ($R_2 = \infty$). Placed at a distance $g = 155\,\text{mm}$ away from the center of the THG cell, it focuses the harmonic light to a plane at a distance of $b_{\text{harm}} = {}^{g \cdot f(147\,\text{nm})}/_{g - f(147\,\text{nm})} = 92\,\text{mm}$ from its center. The focal plane of the fundamental blue light, contrarily, lies $b_{\text{fund}} = 142\,\text{mm}$ away from the center of the lens, coinciding with the position of a concave VUV-mirror with a radius of curvature of $R = -100\,\text{mm}$. Through its center a hole with a diameter of 1 mm has been drilled, allowing the blue fundamental light to pass through the mirror and subsequently be guided into a beam trap. The curved mirror's focal length $f = R/2$ by design corresponds to the distance between its surface and the focal plane of the harmonic light (in other words, the difference $b_{\text{fund}} - b_{\text{harm}}$), leading to a collimated beam of VUV light after reflection off the mirror surface. For other wavelengths in the target range from 144 nm to 147 nm, the deviations of b_{fund} and b_{harm} are in the order of 2 mm and hence smaller than typical positioning uncertainties of the optical elements in the vacuum chamber.

As a characterization of the THG process, Fig. 4.8(a) shows spectra of the THG light for different fundamental wavelengths between 432 nm and 441 nm (recorded with a CCD camera-based spectrometer that will be covered in Sec. 4.7). The xenon pressure within the THG cell was 30 mbar. Clearly, a change of the fundamental wavelength results in a corresponding spectral shift of the harmonic signal. The conversion efficiency appears to be highly wavelength-dependent, with the envelope of the obtained spectra exhibiting a peak around 146.2 nm (the pulse energy of the fundamental light is constant over the relevant wavelength range). This behavior is mirrored by Eq. (4.2) and can be attributed to the interplay between absorption and refractive index in the xenon gas around its resonance. Figure 4.8(b) shows the wavelengths with maximum THG signal as a function of the fundamental wavelength. A linear function fitted to the data yields

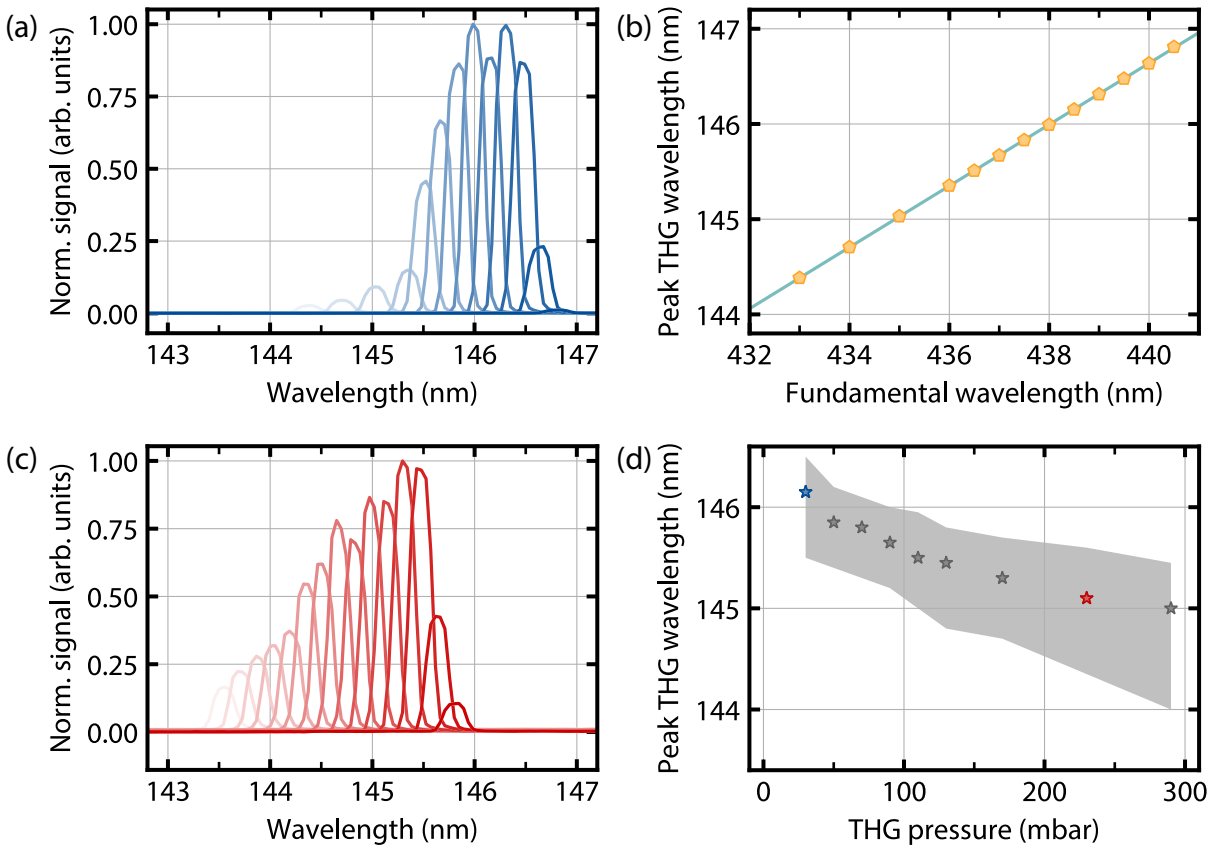

Figure 4.8: Characterizing measurements of the third-harmonic generation (THG) – **(a)** Spectra of the radiation generated in the THG process for different wavelengths of the blue fundamental light with a gas pressure inside the THG cell of 30 mbar. Spectra resulting from fundamental light at longer wavelengths are indicated by a more opaque coloring. The width of the observed peaks (around 0.2 nm) results from the finite resolution of the spectrometer. **(b)** Dependency of the peak THG wavelength on the wavelength of the fundamental light (yellow, data from (a)). A linear function (cyan) fitted to the data yields a slope of (0.32 ± 0.05). **(c)** Data similar to those in (a), but with a higher xenon pressure inside the THG cell of 230 mbar, enabling the conversion of shorter-wavelength light. **(d)** Dependency of the wavelength with highest conversion efficiency on the gas pressure inside the THG cell. The blue and red colored data points are obtained from the the data shown in (a) and (c) in corresponding colors. The gray shaded area indicates the FWHM of the envelopes around each set of spectra.

a slope of (0.32 ± 0.05), showing only a minor deviation from the expected value of $1/3$. Changing the gas pressure within the THG cell results in a shift of the wavelength with maximum conversion efficiency, as indicated in Fig. 4.8(c), showing data similar to those from Fig. 4.8(a), but with a higher xenon pressure of 230 mbar inside the THG cell. As this sample exhibits a broader absorption profile and a more pronounced refractive index change, the conversion of shorter-wavelength blue light is enabled. Figure 4.8(d) shows the dependency of the wavelength with highest conversion efficiency (spectral position of the peak of the envelope) on the gas pressure within the THG cell. Besides exhibiting a spectral shift, the envelope also becomes broader as the xenon pressure is increased, enabling convenient experimental access to the 144 nm to 147 nm wavelength range.

4.6 Laser-Induced Plasma

The light sources introduced so far are narrowband light sources, making them excellent tools for the investigation of emission and excitation spectra. However, for the investigation of absorption spectra, a broadband light source is more suitable, as it allows to probe absorption profiles over extended wavelength ranges at once (assuming an appropriate detection unit to be available). Here, a laser-induced plasma (LIP) is used for this purpose. Generally, LIP is an umbrella term for the radiation emitted by a medium, a significant share of whose constituent particles has previously been ionized or vaporized by irradiation of an intense laser beam. It has been achieved in solid, liquid and gaseous materials, each of which exhibit characteristic advantages and disadvantages [129]. Whereas plasma generation in solid targets excels with regard to emitter density and hence emission intensity, it usually entails the creation of debris, curtailing its practical applicability. Gaseous targets show lower overall conversion efficiencies, but provide a very clean and experimentally controllable environment.

For the absorption measurements presented throughout this thesis, a LIP based on a noble gas target (argon, krypton or xenon) confined to a CF16-crosspiece is used, in the following referred to as *plasma cell* (Fig. 4.9). Along one axis, the plasma cell is equipped with two opposing borosilicate windows (*Vacom* VPCF16B-L) with a transmission range from 400 nm to 2500 nm. Along the second axis, one opening is used for the connection to the gas piping system; the opposing opening is equipped with a MgF_2-window. The LIP is excited with part of the laser radiation from the Q-switched nanosecond laser (Sec. 4.4). The copropagating second harmonic beam at 532 nm wavelength and the fundamental beam at 1064 nm wavelength exhibit an aggregate beam energy of around 300 mJ. Using a lens with a focal length of $f = 100\,\mathrm{mm}$ and an anti-reflection coating for 532 nm and 1064 nm wavelength, the compound beam with a diameter of 10 mm is focused through one of the borosilicate windows into the center of the plasma cell, where a spot size in the order of $2w_0 = 10\,\mu\mathrm{m}$ is reached, resulting in peak intensities as high as $4 \times 10^{17}\,\mathrm{W\,m^{-2}}$, exceeding the plasma ignition threshold. Part of the isotropic plasma light generated in the focal region is collected through the lateral MgF_2-window. The residual excitation light at 532 nm and 1064 nm wavelength leaves the plasma cell through the second borosilicate window and is then guided into a beam trap.

One of the advantages of the LIP is that its emission region is nearly pointlike, enabling an experimentally convenient collimation of the initially divergent light beam. For this, concave mirrors are used, as these are not subject to the strong chromatic dispersion of lenses in the VUV spectral regime[3]. Once collimated, the light can be guided to an absorption setup. Another advantage of the LIP, as used here, is the pulsed nature of its excitation, causing the emission from the LIP not to be temporally continuous, but to be confined to pulses. This is illustrated in Fig. 4.10(a), showing the spectrally-integrated plasma signal recorded with a photomultiplier

[3] Due to the lack of a material compensating for the dispersion of MgF_2 while simultaneously offering its unrivaled transmissivity, no achromatic lenses are available in the VUV spectral regime. While the chromatic dispersion of available lenses proves beneficial for the separation of the THG light and fundamental light, as explained in Sec. 4.5, it generally constitutes an inconvenience for experiments in this wavelength range.

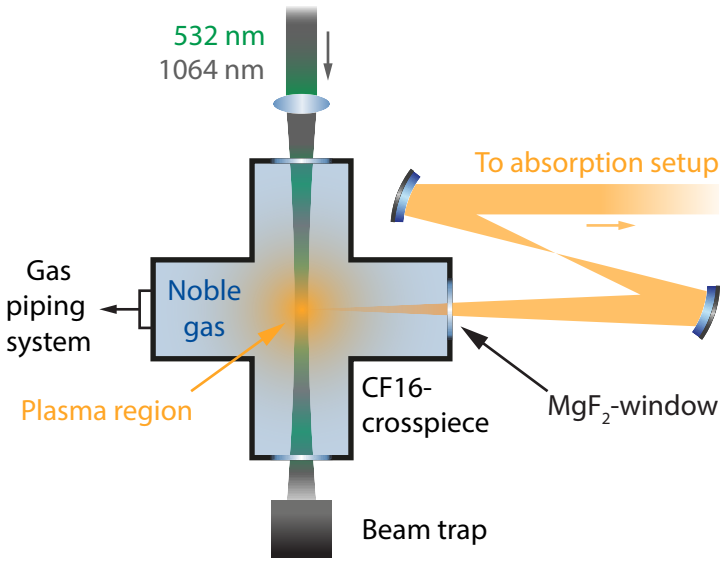

Figure 4.9: Sketch of the experimental setup for the generation of a laser-induced plasma (LIP). Centerpiece is a CF16-crosspiece filled with a noble gas (e.g. argon) and equipped with lateral viewports. Along the vertical axis, the superimposed beams at 532 nm and 1064 nm wavelength are guided through the plasma cell and focused into its center. Part of the light generated in this plasma region is collected through a lateral MgF_2-window on the horizontal axis, collimated using concave mirrors and guided to the absorption setup (not shown). Utilizing two mirrors for the collimation is necessary to ensure near-normal light incidence on both mirrors, preventing aberrations from different focal lengths in the vertical and horizontal plane of the spherically concave mirrors.

(*Hamamatsu* R10825). Although the temporal FWHM of the pulse corresponds to only 70 ns, there is a measurable contribution to the emission signal even multiple hundred nanoseconds after the plasma onset. For the investigation of noncontinuous effects, such as the nondegenerate two-photon absorption presented in Sec. 5.2, this is highly beneficial, as the available light is temporally confined, facilitating a higher instantaneous signal during the detection window. Figure 4.10(b) shows emission spectra of an argon plasma, recorded with an ICCD camera-based spectrometer (whose working principle will be illuminated in Sec. 4.7). The different spectra correspond to different gate width settings of the ICCD camera (the gate delay was kept constant), with larger gate widths indicated by a more opaque coloring of the corresponding spectra. A broad continuum, visible for very short gate widths, gradually evolves into a spectrum with distinct features as the gate width is increased. These pronounced spectral features are attributed to the recombination lines of ionized argon atoms [130–132]. Figure 4.10(c) shows the relation between the argon pressure in the plasma cell and the spectrally-integrated plasma strength. After an initial linear increase of the signal, for pressures above 700 mbar the signal saturates and above 1200 mbar, no increase of the signal can be observed (the maximum investigated pressure of 1500 mbar reflects the damage threshold of the plasma cell). Figure 4.10(d) shows normalized emission spectra of argon, krypton and xenon-based plasmas, respectively. Generally, the observed signal strength increases from argon over krypton to xenon, understood from the decreasing ionization energy with increasing noble gas mass [86]. For the measurements presented

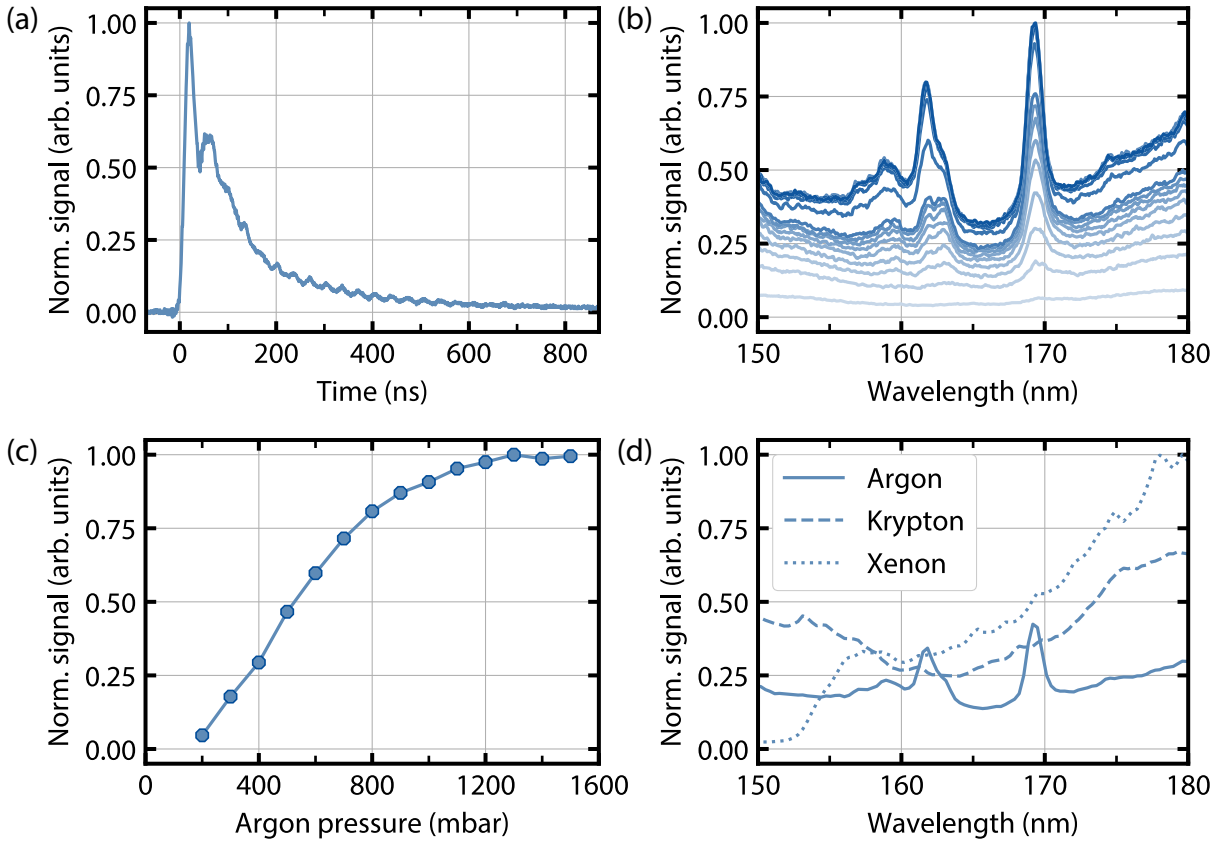

Figure 4.10: Characterizing measurements of the laser-induced plasma (LIP) – **(a)** Temporal evolution of the spectrally integrated plasma emission signal generated in argon (recorded with a photomultiplier). Although the temporal FWHM corresponds to only around 70 ns, there is still a significant contribution to the plasma pulse multiple hundred nanoseconds after its onset. **(b)** Normalized emission spectrum of an argon plasma, recorded with an ICCD camera-based spectrometer for different gate width settings between 20 ns and 1000 ns (and the gate delay kept constant). Spectra recorded with a larger gate width setting are indicated by a more opaque coloring. **(c)** Relation between the argon pressure in the plasma cell and the spectrally-integrated plasma emission strength, with the ICCD camera set to the maximum gate width probed in (b). **(d)** Normalized emission spectra of argon, krypton and xenon plasmas, each recorded at a gas pressure of 1 bar and with the ICCD camera set to the maximum gate width probed in (b). On the short-wavelength side, the spectrum of the xenon plasma is capped by the (atomic) absorption around 146.9 nm.

in this thesis, either argon or krypton are used as plasma target, as the emission spectrum of the xenon plasma on the short-wavelength side is curtailed by reabsorption on its own $5p^6 \rightarrow 5p^5 6s$ transition within the plasma cell.

4.7 Detection Units

For the recording of VUV spectra, two different detection units are used, each comprising a spectrograph and a camera; a schematic is shown in Fig. 4.11. The combined assembly of both devices is in the following referred to as *spectrometer*. Both spectrographs (*McPherson* model

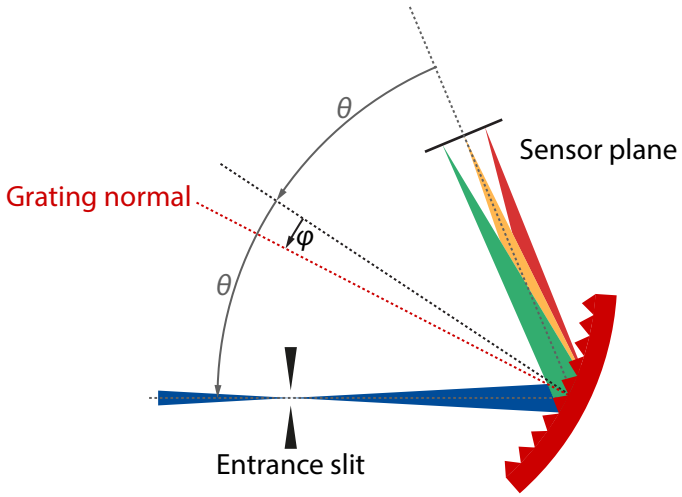

Figure 4.11: Working principle of a VUV spectrometer as used for the experiments presented in this thesis. Light to be investigated (blue) is focused onto an entrance slit and impinges onto a concave diffraction grating, where it is spectrally decomposed. At the same time, the grating images the entrance slit into the sensor plane, where the sensor chip of a CCD or ICCD camera is located. The deviation angle 2θ between the incidence and the diffraction direction of the spectrometer is fixed. The scan angle φ determines the central wavelength of the spectral range imaged into the sensor plane.

234 or *H+P spectroscopy* easyLight) are similar in their underlying design, consisting only of an entrance slit, its width adjustable between a few micrometers and several millimeters, and a diffraction grating. While the former creates a point-like light source, the concave grating both diffracts and images the light onto the exit plane of the spectrograph, where the camera sensor is located. By rotating the grating by the angle φ with an electric actuator, the spectral range imaged onto the camera sensor can be varied. The center wavelength λ of this spectral range is given by the grating equation [133],

$$Gm\lambda = 2\cos(\theta)\sin(\varphi) \ . \tag{4.5}$$

Here, m is the diffraction order, G is the grating constant and θ is the (half) deviation angle. The scan angle φ is measured from the bisector of the incidence and diffraction arms to the grating normal. For the available spectrometers, usually only the first diffraction order is used ($m = 1$), and the deviation angle is given by the spectrograph geometry ($\theta = 32°$). The grating constant, $G = 1200\,\mathrm{mm}^{-1}$ (easyLight) or $G = 2400\,\mathrm{mm}^{-1}$ (model 234), is critical for the spectral resolution of the spectrograph. It is around 0.1 nm or 0.05 nm for the respective device, assuming the entrance slit to be set to a width of 10 µm. With increasing slit width, the resolution decreases, which experimentally leads to a tradeoff between spectral resolution and light throughput.

For the actual detection of VUV radiation either an ordinary charge-coupled device camera

(CCD; *Andor* iDus 420) or an intensified CCD camera (ICCD; *Andor* iStar 320T) is used. The CCD camera has a MgF_2-entrance window and its sensor exhibits 1024 × 256 pixels with a pixel size of 26 µm × 26 µm. Its quantum efficiency (electron counts per incoming photon) is around 20 %. To record spectra, the camera is operated in the full-vertical-binning mode (FVB), describing the on-chip column-wise integration of pixel charges before readout. Determined by the grating dispersion and the sensor area, a wavelength range of about 45 nm can be imaged in a single exposure (without rotation of the grating). The ICCD camera, in contrast to the CCD camera, additionally incorporates an image intensifier unit. This consists of a photocathode, from which incoming photons release electrons, which are subsequently drawn to and through a multi-channel plate (MCP). In essence, this is an array of micrometer-thin tubes along whose length a variable voltage is applied, amplifying the electron signal in an avalanche process. Beyond the MCP a phosphor screen is located, converting the electron signal back to an optical signal, which can be detected with a conventional CCD sensor. The image intensifier unit brings about two key advantages over the use of a conventional stand-alone CCD camera: on the one hand, it facilitates rapid optical gating with temporal gate widths as short as 2 ns by switching the voltage across the MCP, bringing within reach the exploration of phenomena on similar timescales as the length of the pulses generated by the laser and OPO system used here. On the other hand, its adjustable gain enables signal amplifications as high as 10^3 compared to a nonintensified CCD camera, beneficial for measurements with low signal levels (despite its moderate quantum efficiency of about 11 % in the VUV spectral range). In the case of the ICCD camera-based spectrometer, the diameter of the image intensifier unit (18 mm) governs the light-sensitive area, allowing to image a spectral range of around 40 nm in a single exposure.

5 Two-Photon Excitation and Absorption Spectroscopy of Homonuclear Xenon

Whereas the investigations of the spectral emission profiles carried out in earlier work [46] were conducted using fixed-wavelength excitation schemes, for the present work an OPO system was available. As illustrated in Sec. 4.4, this light source provides tunable radiation throughout the wavelength range between 200 nm and 300 nm, which brings a (resonant) driving of xenon's allowed two-photon transitions from the ground state within reach. Hence, with the aim of identifying suitable pump mechanisms for future microcavity-based experiments, two-photon excitation spectroscopy of xenon at elevated pressures was conducted, i.e. a systematic determination of the excitation wavelengths resulting in the highest fluorescence response. Corresponding results will be presented in Sec. 5.1. In the following, the terms *fluorescence* and *emission* will at times be used interchangeably, as is common practice in scientific literature.

Another finding from [46] was an insufficient probability for photons emitted by xenon dimers to be reabsorbed within the same sample, preventing an adequate number of absorption and reemission cycles of photons in future microcavity-based experiments for a thermalization of the photon gas. This shortcoming of the pure-xenon system is rooted in the large spectral gap between the (atomic) absorption and the emission on the second excimer continuum or, put differently, in the large binding energy of xenon excimers. In Sec. 5.2, an approach to compensate this spectral gap will be illustrated, based on the provision of an auxiliary photon field and the inclusion of higher-lying excimer states into the cycles of absorption and reemission.

5.1 Excitation Spectroscopy

Two-photon excitation is a widely used tool, as it generally allows the exciting radiation to be of longer wavelength than the emitted radiation. Xenon exhibits a number of electronic states that can be excited from the $5p^6$ ground state by allowed two-photon transitions[1], namely those of the $5p^5 6p$ and $5p^5 6p'$ configurations exhibiting even total angular momentum ($J = 0,\ 2$), as illustrated in Fig. 5.1. Specifically, these are the $5p^5 6p[1/2]_0$ state at a wave number of $80\,119.0\,\mathrm{cm}^{-1}$, the $5p^5 6p[3/2]_2$ state at $79\,212.5\,\mathrm{cm}^{-1}$ and the $5p^5 6p[5/2]_2$ state at $78\,119.8\,\mathrm{cm}^{-1}$ [86]. In a two-photon excitation scheme, these transition energies correspond to single-photon wavelengths of 249.6 nm, 252.5 nm and 256.0 nm, respectively. The $5p^5 6p'$ configuration, mean-

[1] These need to fulfill $|J_i - J_f| \leq 2$, with $J_{i,f}$ the total angular momenta of the initial (i) and final (f) states, respectively. In the case of two equal-wavelength photons, the transitions $J_i = 0 \rightarrow J_f = 1$ and $J_i = 1 \rightarrow J_f = 0$ are forbidden due to destructive interference between different excitation paths [134, 135]. Further, parity conservation needs to be observed, $P_i \cdot P_f = 1$, with $P_{i,j}$ the parities of the initial and the final state.

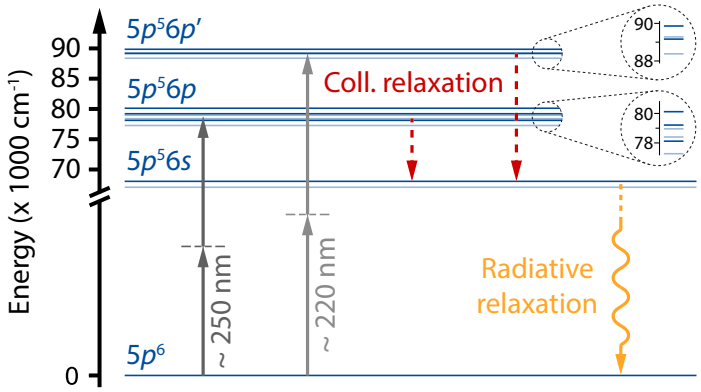

Figure 5.1: Energy levels of xenon as relevant for the measurements in this section. States of the $5p^5 6p$ and $5p^5 6p'$ configurations involved in the allowed two-photon transitions investigated here are indicated in dark blue, other states of the respective configurations are indicated in light blue (also note the magnified visualization in the dashed areas). Excitation to these states is realized by irradiation of UV light around 220 nm or 250 nm wavelength, respectively. After collisional relaxation to the $5p^5 6s$ state (see text), relaxation to the $5p^6$ ground state occurs radiatively with emission on the second excimer continuum (in dense samples as considered here).

while, exhibits two such states, the $5p^5 6p'[1/2]_0$ state at a wave number of 89 860.0 cm^{-1} and the $5p^5 6p'[3/2]_2$ state at 89 162.4 cm^{-1}, corresponding to single-photon wavelengths of 222.6 nm and 224.3 nm.

After excitation to the $5p^5 6p$ or $5p^5 6p'$ configurations, excimers relaxate to the $5p^5 6s$ configuration either radiatively, via emission of a near-infrared photon, or nonradiatively, via collisions with surrounding atoms. For the $5p^5 6p$ configuration, reported collisional deactivation rates are $(6 - 120) \times 10^{-12} \mathrm{cm}^3/\mathrm{s}$ [136], depending on the particular state of this configuration. Even at the comparatively low pressure of 10 bar, this corresponds to a quench rate of $(1.5 - 30.3)\ \mathrm{ns}^{-1}$. This clearly exceeds the spontaneous emission rate, as radiative lifetimes of the $5p^5 6p \rightarrow 5p^5 6s$ transition are (27 – 36) ns. Collisional deactivation rates for the $5p^5 6p'$ configuration are even higher, $(423 - 426) \times 10^{-12} \mathrm{cm}^3/\mathrm{s}$. Accordingly, for both configurations the relaxation to the $5p^5 6s$ configuration is assumed to be dominated by collisional, nonradiative deactivation.

5.1.1 Setup and Characterization

The setup used for the two-photon excitation spectroscopy is shown in Fig. 5.2. UV light near 220 nm or 250 nm wavelength generated in the OPO system is guided to the vacuum chamber. A mirror placed on a motorized flip mount (*Thorlabs* MFF101) allows to direct the beam onto the measurement head of an energy meter (*Coherent* FieldMax II; sensor J-25MB-LE). The beam enters the vacuum chamber through an uncoated UV fused-silica window (*Thorlabs* WG41050). Part of the light scattered off this window is collected with a fiber coupler and guided to a CCD spectrometer (*Thorlabs* CCS200), enabling a tracking of the wavelength of the excitation light. Inside the vacuum chamber, the excitation beam is guided to the five-window high-pressure cell introduced in Sec. 4.2.1 using UV-enhanced aluminum mirrors (*Thorlabs* PF10-03-F01) and

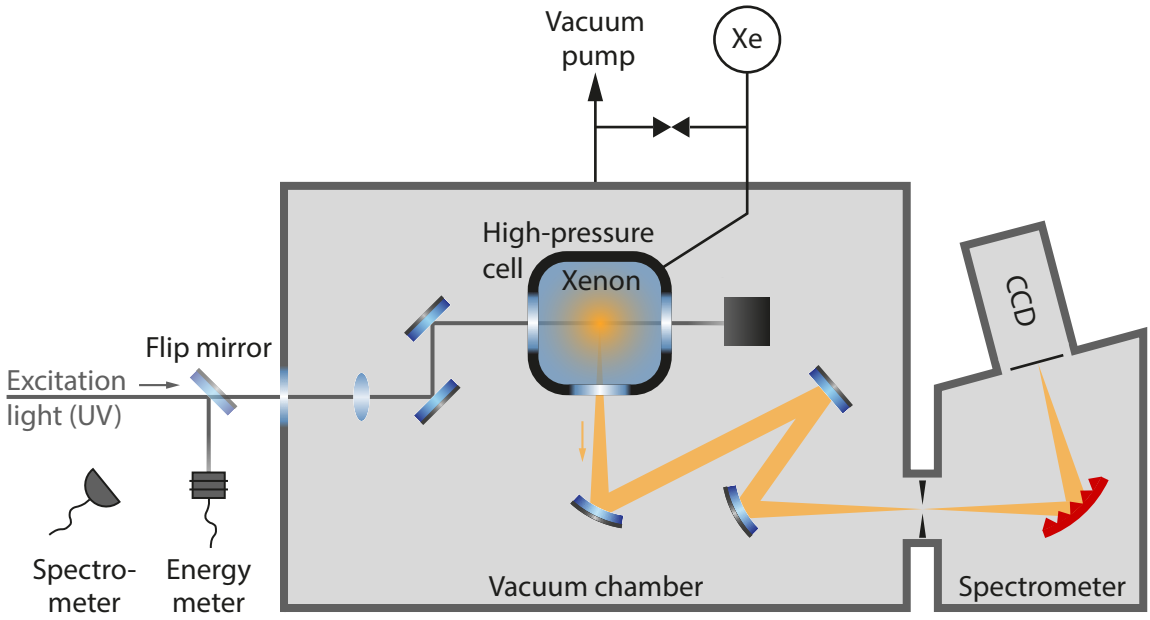

Figure 5.2: Setup for the investigation of two-photon excitation spectra. UV excitation light around either 220 nm or 250 nm wavelength generated by the OPO system is guided into the vacuum chamber. A fiber-coupled spectrometer and an energy meter allow to track the current excitation wavelength and the pulse energy. Fluorescence light is collected under an angle of 90° relative to the direction of the excitation beam and guided into the CCD camera-based spectrometer for analysis.

focused into its center with a plano-convex lens of 25 cm focal length (*Thorlabs* LA4158). At the center of the cell, the excitation beam exhibits a calculated $1/e^2$-diameter of around 10 µm. Beyond the cell, the beam is guided into a beam trap. Part of the radiation generated in xenon samples (prepared using the gas piping system illustrated in Sec. 4.3.1) by the excitation beam is collected through one of the lateral cell windows by a concave mirror (*Laseroptik* coating B-02250-01). It is situated such that its focal length $f = R/2$, with $R = -200$ mm its radius of curvature, matches its distance from the center of the high-pressure cell, resulting in a collimated beam of fluorescence light. Using another concave mirror with $R = -400$ mm, this beam is focused onto the entry slit of the CCD camera-based spectrometer introduced in Sec. 4.7. For all measurements, the entry slit was set to a width of 10 µm. All relevant mirrors are situated in piezo-actuated mirror mounts, allowing for an optimization of the incoupling of the excitation light into the cell and of the emission light into the spectrometer.

Intrinsically, the output energies of the OPO system in the UV wavelength regions probed here are strongly wavelength-dependent. Moreover, the pulse energies are in the order of 20 mJ; such energies would lead to an excessive energy density on the windows of the high-pressure cell, which are only 1 cm away from the focal point of the excitation beam. This makes a deliberate reduction of the pulse energy necessary, achievable by adjusting the UV-S and UV-L crystals involved in the generation of UV radiation (Sec. 4.4). Using a custom calibration between target wavelength and crystal angle, it is possible to achieve a much flatter energy curve over the desired

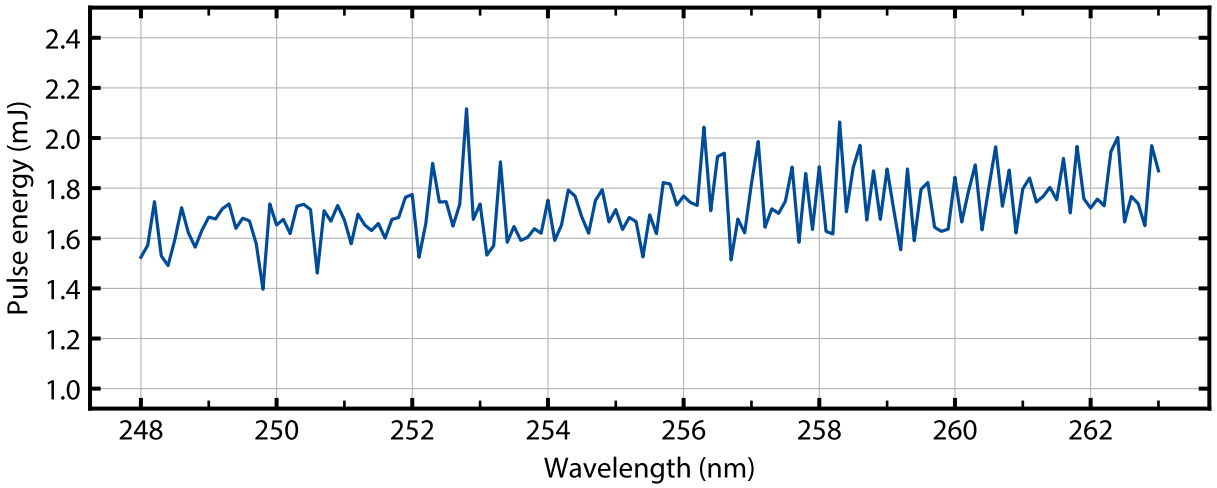

Figure 5.3: Relation between wavelength and pulse energy of the OPO system in the spectral range covering the $5p^6 \rightarrow 5p^5 6p$ two-photon transitions. The data was obtained after conducting a custom angle calibration of the UV-generating crystals in the OPO system. The observed wavelength-to-wavelength variations are persistent over multiple measurement iterations and can be attributed to slight inaccuracies in the crystals' angle control.

wavelength range. Exemplarily, Fig. 5.3 shows the resulting dependency between wavelength and pulse energy in the spectral range around the xenon $5p^6 \rightarrow 5p^5 6p$ two-photon transitions. The pulse energies are now mostly below 2 mJ, experimentally proven to be innocuous for the cell windows over extended periods of time.

A residual wavelength-dependency can be observed in Fig. 5.3, necessitating a tracking of the pulse energy at every excitation wavelength to allow for a correction for different pulse energies. A quadratic scaling between pulse energy and fluorescence signal, as expected for the two-photon excitation scheme considered here [137], has been experimentally validated. Figure 5.4(a) exemplarily shows the fluorescence yield[2] of a xenon sample at a pressure of 20 bar as a function of the squared pulse energy at a fixed excitation wavelength of 256.5 nm. The data can well be described by a linear function, warranting the application of a quadratic relation between pulse energy and fluorescence yield. Figure 5.4(b) shows emission spectra of a xenon sample at a pressure of 20 bar, under excitation with light of different wavelengths. Within experimental accuracy, the spectra agree with each other, fulfilling Kasha's rule (Sec. 2.2.1) and suggesting a thermally equilibrated level occupation within the quasimolecular manifold in the bound part of the excimer potential energy curve. With their maxima at wavelengths around 172 nm and a FWHM of about 13 nm, the spectra can be identified as the second excimer continuum emission of xenon, expected for samples at pressures above a few hundred millibars (Sec. 3.3).

[2] Here and in the following, the term *fluorescence yield* refers to the spectral integral of the emission spectrum. This value as such represents no physical quantity in a narrow sense, since it is governed by a number of experimentally inaccessible parameters, such as the solid angle spanned by the lateral cell window through which the fluorescence is detected, the transmission through the spectrometer's entry slit and the quantum efficiency of the CCD camera. As, however, the aim of the measurements presented in this section is the identification of the most efficient excitation wavelength, this fact is of minor relevance.

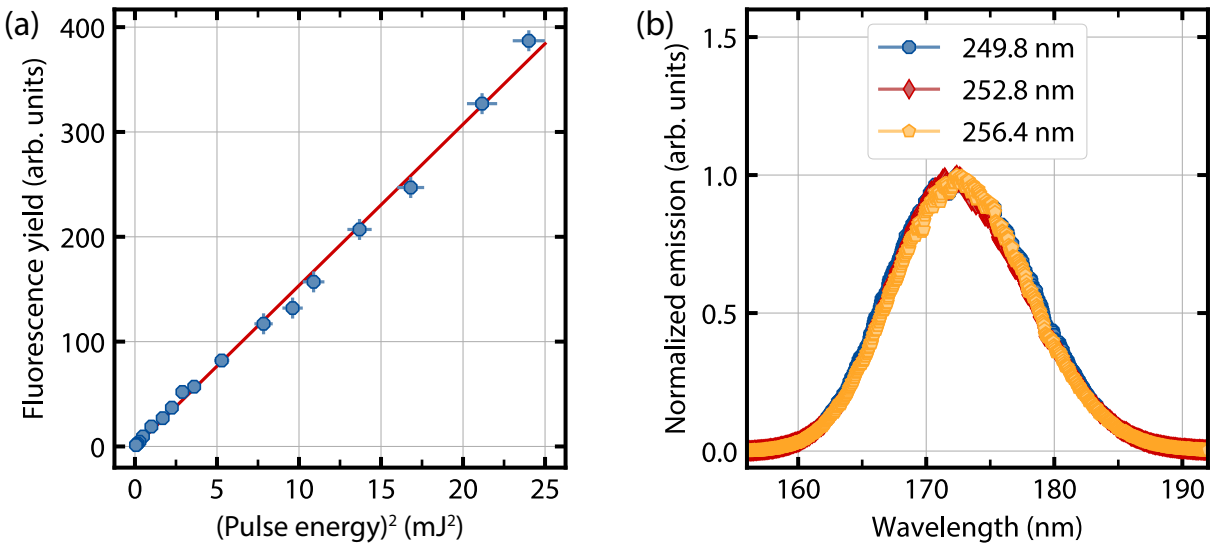

Figure 5.4: Characterizing measurements of the two-photon excitation – **(a)** Dependence between squared pulse energy and fluorescence yield in a xenon sample at a pressure of 20 bar under excitation with light at a fixed wavelength of 256.5 nm (blue data points). The error bars are dominated by the shot-to-shot pulse energy fluctuations of the OPO system. The agreement with a linear function (red) validates the quadratic energy scaling expected for a two-photon excitation. **(b)** Normalized emission spectra of a xenon sample at a pressure of 20 bar under excitation with light of different wavelengths. The observed independence of the spectral shape on the excitation wavelength validates the applicability of Kasha's rule in this system.

5.1.2 Methods and Results

The excitation spectra presented in the following are recorded in a wavelength scan covering the $5p^6 \rightarrow 5p^5 6p$ and $5p^6 \rightarrow 5p^5 6p'$ two-photon resonances. Each scan was conducted using the following repetitive experimental steps:

- The OPO system is set to a new target wavelength, for example 250.0 nm.
- The mirror on the motorized flip mount is brought into the beam path and the pulse energy is measured.
- The mirror on the motorized flip mount is removed from the beam path and the excitation beam then reaches the xenon sample. The ensuing fluorescence light is recorded with the spectrometer.
- The fiber-coupled spectrometer tracks the current excitation wavelength.

During the scan, the spectrometer is set to a center wavelength of 175 nm, allowing to record the emission on the second excimer continuum in its entirety. The CCD camera, whose sensor chip is cooled down to a temperature of −50 °C, is set to an exposure time of 0.55 s, covering five successive shots from the OPO system. Averaging ten consecutive spectra at every excitation wavelength leads to a total average over 50 pulses, suppressing statistical fluctuations sufficiently.

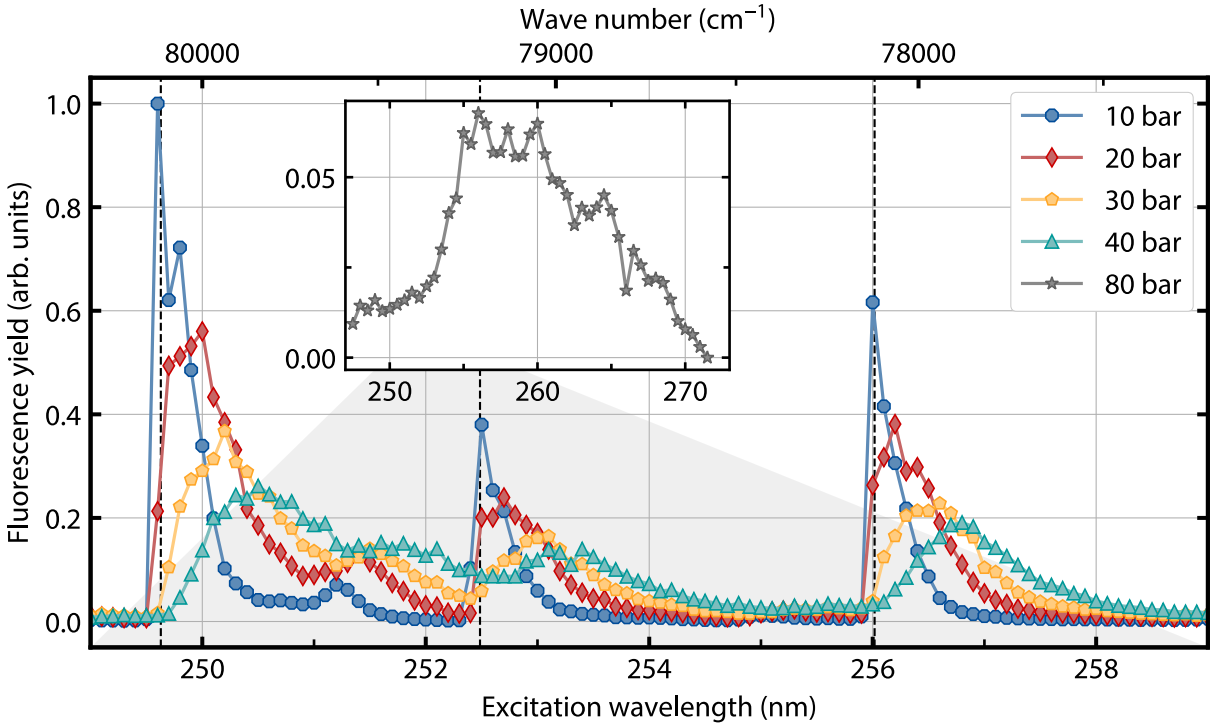

Figure 5.5: Excitation spectra of the xenon $5p^6 \rightarrow 5p^5 6p$ two-photon transitions for different sample pressures, both in the gaseous and supercritical regimes. The vertical dashed lines (from left to right) represent the spectral positions of the undisturbed $5p^6 \rightarrow 5p^5 6p[1/2]_0$, $5p^5 6p[3/2]_2$ and $5p^5 6p[5/2]_2$ transitions [86]. The inset depicts an excitation spectrum of a sample at a pressure of 80 bar, i.e. in the supercritical regime (note the different horizontal and vertical range covered by the inset as compared to the main plot).

Figure 5.5 shows excitation spectra of the $5p^6 \rightarrow 5p^5 6p$ transitions in xenon for various pressures in the gaseous phase (10 bar to 40 bar) and in the supercritical regime (80 bar). In the data set for the sample at the lowest pressure, 10 bar, three distinct peaks can be observed, which can be identified with the $5p^6 \rightarrow 5p^5 6p[1/2]_0$, $5p^5 6p[3/2]_2$ and $5p^5 6p[5/2]_2$ transitions (whose undisturbed transition energies correspond to wave numbers of 80 119.0 cm^{-1}, 79 212.5 cm^{-1} and 78 119.8 cm^{-1}, respectively). For each of these three major resonance features, a strong asymmetry is evident, with their blue (short-wavelength) edges being very steep and their red (long-wavelength) edges petering out more slowly. Such pronouncedly asymmetric line shapes of the $5p^6 \rightarrow 5p^5 6p$ transitions have been reported in earlier work [93, 94] and are attributed to the downward-bending potential energy curves of the states within the $5p^5 6p$ configuration (see also Fig. 3.3). At a wavelength of around 251.2 nm, another feature can be observed in the excitation spectrum. The only transition this could be attributed to is the $5p^6 \rightarrow 5p^5 5d\,[1/2]_0$ transition, expected at 79 771.3 cm^{-1} (250.7 nm), as this is the only state with an energy between the two higher-energy $5p^5 6p$ states accessible from the ground state in allowed two-photon transitions. This $5p^6 \rightarrow 5p^5 5d$ transition is forbidden (violating parity conservation in a two-photon process), but its presence has been observed in previous two-photon spectroscopic studies and was ascribed to a pressure-induced transition [94, 138].

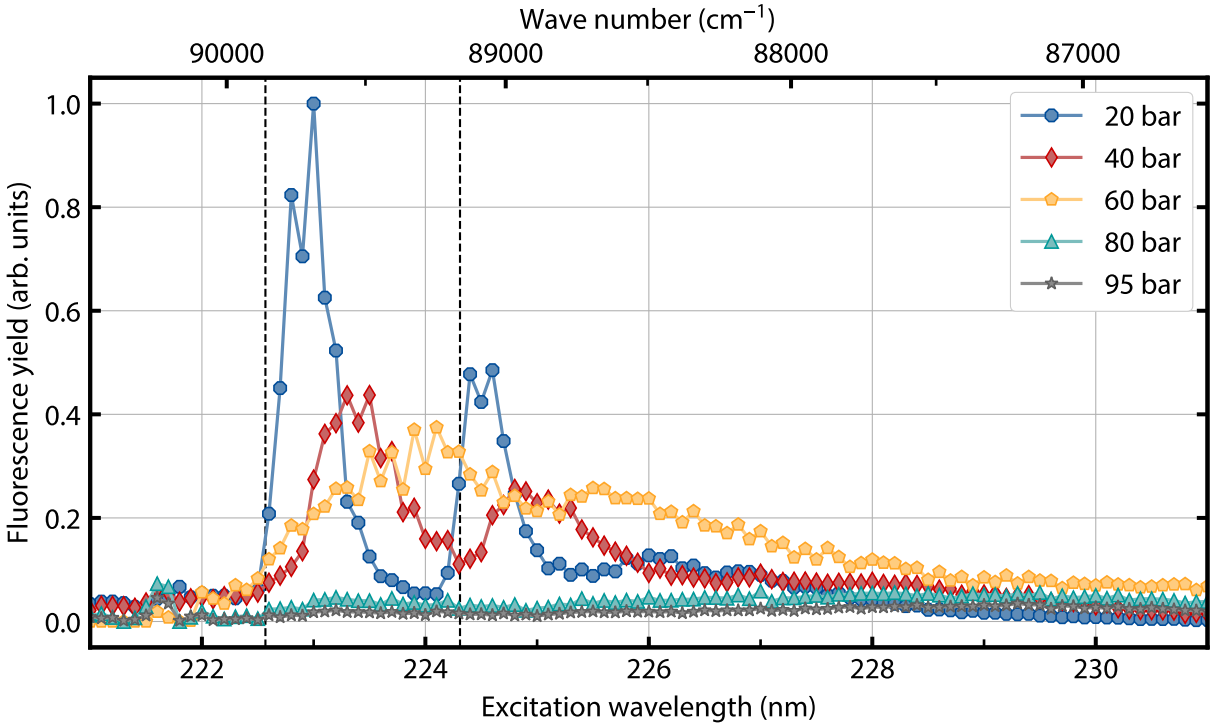

Figure 5.6: Excitation spectra of the higher-energetic xenon $5p^6 \rightarrow 5p^5 6p'$ two-photon transitions for different sample pressures, both in the gaseous and supercritical regimes. The vertical dashed lines (from left to right) represent the spectral positions of the undisturbed $5p^6 \rightarrow 5p^5 6p'[1/2]_0$ and $5p^5 6p'[3/2]_2$ transitions [86].

Upon increasing the xenon pressure, the three major features in the excitation spectrum exhibit a significant spectral broadening and also their respective center positions shift toward lower energies, by rates of $(9.3 \pm 1.4)\,\mathrm{cm}^{-1}/\mathrm{bar}$, $(8.3 \pm 1.2)\,\mathrm{cm}^{-1}/\mathrm{bar}$ and $(8.5 \pm 1.1)\,\mathrm{cm}^{-1}/\mathrm{bar}$, respectively. At the highest pressure in the gaseous phase investigated here, 40 bar, the two higher-energy $5p^6 \rightarrow 5p^5 6p$ resonances along with the putative $5p^6 \rightarrow 5p^5 5d$ resonance form a continuum extending over a wide range of more than 4 nm, corresponding to an energy-equivalent of around $3\,k_\mathrm{B}T$ in this wavelength range. The inset in Fig. 5.5 (note the different horizontal and vertical extent) shows the fluorescence yield for a sample at a pressure of 80 bar. This corresponds to conditions well within the supercritical regime, which is reached upon transcending the critical pressure of 58.4 bar at room temperature. The magnitude of the spectral broadening renders the individual spectral components of the $5p^6 \rightarrow 5p^5 6p$ two-photon transitions unresolvable, as has already been foreshadowed by the extent of the spectral broadening for the highest pressures in the gaseous phase.

In Fig. 5.6 excitation spectra of the $5p^6 \rightarrow 5p^5 6p'$ transitions are shown for different xenon pressures between 20 bar and 95 bar, i.e. for samples both in the gaseous and the supercritical regimes. At the lowest investigated pressure, 20 bar, two distinct spectral features can be observed experimentally, which can well be attributed to the allowed $5p^6 \rightarrow 5p^5 6p'[1/2]_0$ and $5p^5 6p'[3/2]_2$ two-photon transitions (with undisturbed spectral positions at wave numbers of

89 860.0 cm^{-1} and 89 162.4 cm^{-1}, respectively). Interestingly, the asymmetry of the spectral features here is not as pronounced as in the excitation spectrum for the $5p^6 \rightarrow 5p^5 6p$ transitions at the same pressure, indicating less strongly downward-bent potential energy curves. Upon increasing the pressure, a pressure shift as well as a broadening are visible and similar to the case of the $5p^6 \rightarrow 5p^5 6p$ transitions above, no distinct spectral features are resolvable.

The measurements in this section clearly show that an excitation of xenon samples via two-photon processes is possible, with the investigated pressure ranges significantly expanding the available literature. The results indicate possible pumping schemes for future microcavity-based experiments on Bose-Einstein condensation of VUV photons. With an excitation of dense xenon samples possible in the UV over wide wavelength ranges (corresponding to multiple thermal energy units $k_\mathrm{B}T$), the convenient experimental creation of a photon gas inside a microcavity appears possible. Contemplating pump sources beyond the tunable OPO system available here, an excitation could be based, for example, on radiation around 253 nm, obtainable via fourth-harmonic generation of radiation from infrared laser sources [139]. Samples in the supercritical regime could be excited with radiation near 266 nm, as provided by widely available frequency-quadrupled Nd:YAG lasers.

5.2 Absorption Spectroscopy

The measurements described in the last section have shown that the states with even total angular momentum of the $5p^5 6p$ configuration can be accessed from the $5p^6$ ground state in two-photon transitions. So far, in this *degenerate* excitation scheme two photons of equal wavelength were involved. It is tempting to ask whether these can also be accessed by transitions involving two photons of unequal wavelengths, i.e. in a *nondegenerate* excitation scheme [140]. This could prove helpful for increasing the low reabsorption probability of photons emitted on the strongly Stokes-shifted second excimer continuum of xenon, which currently constitutes a major obstacle for the overarching aim of this experiment – to achieve thermalization and ultimately Bose-Einstein condensation of photons in the VUV spectral regime. The energy difference between a 172 nm-wavelength-photon and the $5p^5 6p$ configuration amounts to a photon wave number of around 20 000 cm^{-1}, depending on the respective state. This corresponds to a wavelength in the blue-to-green spectral range, well within the tuning range of the OPO system presented in Sec. 4.4. By providing an auxiliary light field of photons with suitable wavelength, photons on the second excimer continuum around 172 nm wavelength could be included in reabsorption processes by xenon dimers, as illustrated in Fig. 5.7. In this way, inducing absorption beyond that reached for radiation around 172 nm on the single-photon $5p^6 \rightarrow 5p^5 6s$ transition, in future microcavity-based experiments photons could be prevented from leaving the microcavity before undergoing a sufficient number of absorption and reemission cycles.

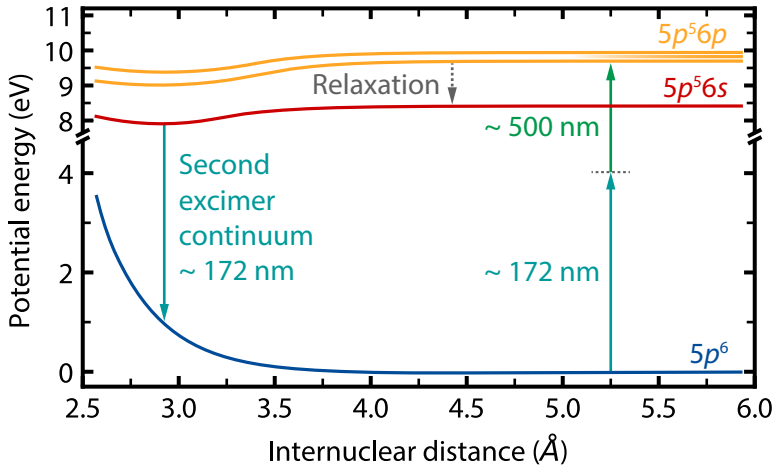

Figure 5.7: Simplified potential energy diagram of xenon, as relevant for the nondegenerate two-photon absorption (potential curves from Fig. 3.3). In the scheme, a VUV photon around 172 nm wavelength (its energy insufficient to drive the $5p^6 \rightarrow 5p^5 6s$ transition) is paired with an auxiliary photon in the blue-to-green spectral range around 500 nm to drive the $5p^6 \rightarrow 5p^5 6p$ two-photon transitions. Exploiting this expanded cycle (including intermediate relaxation from the $5p^5 6p$ to the $5p^5 6s$ configuration) in a future microcavity environment, the number of absorption and reemission events a photon undergoes before leaving the microcavity could be increased.

5.2.1 Setup

The setup used for the two-photon absorption measurements performed here is shown in Fig. 5.8. A laser-induced plasma (LIP, see Sec. 4.6) is used as a broadband light source, implemented by focusing light from the Nd:YAG pump laser and its second harmonic (at 1064 nm and 532 nm wavelength, respectively) into a cell filled with argon gas at around 1 bar pressure. After the light from the LIP is collected and collimated with a concave mirror (*Laseroptik* coating B-02250-01), it is guided through the five-window high-pressure cell (Sec. 4.2.1) with a window configuration resulting in an optical path length of 2 cm by a pair of dichroic mirrors (*Laseroptik* coating B-17281). Reaching a maximum reflectivity of 93 % around 165 nm wavelength with a reflectance bandwidth of around 20 nm, their transmissivity exceeds 90 % in the visible spectral range. Subsequently, the light passes through a VUV bandpass filter (*Acton Optics* 150-B-1D) with a maximum transmissivity of 32 % at 150 nm, a transmission bandwidth of around 50 nm and a rejection ratio of $1/1000$ for radiation in the visible spectral range. Eventually, the light is focused onto the entrance slit of the ICCD camera-based spectrometer. Using the dichroic mirrors' transmissivity for visible light, a beam coming from the OPO system in the 480 nm to 510 nm wavelength range is superimposed with the VUV beam passing through the cell. Both beams counterpropagate to reduce the amount of stray light recorded with the spectrometer. Spatial overlap of both beams is ensured by guiding them through two apertures, one on either side of the high-pressure cell, constraining them to a diameter of 5 mm. In conjunction with a pulse energy of 15 mJ and a pulse length of 8 ns, this corresponds to an intensity of 96 GW m^{-2} (average over one pulse). Before the beam from the OPO system enters the vacuum chamber, it passes a delay stage (not shown in Fig. 5.8) to ensure that its constituent pulses arrive at the

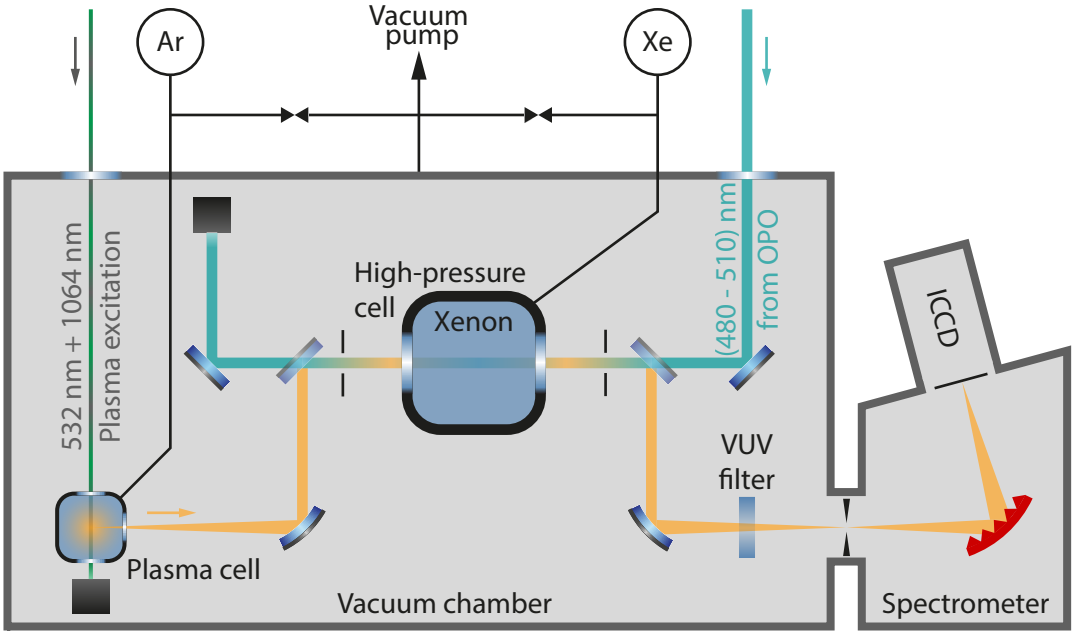

Figure 5.8: Setup for the investigation of nondegenerate two-photon absorption of xenon. Laser-light at 532 nm and 1064 nm from the Nd:YAG laser is used to generate a laser-induced plasma (LIP) in an argon environment. Its light is collimated and guided through a xenon-filled high-pressure cell, before entering the ICCD camera-based spectrometer. Using two dichroic mirrors, a beam coming from the OPO system in the 480 nm to 510 nm wavelength range is superimposed with the beam from the LIP at the position of the high-pressure cell. The two counterpropagating beams are constrained to a diameter of 5 mm by two apertures. The VUV filter prevents visible and infrared stray light from entering the spectrometer.

high-pressure spectroscopy cell simultaneously with the pulses from the LIP (temporal overlap), see Fig. 5.9. The combination of dichroic mirrors, VUV bandpass filter and counterpropagating beams facilitates the required strong suppression of visible and infrared stray radiation, while allowing to detect a sufficient amount of light in the wavelength range where VUV absorption induced in the two-photon processes investigated here is expected.

5.2.2 Methods and Results

For the measurements presented in the following, the spectrometer was set to a center wavelength of 170 nm, allowing to resolve the wavelength range in which absorption induced by the additional light field is expected. The sensor chip of the ICCD camera was cooled down to −25 °C and an exposure time of 20 ms was chosen. A total of 1800 consecutive single-shot frames were averaged to obtain a spectrum with sufficient suppression of signal fluctuations, as caused by pulse energy variations of both the OPO and the plasma light source. The gate width of the ICCD camera's image intensifier was set to equal the pulse length of the OPO source, 8 ns, and the gate delay was chosen such that the temporal center of the detection window coincides with the center of the OPO pulse.

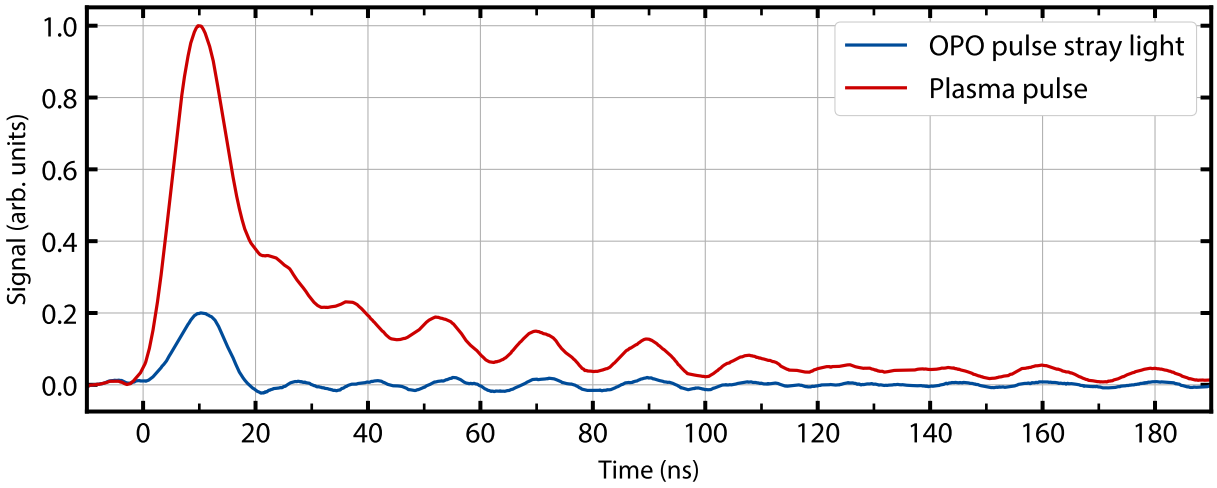

Figure 5.9: Temporal dependence of the emission of the OPO source and the emission of the laser-induced plasma. The data has been recorded using a photomultiplier-based spectrometer instead of the ICCD camera-based spectrometer shown in Fig. 5.8. For the detection of the plasma pulse, the spectrometer grating was set to a wavelength of 168 nm. For the detection of the OPO pulse, the spectrometer grating was set to the zeroth diffraction order, allowing to detect some of the stray light scattered off the windows of the high-pressure cell. The oscillations in the signal for times larger than 20 ns are caused by electromagnetic stray fields from the opening and closing of the Q-switch in the pump laser.

With a xenon sample at 35 bar pressure in the high-pressure cell and the OPO system tuned to a wavelength of 500 nm, two transmission spectra through the cell were recorded; one with the auxiliary OPO beam passing through the cell ($I(\lambda)_{\text{with OPO}}$) and one with the auxiliary OPO beam blocked ($I(\lambda)_{\text{without OPO}}$). Applying Beer's law,

$$\frac{I(\lambda)_{\text{with OPO}}}{I(\lambda)_{\text{without OPO}}} = \exp\left(-\alpha_{\text{VUV}}(\lambda)\, L\right) , \tag{5.1}$$

absorption spectra, denoted as $\alpha_{\text{VUV}}(\lambda)$, are calculated from these transmission spectra (with $L = 2\,\text{cm}$ the optical path length of the high-pressure cell). Typical results are shown in Fig. 5.10(a). Three absorption peaks around 167 nm, 170 nm and 173 nm wavelength are visible; these can be attributed to the $5p^6 \rightarrow 5p^5 6p[1/2]_0$, $5p^5 6p[3/2]_2$ and $5p^5 6p[5/2]_2$ two-photon transitions, similarly to the observations from Fig. 5.5. The spectral distance between the features visible under both the degenerate and the nondegenerate excitation is similar, with a wavenumber difference of about $2000\,\text{cm}^{-1}$ between the rightmost and the leftmost peak.

Inspecting the shape of the individual peaks more closely, one notices a slight asymmetry of the two higher-energy peaks. Their red edges drop off more slowly than their blue edges, which is in accordance with the results on the degenerate excitation of the states of the $5p^5 6p$ configuration. The remaining lowest-energy feature observable in Fig. 5.10(a), however, possesses a very symmetric form, with both its edges dropping off in an equal fashion. This is a difference to the degenerate case, where in Fig. 5.5 the three main resonance features show an equally asymmetric

shape among them. Further, in the degenerate case, the feature with the highest transition energy appears strongest (in Fig. 5.5 around 250.5 nm for the data set recorded at 40 bar), whereas in the nondegenerate case the lowest-energy feature appears most prominent.

Further evidence for the occurrence of a two-photon absorption process is obtained by tuning the wavelength setting of the OPO system and monitoring changes of the corresponding VUV absorption spectra, as an increase of the OPO photon wavelength should invariably lead to a shift of the VUV absorption spectrum to lower wavelengths, and vice versa. Figure 5.10(b) shows absorption spectra for four OPO wavelength settings between 480 nm and 510 nm. Indeed, changing the OPO photon wavelength (while keeping the pulse energy constant) results in collectively shifted absorption spectra. The shifts also agree quantitatively, as a wavelength difference of 10 nm around 500 nm corresponds to a wavelength difference of 1.2 nm around 170 nm. Figure 5.10(c), then, shows the same spectra visualized as a function of the wavenumber sum of the two light fields driving the two-photon transition, resulting in the four spectra lying on top of each other. Noticeably, varying the OPO photon wavelength leaves the absorption spectrum's shape unchanged, implying that the transitions do not depend on the ratio in which the two nondegenerate photons contribute their respective energy amounts. The structure of the absorption spectrum is rather governed by the shape of the potential energy curves of the quasimolecular states involved in the observed transitions [89].

Figure 5.10(c) additionally shows the *degenerate* two-photon excitation spectrum for the comparable gas pressure of 40 bar (data from Fig. 5.5). The data sets agree well with respect to their overall shape. The observed slightly larger linewidth in the absorption spectra is a consequence of the reduced wavelength resolution of the ICCD camera-based spectrometer used for the corresponding measurements, as compared to the CCD camera-based spectrometer. The relative heights of the three absorption peaks are roughly equal, whereas in the case of the degenerate excitation spectrum the feature associated with the $5p^6 \rightarrow 5p^5 6p[1/2]_0$ transition appears dominant. The weakly pronounced feature between 251 nm and 252 nm observed with the degenerate excitation scheme (Fig. 5.5), ascribed to the $5p^6 \rightarrow 5p^5 5d$ transition, appears not as pronounced in the nondegenerate absorption scheme. The minor disparities (different shapes and relative peak heights) between both schemes are presumably rooted in the different measurement approaches, as the excitation spectra (Fig. 5.5) not only account for the absorptive behavior of xenon dimers, but are also influenced by internal conversion processes occurring before radiative relaxation to the ground state.

Figure 5.11 shows absorption spectra obtained for different values of the gate delay of the image intensifier within the ICCD camera, with a fixed wavelength of the auxiliary light field, $\lambda_{\mathrm{aux}} = 490\,\mathrm{nm}$, and a fixed gate width of 8 ns. The absolute value of the gate delay is of no relevance here, as it is subject to an arbitrary offset in any case, among others governed by delays incurring in the circuitry of the ICCD camera. The absorption spectra contain statistically significant nonzero contributions only for gate delays of 15 ns and 20 ns, i.e. roughly within a 5 ns-wide window; agreeing with the temporal half-width of the OPO pulse within the temporal

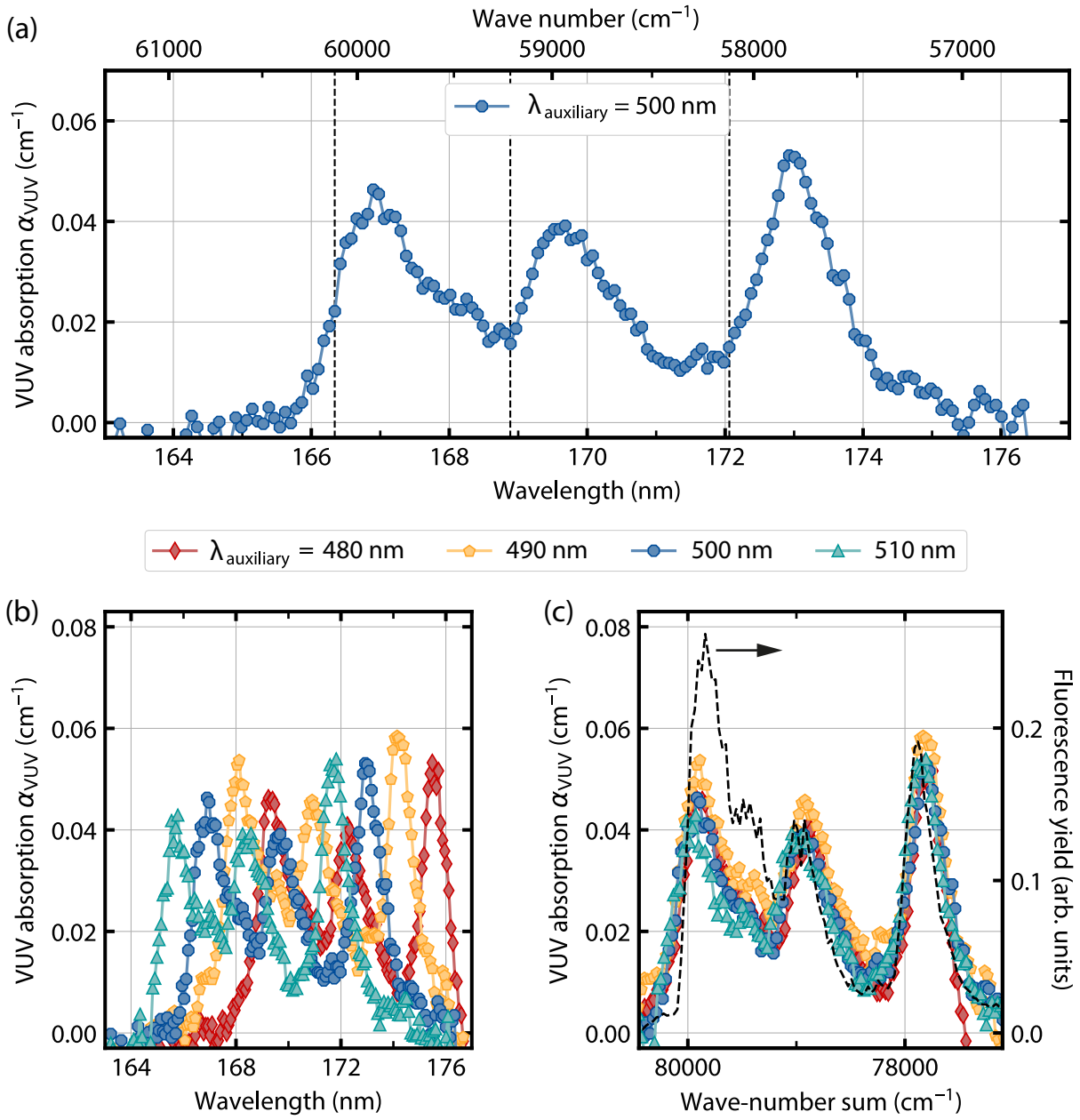

Figure 5.10: Spectra of the nondegenerate absorption on the xenon $5p^6 \rightarrow 5p^5 6p$ two-photon transitions – **(a)** Absorption in the spectral region near the second excimer continuum emission, in a sample at a pressure of 35 bar under irradiation of an auxiliary light field, here set to a wavelength of 500 nm. The three visible features can be attributed to the $5p^6 \rightarrow 5p^5 6p[1/2]_0$, $5p^5 6p[3/2]_2$ and $5p^5 6p[5/2]_2$ two-photon transitions (from left to right), whose undisturbed transition energies are indicated by the vertical dashed lines. **(b)** Data obtained from the same sample, with the auxiliary light field tuned to different wavelengths, which gives rise to a spectral shift between the individual absorption spectra. **(c)** The data from (b) plotted as a function of the wave-number sum of the two light fields involved in the nondegenerate driving of the transitions. As expected, in this visualization the four spectra coincide (note the inverted horizontal scale). The black dashed line shows a degenerate two-photon excitation spectrum for comparison, recorded at the similar pressure of 40 bar (data from Fig. 5.5).

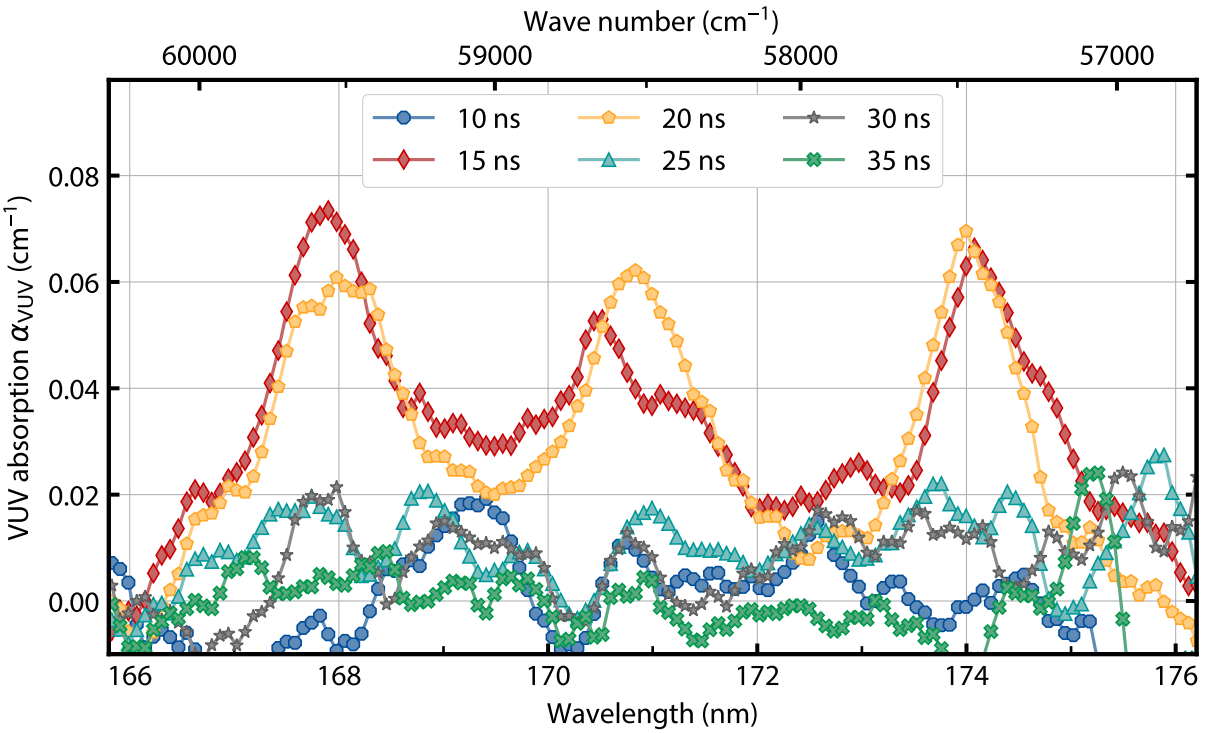

Figure 5.11: Time dependence of the two-photon VUV absorption. With a xenon sample at a pressure of 35 bar and the auxiliary light field tuned to a wavelength of 490 nm, two-photon absorption spectra are shown for different gate delays of the image intensifier within the ICCD camera. A statistically relevant VUV absorption is visible only for two gate settings within a temporal spacing of 5 ns (red and yellow curves), which coincide temporally with the arrival of the OPO pulse at the high-pressure cell.

resolution probed here. With gate delays smaller or larger than these values, no statistically relevant two-photon absorption signal α_{VUV} is observed (to obtain these data sets, fewer shots from the plasma / OPO system were averaged than for the data in Fig. 5.10, explaining the inferior signal-to-noise ratio). This further underpins the attribution of the observed spectral features to transitions from the $5p^6$ ground state to states within the $5p^5 6p$ configuration, driven by the combination of the VUV light field generated in the plasma cell and the auxiliary light field provided by the OPO system.

The two-photon absorption spectra presented in this section agree well with the expectations regarding their spectral composition and prove the general feasibility of the proposed scheme to increase the reabsorption probability of photons emitted by xenon. An enhancement of the effect to a level suitable for the thermalization of photons could be achieved by a tighter focusing of the auxiliary light field to a beam diameter of around 100 µm. This corresponds to the typical spatial extent of the thermal photon cloud in microcavity-based photon BEC experiments with common mirror geometries. Future technological improvements of VUV-mirror coatings might further enhance the feasibility of the proposed scheme by lowering the necessary absorption coefficient to ensure a sufficient number of absorption and reemission cycles.

6 | Absorption and Emission Spectroscopy of Heteronuclear Xenon-Noble Gas Mixtures

In the course of the experimental work presented in this thesis, another candidate system for a thermalization medium for VUV photons was investigated: heteronuclear, two-species mixtures between xenon and one of the other (stable) noble gases. For such systems, previous studies reported significantly less strongly bound excimers while exhibiting a similarly flat ground state potential energy curve as the xenon-xenon system [87, 88]. This is expected to result in a reduced Stokes shift between the emission on the second excimer continuum and the one-photon absorption associated with the $5p^6 \rightarrow 5p^5 6s$ transition of xenon around 147 nm (Sec. 3.2.1), facilitating a stronger reabsorption of the emission radiation, as necessary for the thermalization of VUV photons. Generally, a low-density environment of pure xenon (with its emission spectrum dominated by atoms rather than excimers) would also offer emission spectrally close to the absorption around 147 nm. Yet, due to an insufficient collision rate under these conditions, neither an energetic level substructure nor a significant line broadening are expected to arise, such that atomic systems cannot be employed for the thermalization of photons. Accordingly, the idea behind investigating heteronuclear xenon-noble gas mixtures as thermalization media is to expose xenon atoms to a buffer gas environment. This would allow to exploit emission features spectrally close to the absorption around 147 nm, but ensuring a line broadening on the order of the thermal energy and the emergence of a level substructure within a heteronuclear quasimolecular collisional manifold. As illustrated in Sec. 3.3.2, spectroscopic studies of xenon-noble gas mixtures found in literature are either based on excitation mechanisms (such as electric discharges) incompatible with conditions in a future microcavity environment or limited to the low-density regime. In this regime, the assumption of thermally equilibrated manifolds appears doubtful due to insufficiently low collision rates. This shows the necessity to conduct spectroscopic investigations also in the dense-sample regime (here referring to pressures up to roughly 100 bar).

In the beginning of this chapter, the emission spectra of heteronuclear xenon-noble gas mixtures will be presented, where xenon is the optically active constituent. The spectral composition of the corresponding emission spectra is strongly influenced both by the absolute contributions of both species and their ratio. Regarding a future application in a microcavity system, the emission spectra impose relatively stringent constraints on the suitable ranges of xenon and buffer gas contributions in the mixtures. Subsequently, absorption properties of systems defined by these constraints will be illuminated. Eventually, combining both emission and absorption data, the fulfillment of the thermodynamic Kennard-Stepanov relation will be assessed.

6.1 Emission Spectroscopy

For the emission spectroscopy of heteronuclear xenon-noble gas mixtures, it appears reasonable to optically excite the samples with light around 147 nm wavelength on the xenon $5p^6 \rightarrow 5p^5 6s$ single-photon transition, as this is the most direct excitation channel (without involvement of any intermediate states). Furthermore, in a prospective application as a thermalization mediator in a microcavity, this is also the transition that will be involved in the repeated cycles of absorption and reemission.

6.1.1 Setup

For the measurements presented in this section, the setup shown in Fig. 6.1(a) is employed, bearing close resemblance to the setup used for the degenerate two-photon excitation spectroscopy (Sec. 5.1.1). For the excitation of the gas sample, frequency-tripled light in the wavelength range from 143 nm to 147 nm is used, as obtained in a third-harmonic generation process from blue light from the OPO system (Sec. 4.5). The wavelength and pulse energy of the blue fundamental light can be tracked with a fiber-coupled spectrometer and a power meter before entering the THG cell. After separating the fundamental and the third-harmonic beam with the hole mirror, the fundamental beam is guided into a beam trap. The collimated third-harmonic beam is guided into the five-window high-pressure cell that confines the samples under investigation (which, in turn, are prepared by the gas piping system introduced in Sec. 4.3.2). Part of the ensuing radiation is collected under a right angle to the exciting beam and guided into the spectrometer based on the ICCD camera, whose image intensifier is essential for the detection of the generally low light levels originating from the investigated samples, as these typically contain only very small contributions of the optically active xenon.

For the recording of emission spectra of heteronuclear mixtures, the window geometry of the high-pressure cell is of utmost importance. In contrast to the measurements from Sec. 5.1, where the absorption and the emission are spectrally separated, here emission features in the immediate spectral vicinity of absorptive features are investigated. Correspondingly, the distance the emitted radiation has to traverse before leaving the high-pressure cell through the lateral window has to be minimized, as otherwise the actual emission spectrum could be subject to reabsorption within the sample[1] (secondary inner-filter effect [141]). The window configuration of the high-pressure cell is shown in Fig. 6.1(b). The excitation light is coupled into the high-pressure cell through a MgF_2-step window with a 5 mm-long step. The emission is monitored through a lateral MgF_2-step window with a 10 mm-long step. Radiation trapping is minimized by monitoring the emission spectrum on the ICCD camera while moving the THG beam close to the lateral step window until the emission spectrum's shape no longer changes.

[1] At this point it is worth clarifying that in future microcavity-based experiments on the thermalization of photons, reabsorption of radiation emitted by xenon or xenon-noble gas mixtures is necessary to establish a sufficient thermal contact between the photon gas and the thermalization medium. In contrast, for the emission spectroscopy as illustrated in this section, reabsorption effects within the investigated sample are to be avoided, so as to make the true emission spectrum experimentally accessible.

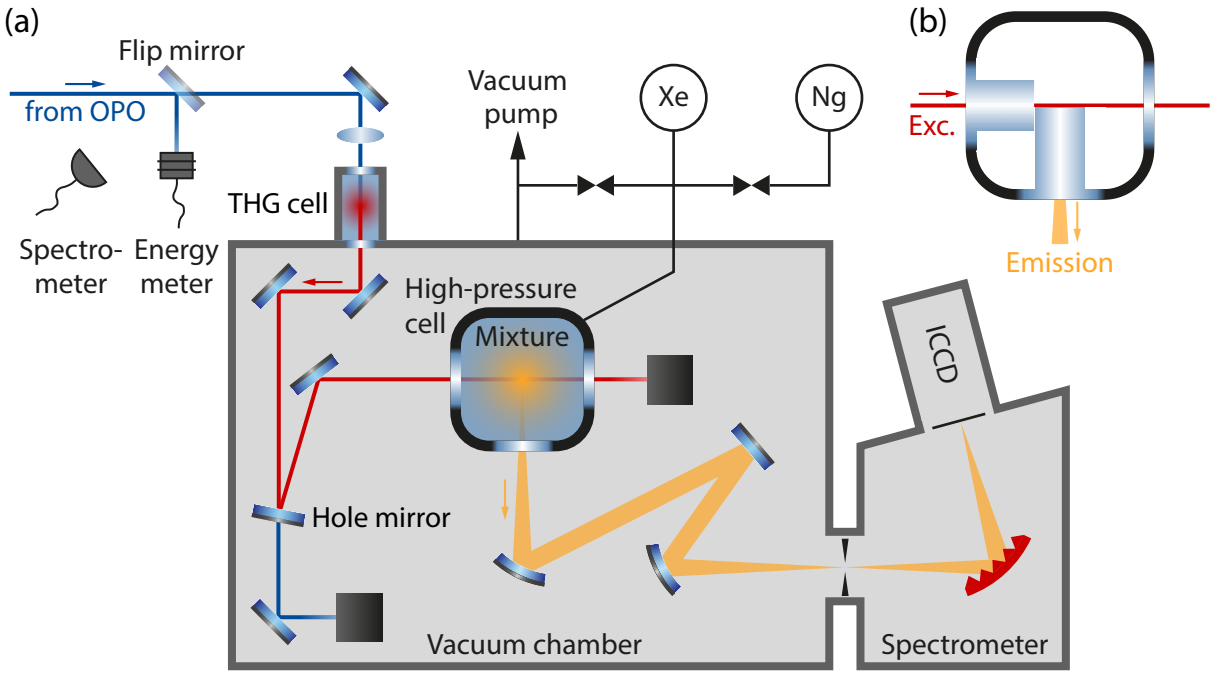

Figure 6.1: Setup for the investigation of the heteronuclear excimer emission – **(a)** Light from the OPO system (blue) in the wavelength range from 432 nm to 441 nm is frequency-tripled in a xenon-filled third-harmonic generation (THG) cell. The resulting VUV radiation (red) in the wavelength range from 144 nm to 147 nm is separated from the fundamental blue light using a hole mirror (Sec. 4.5), after which the fundamental light is guided into a beam trap and the THG light is guided into the high-pressure cell containing heteronuclear xenon-noble gas (abbreviation "Ng") mixtures under investigation. Part of the emission from the sample (yellow) is collected through a lateral MgF_2-step window and guided into an ICCD camera-based spectrometer. **(b)** Zoom-in onto the geometry of the high-pressure cell, illustrating the window arrangement. The excitation beam traverses a step window with a 5 mm-long step and is guided close to the lateral window, which exhibits a 10 mm-long step.

6.1.2 Methods and Results

Unless otherwise stated, for the recording of the emission spectra presented in the following, the center wavelength of the ICCD camera-based spectrometer was set to 170 nm, allowing to monitor the entire spectral range in which emission features are present. The sensor chip of the ICCD camera was cooled down to a temperature of −25 °C. The shot-to-shot fluctuations observed in the emission signal are more pronounced than in the case of the measurements studying two-photon excitation (Sec. 5.1). This behavior can be attributed to the frequency-tripling process of blue light for the excitation, as the fulfillment of the phase matching condition is strongly sensitive to the pressure and temperature of the gas mediating the third-harmonic generation. Correspondingly, the data for the emission spectra are averaged over typically 500 camera frames, each frame recorded with an exposure time of 0.65 s, in aggregate then leading to an effective averaging over 3000 shots from the OPO system. The ICCD camera was synchronized to the main trigger output of the laser system with its gate window set to a width of 400 ns. The gate delay was chosen such that it opened right after the excitation light around 147 nm and its fundamental light around 441 nm receded (verified by the observation

that an empty emission cell leads to no signal being detected by the ICCD camera). The gain of the image intensifier was typically set to 4000, close to the maximum setting, illustrating the generally lower light levels as compared to the measurements in Chap. 5.

The spectra that will be shown throughout this section have been corrected for the spectral response of the optical elements involved in guiding the light from its point of origin at the center of the high-pressure cell to the detector. This correction accounts for the transmission profile of MgF_2 (Fig. 4.2(a)), as well as the reflectivity profile of the grating within the spectrometer. Both the reflectivity profile of the VUV mirrors and the detection efficiency of the ICCD camera's image intensifier are spectrally uniform over the relevant wavelength range, justifying their exclusion from this correction.

A potential global wavelength offset of the emission spectra is accounted for by recording a reference curve of a pure-xenon sample at a pressure of 20 mbar (this is the lowest amount of pure xenon for which an emission signal can be detected with the used setup). At such a low pressure, no spectral line shift could be observed, such that this curve can serve as an absolute wavelength marker. Each spectrum of a heteronuclear mixture is shifted by the deviation between this wavelength marker and the atomic transition wavelength of 146.9 nm.

Balance between Homo- and Heteronuclear Excimer Emission

Figure 6.2 shows three emission spectra of xenon-helium mixtures with a fixed helium partial pressure of 30 bar, and xenon partial pressures varying between 2 and 12 mbar. This corresponds to relative xenon contributions between 67 ppm and 400 ppm (parts per million). The excitation wavelength was chosen individually for each mixture so as to maximize the obtained signal. Two emission features are evident (see also the inset of Fig. 6.2, showing the same data in a different scaling). The relatively sharp feature is centered around a wavelength of 146.4 nm, spectrally blue-shifted compared to xenon's $5p^6 \rightarrow 5p^5 6s$ atomic resonance at 146.9 nm. This shift can be considered a first indication that the observed feature can indeed be attributed to the emission of heteronuclear excimers. Conversely, the broadband spectral feature is attributed to the second excimer continuum emission of homonuclear xenon-xenon dimers. When inspecting the data, one observes that the signal-to-noise ratio of the spectra decreases with increasing xenon concentration, which might appear counterintuitive at first, as more xenon atoms should lead to a stronger emission signal. This observation, however, can be explained by the window configuration of the high-pressure emission cell. After entering the gas volume, the excitation light has to propagate through several millimeters of gas before entering the region covered by the field of view through the lateral detection window. During this propagation, a large share of the excitation light is already absorbed without its emission being detected, leaving a lower level of excitation light in the detection region (primary inner-filter effect [141]).

The visualization in the inset of Fig. 6.2 shows that the homonuclear second excimer continuum emission becomes more dominant with increasing xenon contribution. This behavior is under-

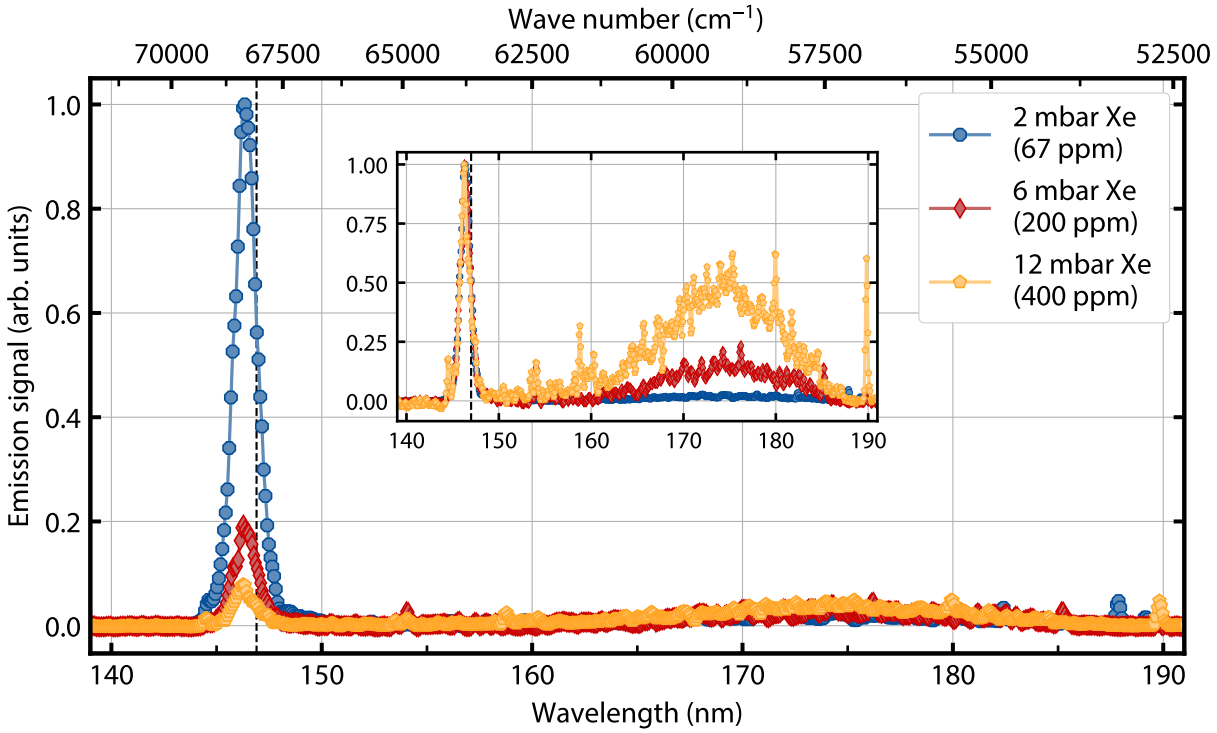

Figure 6.2: Emission spectra of three different xenon-helium mixtures. The helium pressure was kept constant at 30 bar, while the xenon contribution was changed. The inset shows the same data, but normalized to the amplitude of the emission feature around 146.4 nm. The excitation wavelength in all three measurements was chosen such that the obtained signal is maximal. The dashed black line indicates the spectral position of the transition wavelength of xenon's $5p^6 \rightarrow 5p^5 6s$ atomic resonance, 146.9 nm.

standable from the shape of the potential energy curves of the xenon-helium system and the xenon-xenon system. The much deeper potential energy well of the xenon-xenon system makes the formation of homonuclear xenon-xenon excimers energetically much more favorable than the formation of heteronuclear xenon-helium excimers. This plays a role, even if the density of xenon atoms is orders of magnitude smaller than the density of helium atoms. Illustratively, the more xenon atoms the mixture contains, the higher the probability becomes for two xenon atoms to interact and form an excimer. Once this happens, it is virtually impossible for the homonuclear excimer to dissociate, as the corresponding binding energy (507 meV) is much higher than the available thermal energy (25 meV). To investigate this scaling behavior more quantitatively, the spectral profiles from Fig. 6.2 are fitted with a combination of two Gaussian functions,

$$f(\lambda) = \frac{1}{\sqrt{2\pi}} \frac{A_{147}}{\sigma_{147}} \exp\left(-\frac{\left(\lambda - \overline{\lambda}_{147}\right)^2}{2\sigma_{147}^2}\right) + \frac{1}{\sqrt{2\pi}} \frac{A_{\mathrm{Xe_2}}}{\sigma_{\mathrm{Xe_2}}} \exp\left(-\frac{\left(\lambda - \overline{\lambda}_{\mathrm{Xe_2}}\right)^2}{2\sigma_{\mathrm{Xe_2}}^2}\right) , \tag{6.1}$$

each summand describing one of the two peaks. Figure 6.3(a) shows a good agreement between this fit function and the experimental data. For an assessment of how suitable a certain mixture

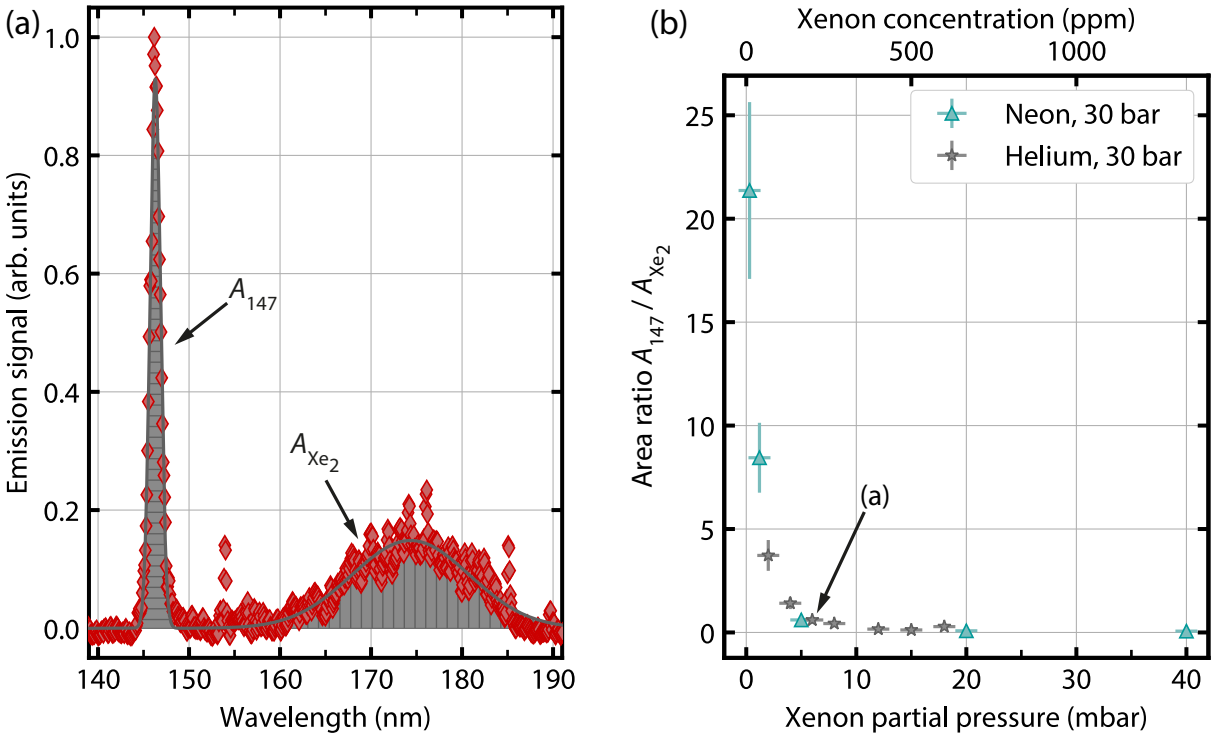

Figure 6.3: Homo- and heteronuclear emission of xenon and xenon-noble gas mixtures – **(a)** Emission spectrum of a sample of 6 mbar xenon in 30 bar helium (red curve in Fig. 6.2). The emission spectrum can well be approximated by the sum of two Gaussian functions, as expressed by Eq. (6.1) and visualized by the gray solid line. The areas under the two visible emission features are denoted by A_{147} (horizontal hatching) and A_{Xe_2} (vertical hatching), respectively. **(b)** Area ratio A_{147}/A_{Xe_2} for different mixtures between xenon and helium or neon. The arrow indicates the data point corresponding to the mixture whose emission spectrum is shown in (a). The error bars indicate the uncertainties of filling the high-pressure cell with a certain amount of gas and the uncertainties of the fit functions, respectively.

is, the area ratio A_{147}/A_{Xe_2} is considered, which is visualized in Fig. 6.3(b) for different mixtures with either helium or neon buffer gas at a pressure of 30 bar. The monotonous trend already indicated by Fig. 6.2 is evident for both buffer gases, showing the area ratio decreasing with increasing xenon pressure. Qualitatively, a similar trend can be observed for the scaling of the area ratio with the buffer gas pressure (this investigation has been done only with helium as a buffer gas). Figure 6.4 shows the area ratio in a three-dimensional visualization as a function of the xenon or helium pressure (with the respective other pressure kept constant). Clearly, also for mixtures with fixed xenon pressures of 6 mbar or 24 mbar, the area ratio decreases as the helium pressure is increased. This behavior can equally be explained by the mechanism of the formation of homonuclear excimers. In order to observe emission on the homonuclear second excimer continuum, a xenon atom in the $5p^5 6s$ state (whether immediately after optical excitation or after dissociation of a heteronuclear excimer) needs to dissipate energy, for example in a collision with a helium atom. With the probability for such a collision naturally increasing with the density of helium atoms, the addition of ever more helium to a sample aids in the formation of homonuclear xenon-xenon excimers at the expense of heteronuclear excimers.

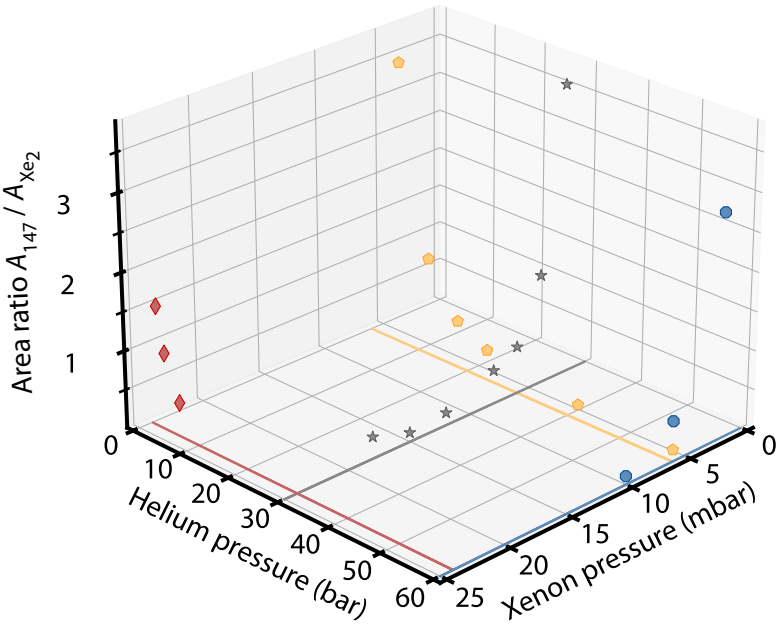

Figure 6.4: Visualization of the area ratio scaling with the xenon and the helium pressure. The area ratio A_{147}/A_{Xe_2} becomes more favorable (higher in value) both for lower helium and lower xenon pressures. The gray data set indicates the data shown in Fig. 6.3. The colored lines underneath the data sets correspond to projections of the data sets into the (x, y)-plane; for either a fixed helium pressure of 30 bar or 60 bar (gray, blue) or a fixed xenon pressure of 6 mbar or 24 mbar (yellow, red). Error bars have been omitted for clarity.

This behavior illustrates an important trade-off that needs to be considered when investigating heteronuclear xenon-noble gas mixtures as a prospective thermalization mediator. On the one hand, an emission spectrum dominated by the heteronuclear emission feature (here around 146.4 nm wavelength) is desirable, as the homonuclear emission around 172 nm is likely to leave a future microcavity system without undergoing thermalization due to the medium's transparency for this light. This would then constitute an effective loss channel and essentially replicate the situation with pure xenon samples. This constraint suggests to use gas mixtures with as small a xenon contribution as possible. On the other hand, a certain absolute absorption strength in the spectral emission region is necessary. As the absorption strength of gas mixtures is expected (and will be shown in Sec. 6.2) to increase monotonously with the xenon contribution, this constraint necessitates to use mixtures with as high a xenon contribution as possible. For now, samples exhibiting an area ratio above 1, where the heteronuclear and the homonuclear excimer emission contribute equally to the emission spectrum, are deemed suitable for a thermalization medium candidate. Looking at Fig. 6.3(b), this imposes a first estimate for an upper limit on the xenon contribution of roughly 5 mbar. A similarly high value of A_{147}/A_{Xe_2} is, as discussed, also obtained for a low buffer gas pressure, but in this limit no significant thermalization is expected due to the low interparticle collision rate.

So far, only emission data for the xenon-helium system and the xenon-neon system have been presented. In this experiment, also mixtures between xenon and the heavier species argon and

krypton have been investigated, although only to a lesser extent than the mixtures with the lighter noble gases. At the time of writing, corresponding emission measurements of xenon-argon and xenon-krypton mixtures are still the subject of experimental efforts.

Redistribution of Fluorescence

One of the key properties of a system in thermal equilibrium is the redistribution of fluorescence. More precisely, this concept requires the spectral position and shape of the emission spectrum to be independent of the excitation wavelength, encapsulated by Kasha's rule (Sec. 2.2.1). In the following, it is investigated to what extent this behavior is fulfilled by the heteronuclear emission feature. The excitation on the $5p^6 \rightarrow 5p^5 6s$ transition with light generated in third-harmonic generation from blue light proves to be very conducive for this endeavor, as it allows efficient access to the wavelength range between 143 nm and 147 nm. In units of the thermal energy, this tuning range corresponds to about $8\,k_\mathrm{B}T$, allowing a thorough probing over the relevant wavelength scale.

Subject of this investigation is a xenon-helium mixture with a xenon contribution of 0.6 mbar and a total pressure of 80 bar, the latter being close to the maximum achievable total pressure for gas mixtures in the current experimental configuration (limited by the maximum pressure rating of the sample cylinder and the volumes of the different compartments of the gas piping system, see Sec. 4.3.2). Figure 6.5(a) shows normalized spectra of the heteronuclear emission for excitation with light of two different wavelengths, 144.5 nm and 145.5 nm. The emission features well agree in shape, but are spectrally slightly shifted, with the shorter excitation wavelength leading to an emission spectrum shifted to longer wavelengths and vice versa. To investigate this behavior in more detail, Gaussian functions are fitted to the emission profiles and the peak positions of these fits are introduced as *center emission wavelengths* $\overline{\lambda}_\mathrm{em}$. Figure 6.5(b) shows the center emission wavelength as a function of the excitation wavelength λ_ex. Here, a variation of the excitation wavelength between 144 nm and 147 nm leads to a shift of the center emission wavelength of more than 0.3 nm.

In the following, the extent of this deviation from Kasha's rule will be investigated for xenon-helium samples with different xenon contributions. However, not for all samples the same range of excitation wavelengths can be probed, as varying xenon contributions in the mixtures lead to varying absorption bandwidths of a sample (as will be illuminated in more detail in Sec. 6.2). From Fig. 6.5(b), it becomes clear that a narrower range of probed excitation wavelengths would lead to a narrower observed range of center emission wavelengths, such that considering the range of center emission wavelengths alone is not appropriate to quantify the deviation from Kasha's rule. A more telling approach is to determine the deviation $\Delta \coloneqq \overline{\lambda}_\mathrm{em} - \lambda_\mathrm{ex}$ between the center emission wavelength and the excitation wavelength and to consider this quantity as a function of the excitation wavelength, as suggested in [142]. The derivative $m \coloneqq \partial\Delta/\partial\lambda_\mathrm{ex} = \partial\overline{\lambda}_\mathrm{em}/\partial\lambda_\mathrm{ex} - 1$ then reveals information about the degree to which Kasha's rule is fulfilled. For the case of a perfect redistribution of fluorescence, $\partial\overline{\lambda}_\mathrm{em}/\partial\lambda_\mathrm{ex} = 0$, the derivative would be exactly $m = -1$.

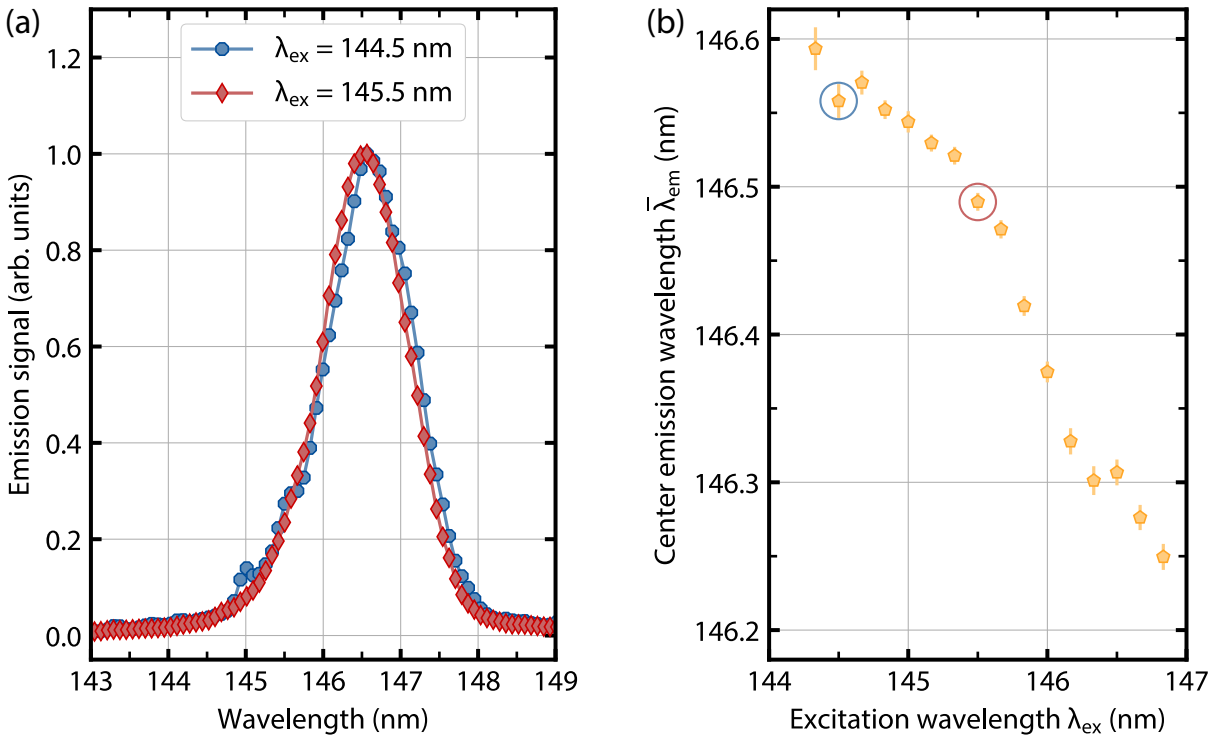

Figure 6.5: Redistribution of fluorescence in a sample containing 0.6 mbar xenon and 80 bar helium – **(a)** Normalized emission spectra of the heteronuclear excimer emission for two different excitation wavelengths λ_{ex}. The mean of a Gaussian function fitted to the data (not shown) is introduced as the center emission wavelength $\overline{\lambda}_{em}$. **(b)** Dependency between the center emission wavelength $\overline{\lambda}_{em}$ and the excitation wavelength λ_{ex}. The encircled data points are obtained from the two emission spectra shown in (a). The vertical error bars represent the uncertainty of the center wavelengths for the Gaussian functions fitted to the spectra at individual excitation wavelengths. The uncertainty on the excitation wavelength λ_{ex}, mirroring a third of the accuracy of setting the OPO system to a specific target wavelength (0.1 nm), is not visible in this visualization.

For a positive correlation, $\partial\overline{\lambda}_{em}/\partial\lambda_{ex} > 0$, it would be $m > -1$ and for a negative correlation, $\partial\overline{\lambda}_{em}/\partial\lambda_{ex} < 0$, it would be $m < -1$. Consequentially, a stronger deviation from the exceptional value of $m = -1$ here indicates a fulfillment of Kasha's rule to a lesser degree. In the following, due to its relevance in the assessment whether the redistribution is fulfilled, this slope will be referred to as *characteristic slope*.

Figure 6.6(a) shows the deviation Δ in dependence of the excitation wavelength for the gas mixture containing 0.6 mbar xenon and 80 bar helium (obtained from the data in Fig. 6.5(b)). The data can well be fitted by a linear function, yielding a slope of $m = -1.14 \pm 0.01$, indicating a deviation from Kasha's rule with a negative correlation between the excitation wavelength λ_{ex} and the center emission wavelength $\overline{\lambda}_{em}$. Such an evaluation was conducted for various samples with xenon contributions from 0.02 mbar to 10 mbar (corresponding to xenon concentrations from 0.25 ppm to 125 ppm in a helium environment of 80 bar). For each mixture, the entire range of excitation wavelengths was scanned, for which an emission spectrum could be detected. The corresponding values for the characteristic slope are visualized in Fig. 6.6(b) as a function

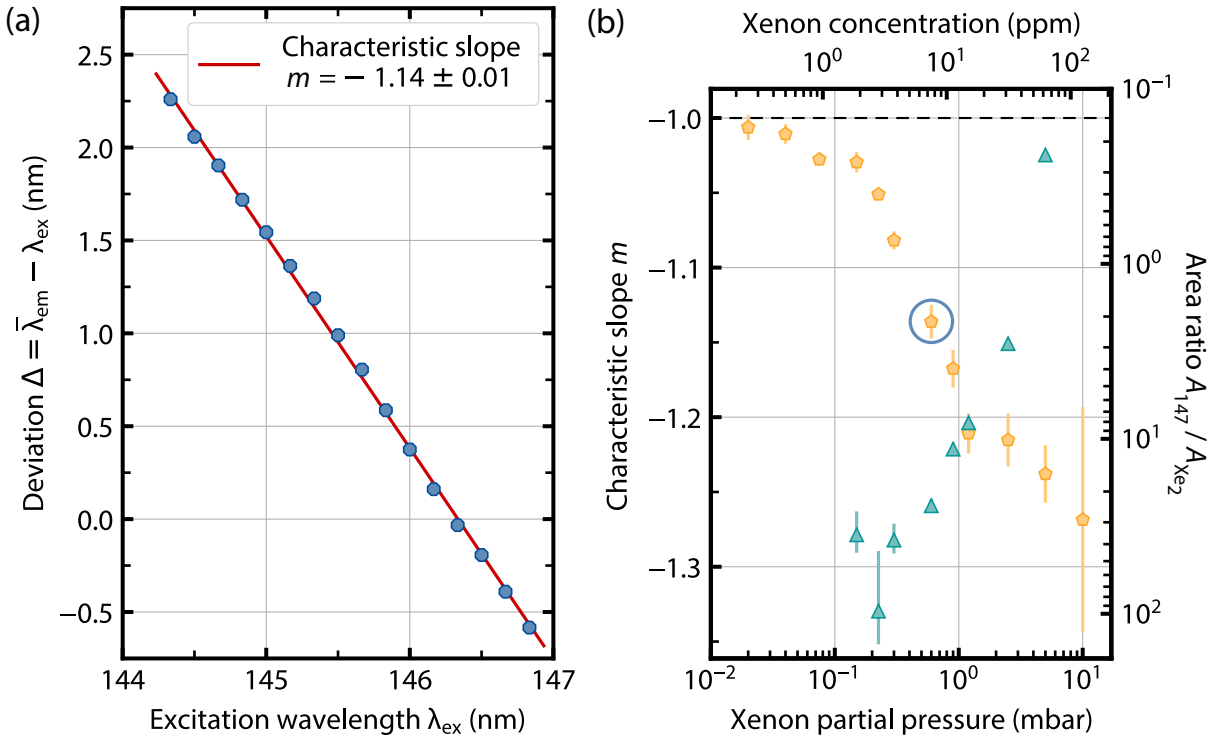

Figure 6.6: Redistribution of fluorescence – **(a)** For the sample containing 0.6 mbar of xenon and 80 bar of helium, the deviation $\Delta = \overline{\lambda}_{\mathrm{em}} - \lambda_{\mathrm{ex}}$ between the center emission wavelength and the excitation wavelength is visualized as a function of the excitation wavelength λ_{ex} (blue data points; obtained from the data in Fig. 6.5(b)). A linear function was fitted to the data (red curve), yielding a characteristic slope of $m = -1.14 \pm 0.01$. **(b)** For multiple samples containing different amounts of xenon and at a total helium pressure of 80 bar, the characteristic slope is plotted as a function of the xenon partial pressure (yellow data points, error bars representing the statistical uncertainties of the linear fit functions). The encircled data point corresponds to the data shown in (a). The horizontal dashed line indicates a characteristic slope of -1, reflecting the case of a complete redistribution of fluorescence. On the second ordinate (note the inverted scale), the area ratio $A_{147}/A_{\mathrm{Xe}_2}$ is shown (cyan).

of the xenon partial pressure. It is evident that all values are below the ideal value of $m = -1$, generally showing a negative correlation between the center emission wavelength $\overline{\lambda}_{\mathrm{em}}$ and the excitation wavelength λ_{ex}. For the smallest xenon pressures, the characteristic slope is very close to -1. Although the measurement series could not be expanded to even lower xenon contributions (due to an insufficient signal level), an asymptotic approach of the data toward a characteristic slope of $m = -1$ can be identified, indicating a virtually complete redistribution in this regime and a close fulfillment of Kasha's rule. With increasing xenon contribution, the characteristic slope becomes smaller (its absolute value becomes larger), suggesting an ever stronger deviation from Kasha's rule.

In an attempt to find an explanation for this behavior, it is worth recalling the area ratio, $A_{147}/A_{\mathrm{Xe}_2}$, as a function of the xenon contribution, which is also shown in Fig. 6.6(b). Intriguingly, the increase of the characteristic slope's deviation from -1 is clearly accompanied by a decrease of the area ratio. This suggests that an explanation for the deviation from Kasha's rule

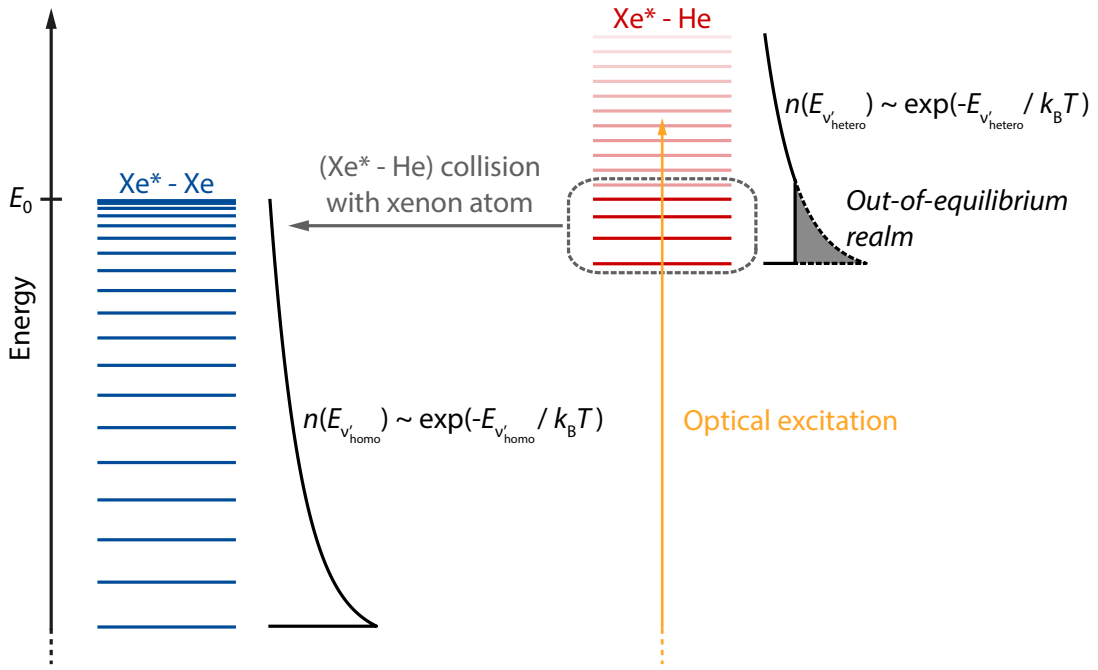

Figure 6.7: Model for a population transfer between heteronuclear and homonuclear excimers. Assuming a binary collision picture, the levels of the quasimolecular manifolds are schematically depicted in blue and red, respectively (the corresponding potential energy curves have been omitted for clarity). The energy $E_0 = {}^{hc}/_{146.9\,\mathrm{nm}}$ corresponds to the transition energy of the xenon $5p^6 \rightarrow 5p^5 6s$ atomic transition, which constitutes the asymptotic energy of both the homonuclear and the heteronuclear excimer systems. For the case of the heteronuclear excimer system, a continuum of levels is indicated in light red color above the energy E_0. Optical excitation leads to occupation of a certain level ν'_{hetero}. Subsequently, considering an ensemble of excimers, a tentative thermalization is reached in frequent interconstituent collisions. The heteronuclear excimers can be dissociated in collisions with a xenon atom, as the formation of a homonuclear xenon-xenon dimer is energetically favored. In the process, population of the lower ν'_{hetero} levels is removed (indicated by the dashed frame), leading to an interruption of the thermalization.

can be found in the increasingly efficient formation of homonuclear excimers at higher xenon concentrations. For this, the following line of arguing is considered, substantiated by the scheme shown in Fig. 6.7. In a xenon-helium mixture, heteronuclear excimers form, consisting of a xenon atom optically excited to the $5p^5 6s$ state and a helium atom in the ground state. In frequent collisions, the levels within the quasimolecular collisional manifold adopt a thermally equilibrated occupation. Although the number density of helium atoms is much higher than that of xenon atoms, it is possible that during their radiative lifetime heteronuclear excimers encounter surrounding xenon atoms. In such a collision, heteronuclear excimers can be dissociated and homonuclear xenon-xenon excimers can form in their stead, as these are energetically favored (Sec. 3.2.1). As the quasimolecular manifold of the heteronuclear excimers lies energetically above that of the homonuclear excimers, predominantly the population of the lowest levels ν'_{hetero} of the heteronuclear manifold is transferred, populating levels close to the continuum region of the homonuclear manifold. The result is a dearth of heteronuclear excimers occupying the lowest levels and a persistent interruption of the thermalization of the level occupation within

the heteronuclear manifold. The probability for a heteronuclear excimer to encounter a xenon atom naturally increases with the xenon contribution in the mixture, such that this picture of a collision-aided transfer can explain the increasing deviation from a complete redistribution for increasing xenon contributions. This model assumption would also account for the *negative* correlation between the excitation wavelength λ_{ex} and the center emission wavelength $\overline{\lambda}_{\mathrm{em}}$. Excitation with a shorter wavelength tends to result in a population of higher levels, and vice versa. In the case of an initial population of higher levels ν'_{hetero}, the redistribution of occupation to the lower levels, as imperative for the thermalization process, takes longer. Accordingly, the process of collision transfer between a heteronuclear excimer and a homonuclear excimer becomes less likely. Eventually, this leads to a lower mean occupation number and accordingly a slightly red-shifted emission spectrum upon radiative relaxation to the ground state of the heteronuclear dimer system.

6.2 Absorption Spectroscopy

In the previous section it was shown that high-pressure heteronuclear xenon-noble gas mixtures exhibit emission features spectrally close to the (atomic) absorption. This can be considered a major improvement over homonuclear xenon samples, where the emission on the second excimer continuum is strongly Stokes-shifted. However, it became evident that only samples with relatively small xenon contributions (in the order of a few mbar) qualify, which might contrast with the need for a strong reabsorption probability for photons in a future microcavity environment. Hence, when exploring heteronuclear xenon-noble gas mixtures as a prospective thermalization mediator for VUV photons, also the absorptive behavior around the spectral emission region needs to be considered. In this section, such samples will be investigated regarding their absorption spectra's composition and absolute strength.

6.2.1 Setup

The setup employed for the investigation of absorption properties of heteronuclear samples is shown in Fig. 6.8, resembling the setup illustrated in Sec. 5.2.1 for the study of the nondegenerate two-photon absorption in homonuclear xenon samples. Again, a laser-induced plasma serves as a broadband spectroscopy light source. However, this time krypton is used as a plasma target, as its light yield exceeds that of argon in the spectral vicinity of 147 nm, making it more favorable for the investigation of the heteronuclear excimer absorption. Part of its light emission is collected, collimated and guided through the two-window high-pressure cell with an optical path length of 200 µm (Sec. 4.2.2). Having traversed the cell, the light passes through a VUV-transmissive filter, suppressing visible and infrared stray light from the plasma excitation. After that, the VUV light is focused onto the entry slit of the CCD camera-based spectrometer, set to a width of 50 µm. Heteronuclear gas mixtures are created by the gas piping system illustrated in Sec. 4.3.2. As the volume of the high-pressure cell used in this setup is much smaller than that of the

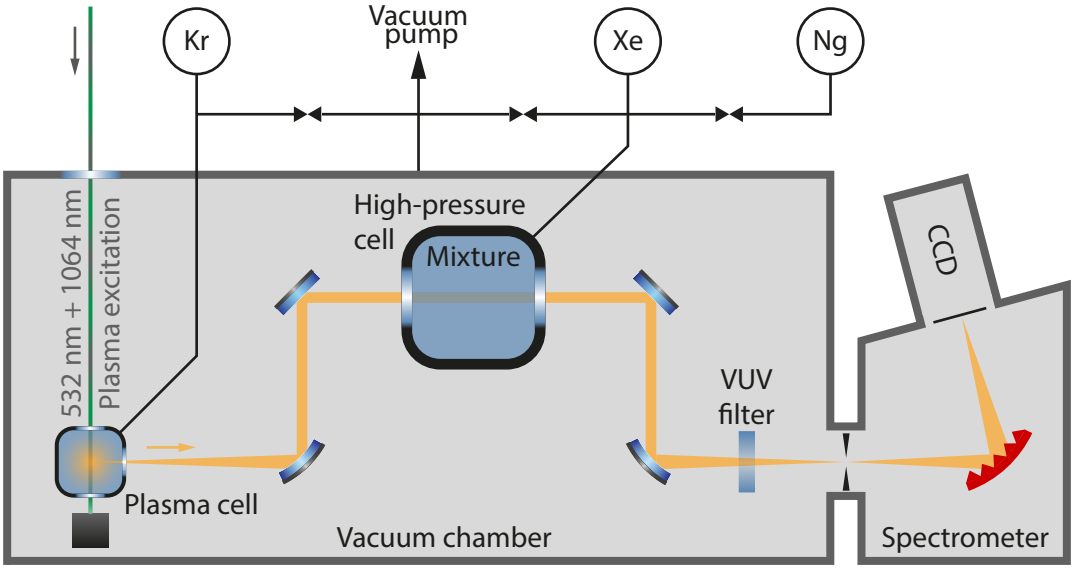

Figure 6.8: Setup for the investigation of the absorption of heteronuclear xenon-noble gas mixtures. A laser-induced plasma of krypton is used as a broadband spectroscopy light source. Part of its radiation is guided through a high-pressure cell with an optical path length of 200 µm and into a CCD camera-based spectrometer. Residual visible and infrared radiation is suppressed by a VUV-transmissive filter.

five-window cell used in the measurements on the emission properties of heteronuclear samples, buffer gas pressures of up to 90 bar can be achieved.

6.2.2 Methods and Results

The absorption spectrum of a specific sample is obtained by recording one transmission spectrum through the high-pressure cell when it is empty and one when it is filled with the sample. From the two spectra, the absorption coefficient α is calculated using Beer's law, $I_{\mathrm{gas}}(\lambda) = I_{\mathrm{empty}}(\lambda)\exp(-\alpha L)$, where $I_{\mathrm{gas}}(\lambda)$ is the measured transmission spectrum through the high-pressure cell filled with the sample, $I_{\mathrm{empty}}(\lambda)$ the transmission spectrum through the evacuated high-pressure cell and L the optical path length. All spectra are corrected for the baseline signal, which is dominated by the dark current of the CCD camera's sensor chip and residual stray light. The (spectral) photon rate of a plasma as used here has been estimated to be around $10^9\,\mathrm{nm}^{-1}\,\mathrm{s}^{-1}$ [129], resulting in a photon density much smaller than the density of xenon atoms in the sample, warranting the application of Beer's law. The absorption spectrum of a low-density xenon sample (20 mbar) serves as an absolute wavelength reference.

Figure 6.9 shows the absorption spectra of xenon-helium and xenon-neon mixtures. The total sample pressure is 90 bar and the xenon pressure varies between 0.3 mbar and 5 mbar, corresponding to xenon concentrations between 3 ppm and 56 ppm. For clarity, the spectra for the higher xenon pressures have been capped at an absorption coefficient of $\alpha_{\mathrm{cap}} = 150\,\mathrm{cm}^{-1}$, as the true value of the absorption coefficient cannot be resolved in this spectral interval due to van-

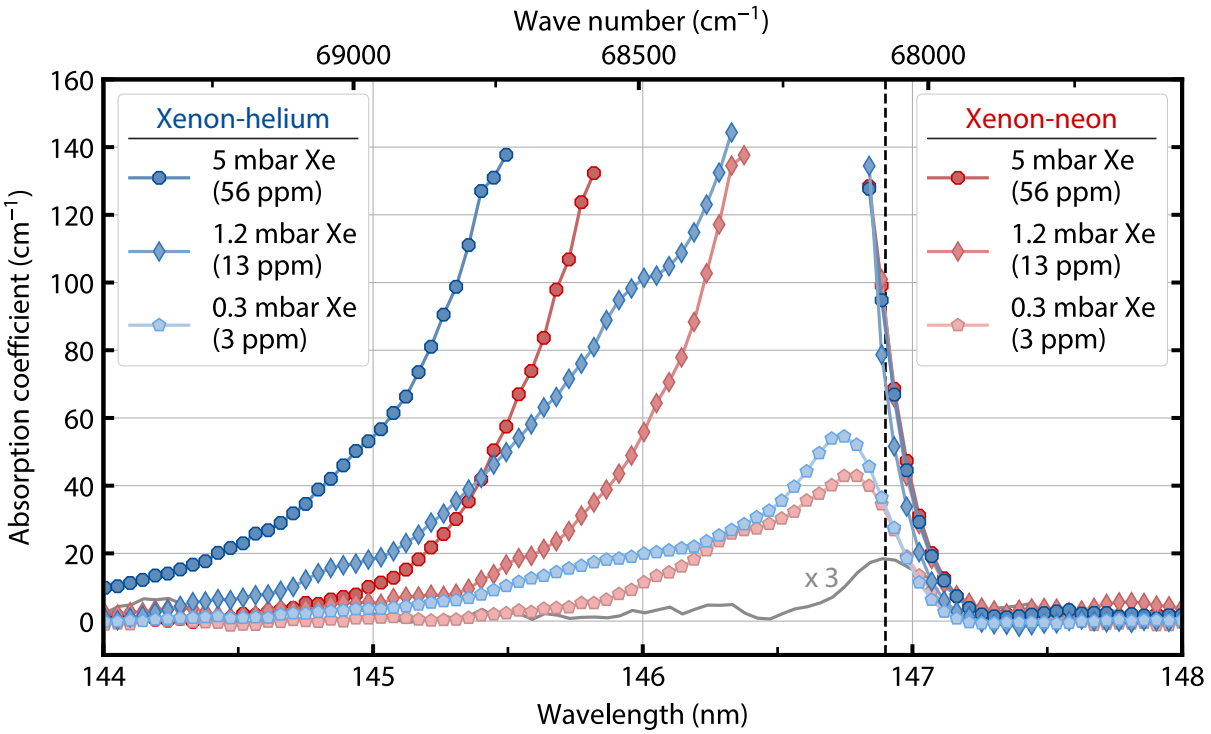

Figure 6.9: Absorption spectra of xenon-helium (blue) and xenon-neon mixtures (red) at a total pressure of 90 bar. The different markers indicate different xenon contributions between 0.3 mbar and 5 mbar. For clarity, the spectra are capped at an absorption coefficient of 150 cm^{-1}, above which the absorption coefficient can no longer be resolved with the cell used here. For comparison, also an absorption spectrum of a sample of pure xenon at a pressure of 20 mbar is shown (gray; multiplied by a factor of 3 for better visibility). The vertical dashed line indicates the spectral position of xenon's $5p^6 \rightarrow 5p^5 6s$ atomic resonance.

ishing transmission $\left(\exp\left(-150\,\mathrm{cm}^{-1} \cdot 200\,\mu\mathrm{m}\right) \approx 0.05\right)$ [143]. Generally, the absorption spectra appear blue-shifted relative to the atomic resonance at 146.9 nm; further, their short-wavelength edges drop off much more slowly than the long-wavelength edge. This observation can be made consistent with the shape of the potential energy curves (Fig. 3.4). In the heteronuclear system, the excimer equilibrium distance is at larger internuclear distances as compared to the homonuclear system, such that it coincides with the flat region of the ground state potential energy curve. Accordingly, in stark contrast to the homonuclear system, it is possible for two ground-state atoms to approach closer than the equilibrium distance of the excimer. This way, a transition into the strongly repulsive part of the excimer's potential energy curve now becomes possible, associated with absorption on the short-wavelength side of the absorption peak. Such an asymmetry has been observed earlier [111], where it has similarly been ascribed to transitions from the electronic ground state to repulsive parts of the excimer state of the xenon-helium dimer[2]. As the xenon pressure is increased from 0.3 mbar to 5 mbar, the absorption spectra increase both in absolute height and width, although their long-wavelength edges move

[2] By the same token, in Chap. 5 the observed extension of the long-wavelength absorption edge in the homonuclear system was attributed to attractive parts of the potential energy curves, i.e. downward-bending potential curves.

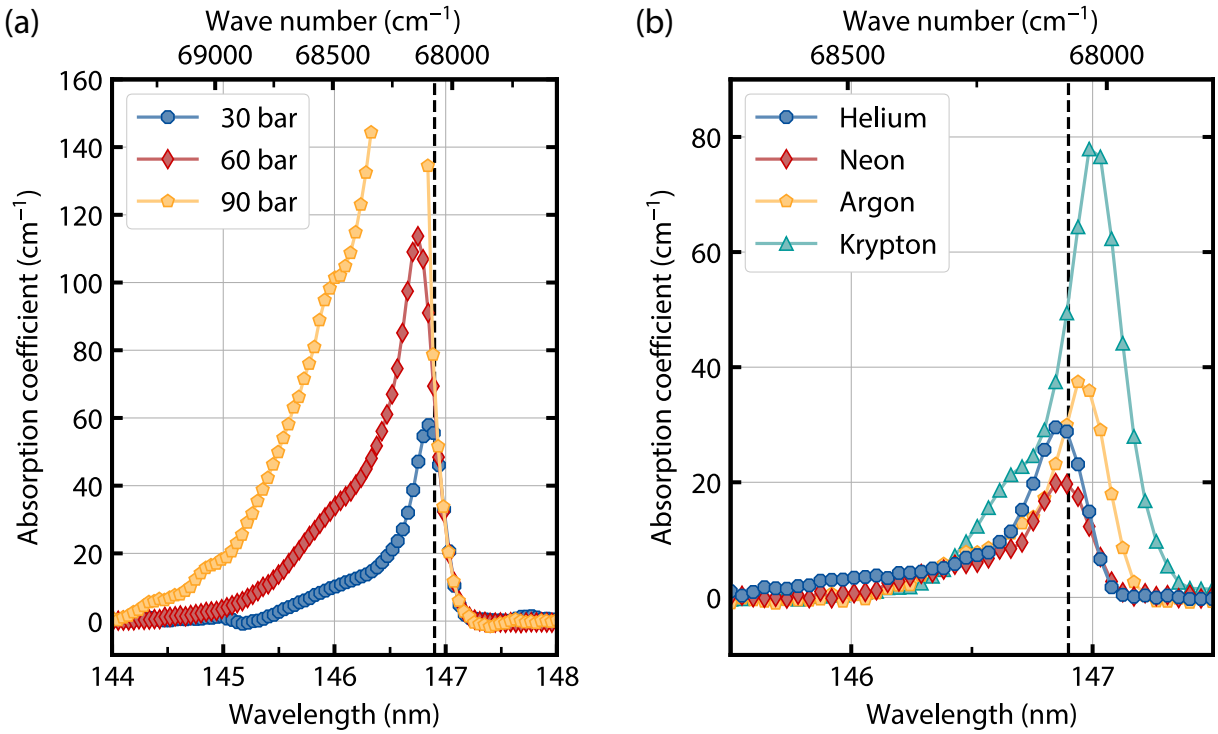

Figure 6.10: **(a)** Absorption spectra for xenon-helium mixtures at a fixed xenon pressure of 1.2 mbar and various helium pressures. The yellow curve (90 bar total pressure) corresponds to one of the data sets shown in Fig. 6.9 (blue diamonds). For clarity, the absorption spectrum has again been capped at values above 150 cm^{-1}. **(b)** Absorption spectra for mixtures between xenon and different noble gases. In all measurements, the xenon pressure was 0.2 mbar, while the noble gas pressure was 30 bar.

barely. In contrast, the short-wavelength edges shift by about 1.8 nm for the xenon-helium system (at an absorption coefficient of 40 cm^{-1}), corresponding to more than 3 $k_{\mathrm{B}}T$. The equivalent figure for the xenon-neon system is only 1.3 nm. Moreover, for each xenon contribution, the absolute absorption strength of the xenon-helium mixture exceeds that of the xenon-neon mixture. Figure 6.9 further shows the absorption spectrum of a pure-xenon sample at a pressure of 20 mbar (whose spectral position serves as an absolute wavelength reference). Interestingly, its absorption is much weaker than that of any xenon-noble gas mixture, although these contain less xenon without exception, providing evidence that the observed absorption spectra of the mixtures result from the formation of heteronuclear dimers.

Figure 6.10(a) shows absorption spectra of xenon-helium mixtures with a constant xenon pressure of 0.2 mbar and helium pressures varying between 30 and 90 bar. Similarly to the previously discussed measurement in which the xenon pressure was varied (Fig. 6.9), the helium pressure also has a strong influence on the shape and the height of the absorption spectrum. As before, the red absorption edge barely moves spectrally, whereas the blue absorption edge shifts by about 1.3 nm upon increasing the helium pressure from 30 bar to 90 bar. Overall, as a qualitative observation, the absorption becomes stronger with increasing helium pressure. At this point, it

is worth mentioning that in the data set for the lowest helium pressure, 30 bar, the width of the spectrally sharp feature close to the atomic resonance is similar to the spectral resolution of the used detection system (about 0.3 nm, compare the width of the pure-xenon absorption spectrum in Fig. 6.9). This prevents a quantitative comparison of the line areas; a spectrometer with a higher spectral resolution, as necessary for such an analysis, was not available in the course of this work.

Figure 6.10(b) shows absorption spectra for mixtures between xenon and the noble gases helium, neon, argon and krypton. The xenon partial pressure in all measurements was 0.2 mbar, which together with a noble gas pressure of 30 bar corresponds to a concentration of 6.7 ppm. The spectra of the mixtures with the lightest noble gases helium and neon coincide on their red wings, while the blue wing is broader for the lighter noble gas helium. Overall, the absorption of the helium mixture appears to be stronger, resembling the behavior seen in Fig. 6.9. The absorption spectrum of the xenon-argon mixture extends further toward long wavelengths than the spectra of either the xenon-helium or xenon-neon mixtures; also the corresponding absorption peak is shifted to longer wavelengths. Lastly, the xenon-krypton mixture exhibits the strongest absorption of all four samples investigated here and also shows the largest red-shift of the absorption peak (also note the pronounced hump on the blue side of the xenon-krypton spectrum, which is not visible in the spectra of the other mixtures). In the data presented here, the spectral position of the absorption peak evidently shifts to larger wavelengths with an increasing atomic number of the buffer gas. This is an indication for more strongly bound excimer configurations for compounds with higher atomic numbers. This appears plausible, considering the mechanism of excimer formation. The covalent bonding between a xenon atom and a noble gas atom is mediated by a shared valence electron (Sec. 3.1). With increasing atomic number of the noble gas, this valence electron is ever less strongly bound to the noble gas nucleus, allowing a stronger bonding between the xenon atom and the noble gas atom. These findings can be considered further evidence that the absorptive behavior observed in this chapter is associated with the formation of heteronuclear dimers. A pressure broadening within the limits of the impact approximation [144], i.e. not based on the formation of dimers, would not result in absorption spectra whose spectral position and shape depend as strongly on the type of buffer gas. Rather, the form of the absorption spectra appears to be governed by the relevant potential energy curves of the heteronuclear dimer systems.

6.3 Spectral Overlap and Kennard-Stepanov Analysis

In the previous sections, absorption and emission spectra of various xenon-noble gas mixtures have mostly been treated isolated from each other. For the employment of such mixtures as a thermalization medium in experiments on the Bose-Einstein condensation of photons, however, the relation between absorption and emission spectra is highly significant, as they need to fulfill the thermodynamic Kennard-Stepanov relation (Sec. 2.2.1). Figure 6.11 simultaneously shows absorption and emission spectra of xenon-helium mixtures at a total pressure of 80 bar.

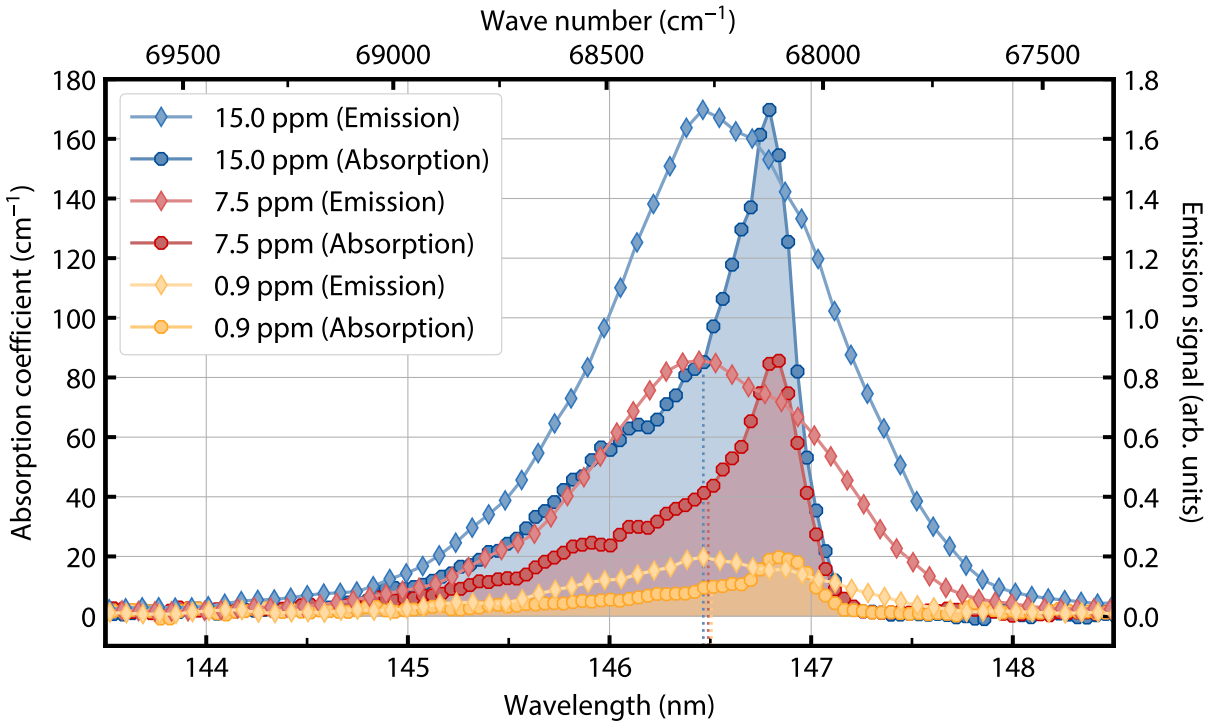

Figure 6.11: Spectral overlap of absorption and emission profiles of xenon-helium mixtures at a total sample pressure of 80 bar. The xenon contributions are 0.075 mbar, 0.6 mbar and 1.2 mbar, respectively, corresponding to concentrations of 0.9 ppm, 7.5 ppm and 15.0 ppm. The emission spectra (diamond markers) are those from the measurements in Sec. 6.1.2 recorded at an excitation wavelength of $144.\overline{6}$ nm. For clarity, the emission spectra have been scaled to match in height the corresponding absorption profiles (octagon markers, shaded areas under the curves). The vertical dotted lines indicate the center-of-gravity wavelengths of the strongly asymmetric absorption profiles.

The xenon contributions of the mixtures are 0.075 mbar, 0.6 mbar and 1.2 mbar, corresponding to xenon concentrations of 0.9 ppm, 7.5 ppm and 15 ppm. The excitation wavelength for the emission measurements was $144.\overline{6}$ nm (this is the shortest wavelength for which emission spectra are available for all three samples). The absorption spectra lie well within the emission profiles, i.e. there exists a large spectral overlap between the absorption and the emission spectral profiles. At first glance, judging only from the peaks of the respective spectral profiles, it might appear as though the emission spectra even lie at smaller wavelengths than the absorption spectra. However, this impression is a result of the strong asymmetry of the absorption profiles. The center-of-gravity wavelengths of the absorption profiles (also indicated in Fig. 6.11) coincide well with the spectral peak positions of the mostly symmetric emission spectra. This observation is broadly in line with the assumption of rather shallow potential wells of excimer states in heteronuclear xenon-noble gas mixtures (Sec. 3.2); a shallower potential well is mirrored in a smaller spectral gap between the absorption and the emission profiles.

Considering, in particular, the sample with a xenon concentration of 15 ppm, the maximum absorption coefficient within the spectral emission region is in the order of 170 cm^{-1}. This is in

the same order of magnitude as the "target" value in the context of Bose-Einstein condensation of photons, $300\,\mathrm{cm}^{-1}$ (Sec. 2.3). The full width at half maximum (FWHM) of the absorption spectrum is in the order of 0.5 nm, suggesting that a large share of the emission spectrum is likely to be reabsorbed. This constitutes a significant improvement over the situation in the homonuclear system. Further, it has to be kept in mind that for this very sample, the area ratio $A_{147}/A_{\mathrm{Xe}_2}$ is around 8 (Fig. 6.6(b)), implying that the emission spectrum is dominated by heteronuclear excimers. In the future, it is even conceivable to employ samples with slightly more xenon or helium, exhibiting even stronger (re)absorption.

In Sec. 2.2.1, the thermodynamic Kennard-Stepanov relation has been introduced, linking absorption and emission in a Boltzmann-like frequency scaling,

$$\frac{\varepsilon(\overline{\nu})}{\alpha(\overline{\nu})} \propto \overline{\nu}^3 \cdot \exp\left(-\frac{hc\overline{\nu}}{k_\mathrm{B}T_\mathrm{s}}\right) , \tag{6.2}$$

at the spectral temperature T_s. With now both absorption $\alpha(\overline{\nu})$ and emission spectra $\varepsilon(\overline{\nu})$ available, the fulfillment of this relation can be assessed. Figure 6.12 shows the quantity $\log\left(\alpha(\overline{\nu})/\varepsilon(\overline{\nu})\right)$ as a function of the wave number $\overline{\nu}$ for the three samples covered by Fig. 6.11, along with fit functions according to Eq. (6.2). Within a certain wavelength range, the data agree well with the fit functions, although the obtained spectral temperatures ($(106 \pm 22)\,\mathrm{K}$, $(93 \pm 7)\,\mathrm{K}$ and $(84 \pm 5)\,\mathrm{K}$ with increasing xenon contribution) differ from ambient temperature, $T = 295\,\mathrm{K}$. This finding, however, has to be assessed against the backdrop of the observations from Sec. 6.1.2, where a characteristic slope smaller than -1 has already hinted at deviations from a perfect redistribution of fluorescence in this heteronuclear excimer system. Despite the differences between the spectral temperatures and ambient temperature, the scaling between the spectral profiles of absorption and emission conveyed by Eq. (6.2) can be retrieved in the data of Fig. 6.12. Accordingly, the Kennard-Stepanov relation can be considered to be fulfilled, suggesting a (partial) thermalization of the level occupation within the quasimolecular collisional manifold of heteronuclear xenon-helium excimers. For any given sample, the range in which the Kennard-Stepanov relation is fulfilled can be identified as the long-wavelength edge of the respective absorption spectrum. For the sample with the highest xenon concentration investigated here, 15 ppm, this amounts to about 0.5 nm. This figure roughly corresponds to $k_\mathrm{B} \cdot 295\,\mathrm{K}$, the thermal energy at room temperature (which constitutes the relevant energy scale for the thermalization of photons). If the spectral temperature obtained from the fit is invoked, 84 K, the same spectral range even corresponds to more than $3 \cdot k_\mathrm{B}T_\mathrm{s}$.

The discussion in this section has so far been limited to the emission spectrum recorded at an excitation wavelength of $144.\overline{6}\,\mathrm{nm}$, which was the shortest wavelength for which emission spectra for all three samples investigated could be recorded ("blue excitation"). As has been observed in Sec. 6.1.2, however, the center emission wavelength depends on the excitation wavelength. This suggests to conduct a Kennard-Stepanov analysis also for the longest excitation wavelength for which emission data are available for all samples, which in this case is $146.\overline{6}\,\mathrm{nm}$ ("red excitation").

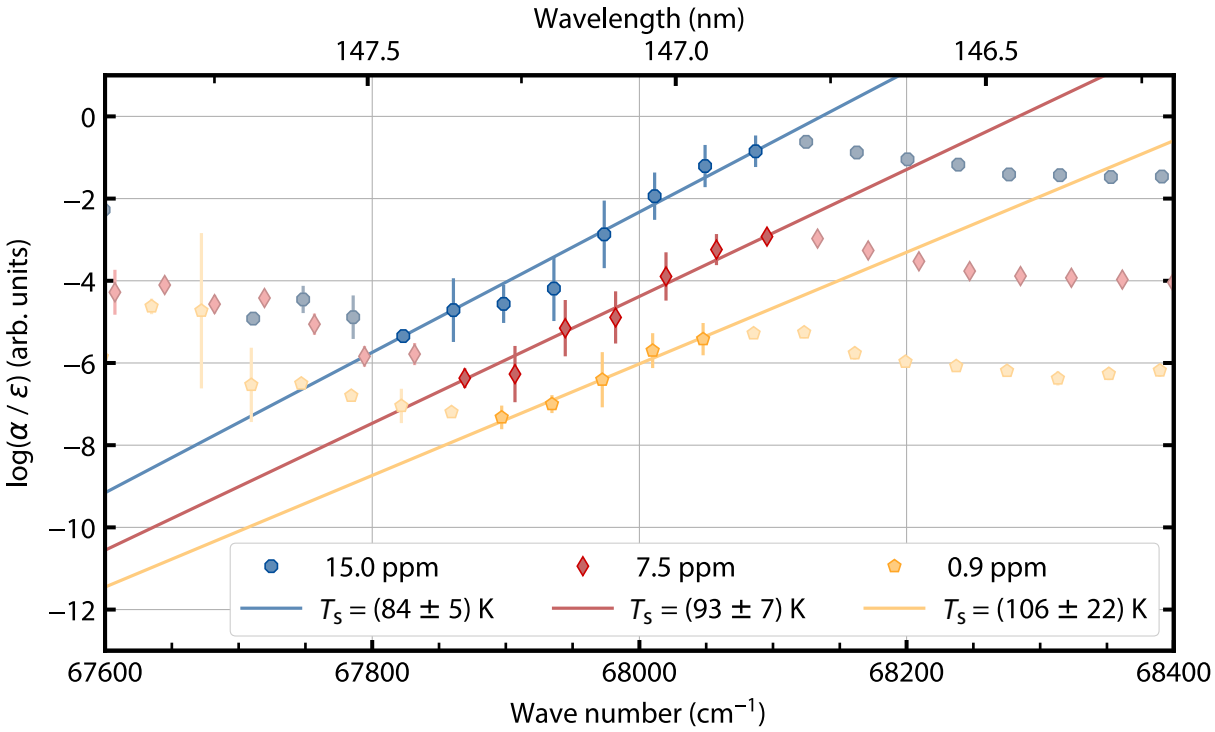

Figure 6.12: Kennard-Stepanov analysis for xenon-helium mixtures. Based on the absorption and emission spectra ($\alpha(\overline{\nu})$ and $\varepsilon(\overline{\nu})$, respectively) from Fig. 6.11, the quantity $\log\left(\alpha(\overline{\nu})/\varepsilon(\overline{\nu})\right)$ is calculated and visualized as a function of the wave number $\overline{\nu}$ (the data has been vertically shifted for clarity). The vertical error bars result from an assumed uncertainty of 0.1 nm on the absolute spectral positions of the absorption and emission spectra, as these have been recorded with different spectrometers. Functions given by Eq. (6.2) were fitted to the data (solid lines), yielding the spectral temperatures T_s. Only the not-grayed-out data points are included in the fits.

For this data set, the overlap between the absorption and emission spectra, the former being the same as in Fig. 6.11, is shown in Fig. 6.13(a). As expected, the peaks of the emission spectra here are observed at shorter wavelengths than those in Fig. 6.11. Similarly as before, this shift appears to scale monotonously with the xenon contribution in the samples. Figure 6.13(b) shows the Kennard-Stepanov analysis based on this data. Again, the data can be described by a function according to Eq. (6.2); interestingly, in the same spectral range as that shown in Fig. 6.12, corresponding to the red edge of the absorption spectrum. The spectral temperatures obtained under blue and red excitation agree within error margins, which appears evident on closer examination of Eq. (6.2). Approximating the long-wavelength edge of the emission spectrum $\varepsilon(\overline{\nu})$ to be of exponentially decaying shape, a spectral shift leads to a vertical offset of the quantity $\log\left(\alpha(\overline{\nu})/\varepsilon(\overline{\nu})\right)$, but does not change the spectral temperature, which is independent of such an arbitrary vertical offset. Data on the spectral overlap between absorption and emission and the Kennard-Stepanov analysis for the xenon-neon system can be found in App. C (Figs. C.1 and C.2), showing generally the same behavior as that presented in this section for the xenon-helium system.

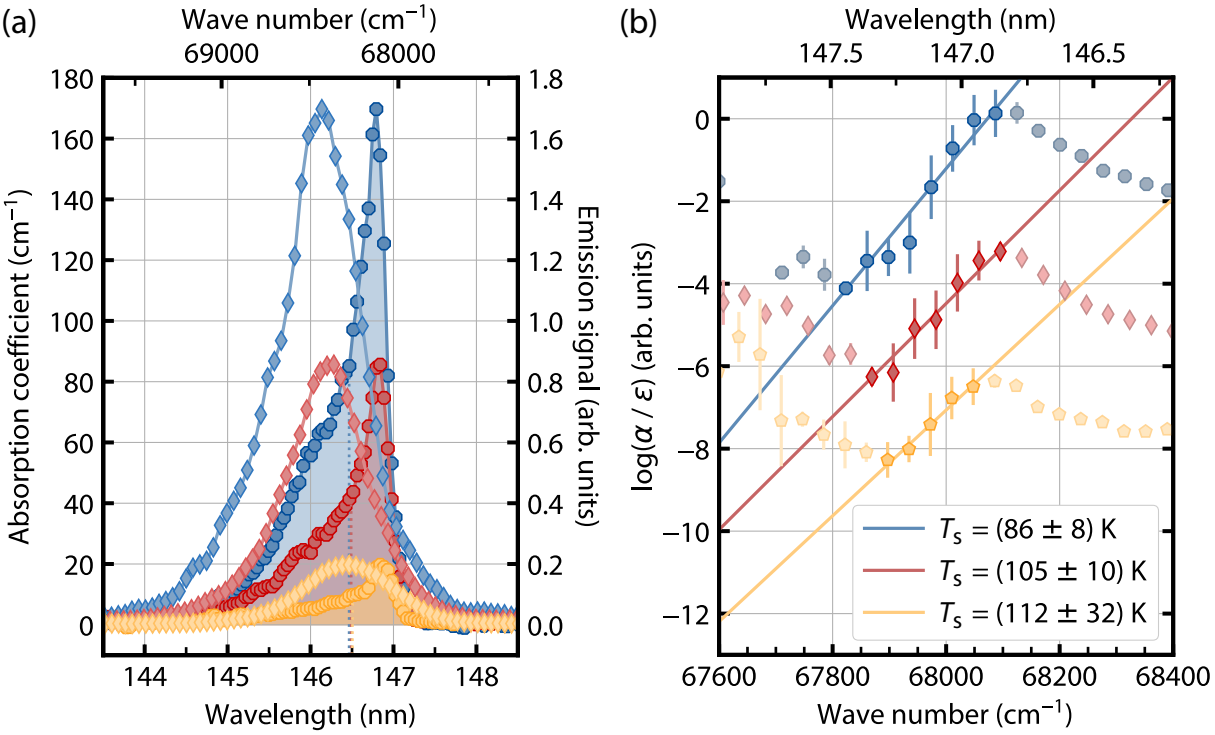

Figure 6.13: **(a)** Spectral overlap between absorption and emission spectra for the same samples as in Fig. 6.11, but with the emission spectra recorded at a longer excitation wavelength of $146.\overline{6}$ nm. **(b)** Kennard-Stepanov analysis, analogous to the visualization from Fig. 6.12.

7 Conclusion and Outlook

In this work, xenon and xenon-noble gas mixtures were spectroscopically investigated, aiming at an assessment of their suitability as a thermalization mediator for the Bose-Einstein condensation of photons in the vacuum-ultraviolet spectral regime. A prospective thermalization mediator needs to exhibit a sufficient reabsorption probability for its own emission light; moreover, the spectral profiles of absorption and emission need to fulfill the thermodynamic Kennard-Stepanov relation. This work significantly expands the available scientific literature, both in terms of the covered pressure range as well as the utilized excitation mechanisms. Key aspects of the present thesis are the following:

- Two-photon excitation spectroscopy of the homonuclear xenon system has been conducted in samples with pressures as high as 95 bar, covering both the gaseous and the supercritical regimes. Transitions between the $5p^6$ ground state and the $5p^5 6p$ and $5p^5 6p'$ excited state configurations were driven using UV-light, while monitoring emission on the second excimer continuum emission around 172 nm wavelength. The obtained excitation spectra agree well with expectations regarding their spectral composition. For increasing pressures, a pronounced spectral broadening is observed, which can be attributed to the shape of the relevant potential energy curves. These measurements illustrate the suitability of a two-photon excitation scheme to pump future xenon-based Bose-Einstein condensates of vacuum-ultraviolet photons.

- The xenon $5p^6 \rightarrow 5p^5 6p$ two-photon transitions have been driven nondegenerately, involving two photons of different wavelengths, in a homonuclear xenon sample at a pressure of 35 bar. Similar as in the case of degenerate excitation, distinct spectral features were observed that can be identified with the allowed two-photon transitions. In the measurements presented here, the absolute strength of the two-photon absorption in this scheme as yet appears rather low. Nevertheless, it was demonstrated that the (re)absorption probability of photons emitted on the second excimer continuum can in principle be enhanced by provision of an auxiliary light field of suitable wavelength. In a future microcavity application, the strength of the observed effect could be increased to a sufficient level by a tighter focusing of the auxiliary light field.

- Mixtures between xenon and the lighter noble gases have been spectroscopically investigated, as such systems constitute alternative thermalization mediator candidates. The observed emission spectra show spectral features in close vicinity to xenon's atomic resonance at 146.9 nm, which are ascribed to the emission by weakly bound heteronuclear excimers. A dependency between the spectral position of these features and the excitation wave-

length is observed. It is attributed to the competing formation of homonuclear excimers, becoming more relevant with increasing xenon concentration in the sample. Absorption measurements reveal a monotonous scaling between the xenon pressure and the absorption strength. It was possible to identify a certain range of xenon contributions in which the absorption is in a suitable order of magnitude for a sufficient reabsorption probability in a future microcavity application, while the emission spectrum is still dominated by the emission from heteronuclear excimers. The fulfillment of the Kennard-Stepanov relation was (partially) validated. Although the obtained spectral temperatures are below ambient temperature, the predicted scaling between absorption and emission could be observed, indicating a partial thermalization of the heteronuclear quasimolecular manifolds.

For the future, the next major goal on the route to the realization of a Bose-Einstein condensate of vacuum-ultraviolet photons is the observation of a thermalized two-dimensional photon gas in this spectral regime. For this, at the time of writing, heteronuclear noble gas mixtures seem to be the most suitable thermalization mediator. Preparations for this endeavor are already running, currently at the stage of setting up a new experimental platform, at the center of which will be the high-pressure microcavity presented in App. A. In this new setup, the initial creation of a photon gas within the microcavity is envisaged to be realized by driving xenon's $5p^6 \rightarrow 5p^5 6s'[1/2]_1$ one-photon transition. The necessary radiation, at a wavelength of around 129.6 nm, can be generated via third-harmonic generation of ultraviolet light (similarly as was done in this thesis to generate radiation around 147 nm for the emission measurements). The photon gas inside the cavity is expected to be driven toward thermal equilibrium via repeated cycles of absorption and reemission of photons by the xenon-noble gas mixture. Based on the results of the present thesis, the expectation to observe (partially) thermalized photon spectra appears justified, with the equilibrium temperature anticipated to correspond to the spectral temperature of the thermalization mediator. The low-energy cutoff, adjustable via the length of the microcavity, will be chosen to lie within the emission bandwidth of the thermalization mediator.

The use of pump radiation near 129.6 nm wavelength, which is deep in the vacuum-ultraviolet spectral range, appears to be a viable scheme to demonstrate the thermalization and Bose-Einstein condensation in a two-dimensional photon gas. This pump radiation can be supplied by pulsed frequency-tripled laser sources. In contrast, to operate the photon condensate in a continuous-wave mode, a pumping with longer-wavelength sources appears more suitable, given the absence of powerful continuous-wave laser-based light sources below 200 nm wavelength. Conceptually, this should be feasible using the two-photon excitation scheme demonstrated in this thesis.

Photon condensates at even shorter wavelengths could be realized by employing the optical transitions of one of the lighter noble gases instead of xenon, such as krypton or argon. Spectroscopic investigations regarding their suitability as thermalization mediators can be performed using the experimental platforms and techniques developed in the course of this thesis.

A | High-Pressure Microcavity

For the observation of Bose-Einstein condensation of photons, a suitable microcavity is needed. Considering a high-pressure gas environment the most likely candidate as a thermalization mediator, the development of such a platform poses a significant challenge, as two seemingly contradictory requirements need to be fulfilled. On the one hand, the assembly needs to confine gaseous samples and to be of sufficient rigidity to withstand pressures of at least 100 bar. On the other hand, the microcavity (or at least one of its constituent mirrors) needs to be adjustable on a sub-micrometer scale. As part of the work presented here, a high-pressure microcavity fulfilling these criteria was designed. Only a short overview shall be given here; more details on the device can be found in the master thesis of Franz Huybrechts [145].

The general idea behind the design approach here was to incorporate an adjustable mirror mount into a high-pressure container, allowing to adjust one of the mirrors that will constitute the microcavity. Figure A.1 shows a visualization of the cylindrical high-pressure container, which essentially consists of three main parts. The lower part (as the other parts made from stainless steel), constitutes one of the end caps of the high-pressure container. It houses a plano-concave MgF_2-substrate, onto whose concave side ($R = 1\,\mathrm{m}$) a VUV-reflective coating has been applied (*Laseroptik* coating B-19370). This entity represents one of the mirrors of the microcavity; at the same time, it constitutes the boundary between the confined gas volume and the outside. As it is fixed within the stainless-steel end cap, it cannot be adjusted. The transmissivity of the MgF_2-substrate allows the incoupling of pump radiation with wavelengths as short as 115 nm and detect VUV radiation from within the microcavity. The middle part is the centerpiece of the high-pressure container. Besides housing the connector to the gas piping system, it accommodates a mirror mount (*Radiant Dyes* MXI-HS-C-3-3025-M6) with three adjustment screws. This mirror mount in turn holds the second mirror of the microcavity (which is of equal type as the first mirror). Via the three adjustment screws, both the distance as well as the orientation of this mirror relative to the first, fixed-position mirror can be varied. The handles of the screws are modified to house eight neodymium (NdFeB) magnets (not visible in Fig. A.1). The upper part of the high-pressure container, constituting its second end cap, houses a sapphire optical viewport (not visible in Fig. A.1), attached to the metal via active soldering [146]. This viewport can be used for optical inspection, alignment purposes or the incoupling of pump light into the microcavity. Furthermore, this part has three recesses, into which the magnet-equipped screw handles protrude. Each recess is circumvented by eight further neodymium magnets. The combination of the inner and the outer magnets constitutes a rotary feedthrough, which allows the precise adjustment of the mirror mount even with a fully assembled and gas-filled high-pressure container.

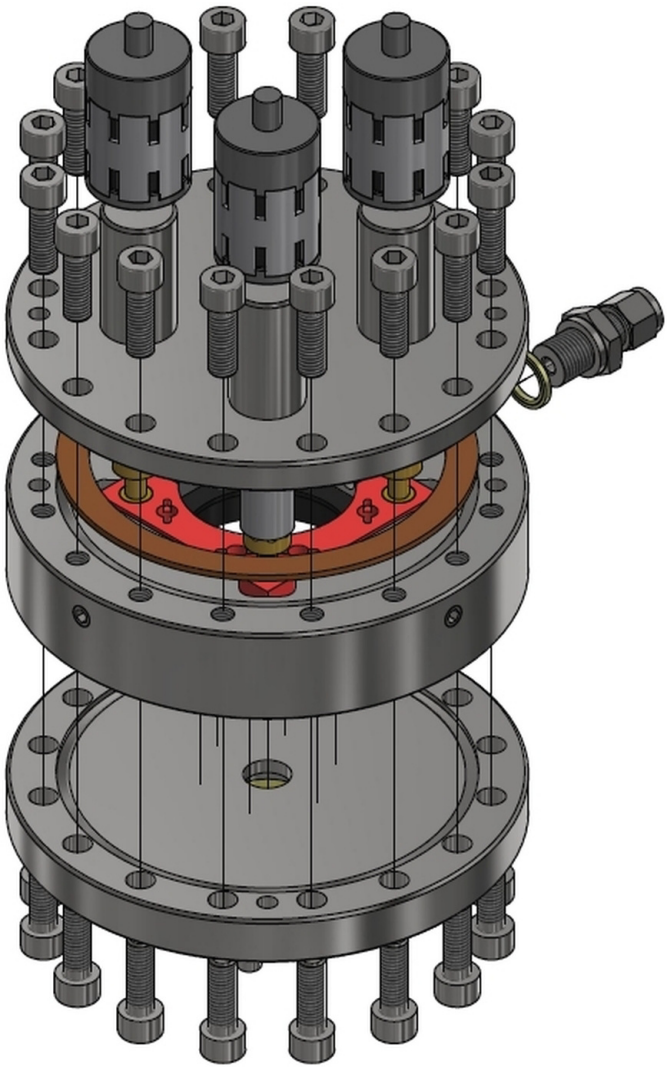

Figure A.1: High-pressure container incorporating a microcavity for the vacuum-ultraviolet spectral range [147]. One of the microcavity mirrors is housed by the lower end cap of the container. The other mirror is held by a customized mirror mount (red), allowing the adjustment of the corresponding mirror. Fully assembled, the high-pressure container has a diameter of 150 mm and a thickness of 55 mm (excluding the protrusions of the upper end cap).

The device as described here has been manufactured by the in-house fine mechanics workshop. Subsequently, to enable the microcavity adjustment even when the high-pressure container is situated in a vacuum chamber, the rotary feedthroughs were equipped with connectors to stepper motors. With these, the possibility of adjusting the mirror orientation with sufficient accuracy for the operation of a microcavity was proven [148].

B | Racah Notation for Noble Gases

A widely used notation for states of excited heavy noble gases is the Racah notation [149]. For a single excited electron, it is given by [150]

$$\underbrace{\left(^{2S_\mathrm{p}+1}L_{J_\mathrm{p}}\right)}_{\text{Parent ion}}\underbrace{nl\,[K]^\mathrm{o}_J}_{\text{Electron}}\,,$$

where the first part refers to the quantum numbers of the parent ion (subscript "p") and the second part refers to the quantum numbers of the excited electron. In this scheme, the parent ion's total angular momentum $\vec{J}_\mathrm{p} = \vec{L}+\vec{S}_\mathrm{p}$ and the excited electron's orbital angular momentum $\vec{l}$ couple to form $\vec{K} = \vec{J}_\mathrm{p}+\vec{l}$. The resulting vector couples with the spin of the excited electron, $\vec{J} = \vec{K} + \vec{s}$. As the parent ion lacks only one electron to a completely-filled p-shell, its configuration can only be $^2P_{1/2}$ or $^2P_{3/2}$. This differentiation is usually absorbed in the electron configuration, with $nl'\,[K]_J$ indicating a parent ion in the $J_\mathrm{p} = 1/2$ state and $nl\,[K]_J$ indicating one in the $J_\mathrm{p} = 3/2$ state. The superscript "o" indicates odd parity of a particular state. By convention, this superscript is omitted in case of even parity.

For an excited s-electron ($l = 0$), this coupling results in four possible states. For $J_\mathrm{p} = {}^3\!/_2$, $K = J_\mathrm{p} + l$, ..., $|J_\mathrm{p} - l| = {}^3\!/_2$ and $J = K + s$, ..., $|K - s| = 2, 1$. For $J_\mathrm{p} = {}^1\!/_2$, $K = {}^1\!/_2$ and $J = 1, 0$. In total, this results in the four states

$$ns[3/2]_2 \qquad ns[3/2]_1 \qquad ns'[1/2]_1 \qquad ns'[1/2]_0\,.$$

For a p-electron ($l = 1$), there are ten states. For $J_\mathrm{p} = {}^3\!/_2$, $K = {}^5\!/_2, {}^3\!/_2, {}^1\!/_2$ and, correspondingly, $J = 3, 2, 2, 1, 1, 0$. For $J_\mathrm{p} = {}^1\!/_2$, $K = {}^3\!/_2, {}^1\!/_2$ and $J = 2, 1, 1, 0$. In total, this yields

$$ns[5/2]_3 \qquad ns[5/2]_2 \qquad ns[3/2]_2 \qquad ns[3/2]_1 \qquad ns[1/2]_1 \qquad ns[1/2]_0$$

and

$$ns'[3/2]_2 \qquad ns'[3/2]_1 \qquad ns'[1/2]_1 \qquad ns'[1/2]_0\,.$$

C | Additional Spectroscopic Data

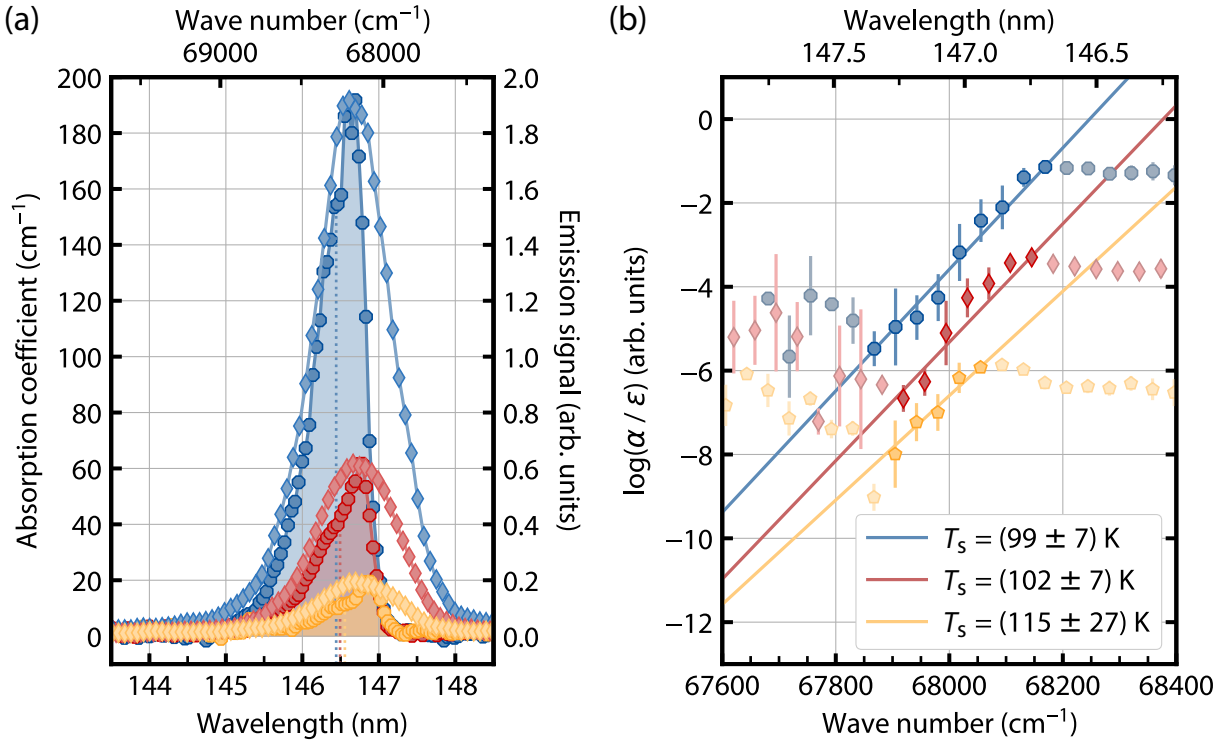

Figure C.1: (a) Spectral overlap of absorption and emission profiles of xenon-neon mixtures at a total sample pressure of 90 bar. The xenon contributions are 0.075 mbar (yellow), 0.3 mbar (red) and 1.2 mbar (blue), respectively; this corresponds to concentrations of 0.8 ppm, 3.3 ppm and 13.3 ppm. The emission spectra (diamond markers) were recorded at an excitation wavelength of $145.1\overline{6}$ nm. For clarity, the emission spectra have been scaled to match in height the corresponding absorption profiles (octagon markers, shaded areas under curves). The vertical dotted lines indicate the center-of-gravity wavelengths of the strongly asymmetric absorption profiles. **(b)** Kennard-Stepanov analysis for xenon-neon mixtures. Based on the absorption and emission spectra ($\alpha(\overline{\nu})$ and $\varepsilon(\overline{\nu})$, respectively) from (a), the quantity $\log\left(\alpha(\overline{\nu})/\varepsilon(\overline{\nu})\right)$ is calculated and visualized as a function of the wave number $\overline{\nu}$ (the data has been vertically shifted for clarity). Functions given by Eq. (6.2) were fitted to the data (solid lines), yielding the spectral temperatures T_s. Only the not-grayed-out data points are included in the fits.

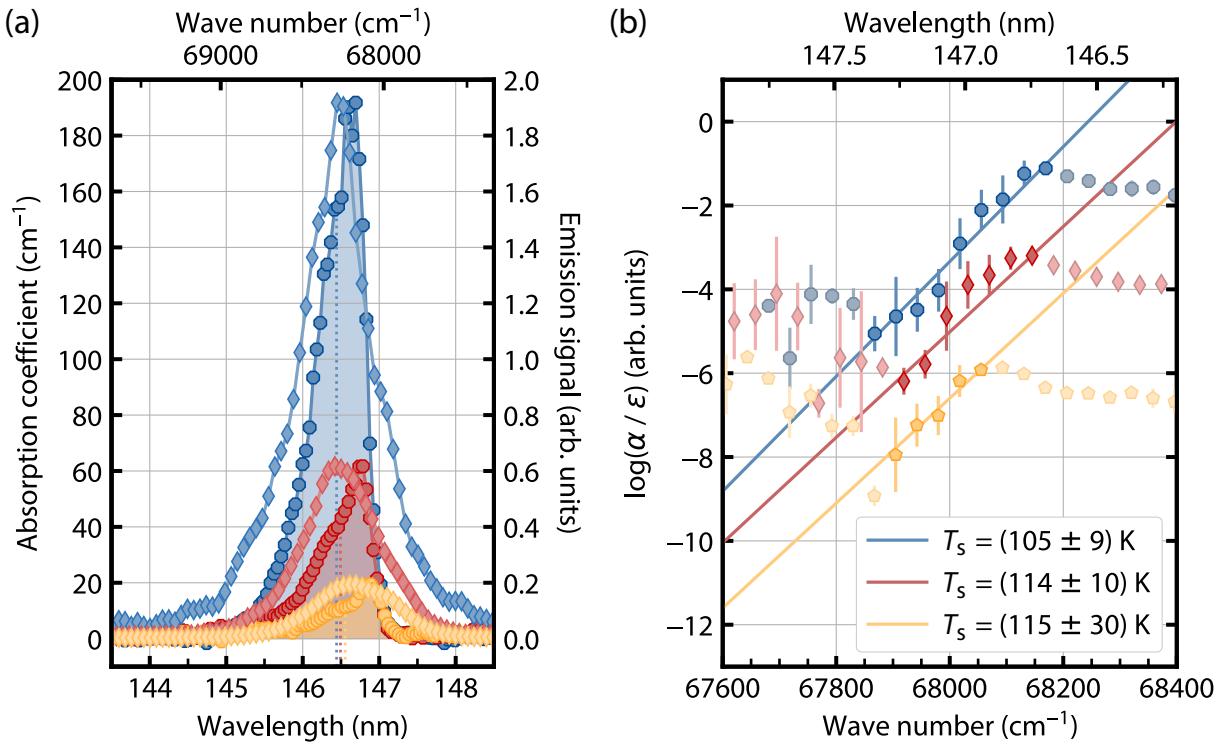

Figure C.2: (a) Qualitatively similar data as in Fig. C.1(a), but with the emission spectra recorded at a longer excitation wavelength of 146.1$\overline{6}$ nm. **(b)** Kennard-Stepanov analysis with the data from (a), analogous to the visualization in Fig. C.1(b).

References

1. Pliny The Elder, *The Natural History, Iris - Two varieties of it* (eds J. Bostock & H. Riley) (Taylor and Francis, London, 1855) – Cited on page 1.
2. C. Burgess & K. Mielenz, *Advances in Standards and Methodology in Spectrophotometry* (Elsevier Science, Amsterdam, 2012) – Cited on page 1.
3. I. Newton, *Opticks* (Dover Press, London, 1704) – Cited on page 1.
4. I. Newton, *Hydrostatics, optics, sound and heat* (Cambridge University Library, 2012) – Cited on page 1.
5. J. Fraunhofer, *Bestimmung des Brechungs- und des Farbenzerstreungs-Vermögens verschiedener Glasarten, in Bezug auf die Vervollkommnung achromatischer Fernröhre,* Annalen der Physik **56**, 264–313 (1817) – Cited on page 1.
6. W. H. Wollaston, *XII. A method of examining refractive and dispersive powers, by prismatic reflection,* Philosophical Transactions of the Royal Society of London **92**, 365–380 (1802) – Cited on page 1.
7. S. Bose, *S.N. Bose: The Man and His Work, Part II: Life, Lectures and Addresses, Miscellaneous Pieces* (S.N. Bose National Centre for Basic Sciences, Calcutta, 1994) – Cited on page 1.
8. Bose, *Plancks Gesetz und Lichtquantenhypothese,* Z. Physik **26**, 178–181 (1924) – Cited on page 1.
9. A. Einstein, *Quantentheorie des einatomigen idealen Gases,* Sitzungsberichte der Preussischen Akademie der Wissenschaften **261** (1924) – Cited on page 1.
10. A. Einstein, *Quantentheorie des einatomigen idealen Gases. Zweite Abhandlung,* Sitzungsberichte der Preussischen Akademie der Wissenschaften **3** (1925) – Cited on page 1.
11. A. Einstein, *Quantum Theory of the Monatomic Ideal Gas. Second Paper,* in *The Collected Papers of Albert Einstein, Volume 14 (English): The Berlin Years: Writings & Correspondence, April 1923–May 1925 (English Translation Supplement)-Documentary Edition* (eds D. K. Buchwald, J. Illy, Z. Rosenkranz, T. Sauer & O. Moses) translated by A. Hentschel & J. N. James (Princeton University Press, Princeton, 2015) – Cited on page 1.
12. T. Maiman, *Stimulated optical radiation in ruby,* Nature **187**, 493–494 (1960) – Cited on page 2.

13. A. Javan, W. R. Bennett & D. R. Herriott, *Population Inversion and Continuous Optical Maser Oscillation in a Gas Discharge Containing a He-Ne Mixture,* Phys. Rev. Lett. **6**, 106–110 (1961) – Cited on page 2.

14. F. Diedrich, J. C. Bergquist, W. M. Itano & D. J. Wineland, *Laser Cooling to the Zero-Point Energy of Motion,* Phys. Rev. Lett. **62**, 403–406 (1989) – Cited on page 2.

15. M. H. Anderson, J. R. Ensher, M. R. Matthews, C. E. Wieman & E. A. Cornell, *Observation of Bose-Einstein Condensation in a Dilute Atomic Vapor,* Science **269**, 198–201 (1995) – Cited on page 2.

16. K. B. Davis, M. O. Mewes, M. R. Andrews, N. J. van Druten, D. S. Durfee, D. M. Kurn & W. Ketterle, *Bose-Einstein Condensation in a Gas of Sodium Atoms,* Phys. Rev. Lett. **75**, 3969–3973 (1995) – Cited on page 2.

17. C. C. Bradley, C. A. Sackett & R. G. Hulet, *Bose-Einstein Condensation of Lithium: Observation of Limited Condensate Number,* Phys. Rev. Lett. **78**, 985–989 (1997) – Cited on page 2.

18. T. Weber, J. Herbig, M. Mark, H.-C. Nägerl & R. Grimm, *Bose-Einstein condensation of cesium,* Science **299**, 232 (2003) – Cited on page 2.

19. T. Fukuhara, S. Sugawa & Y. Takahashi, *Bose-Einstein condensation of an ytterbium isotope,* Phys. Rev. A **76**, 051604 (2007) – Cited on page 2.

20. S. Jochim, M. Bartenstein, A. Altmeyer, G. Hendl, S. Riedl, C. Chin, J. Hecker Denschlag & R. Grimm, *Bose-Einstein condensation of molecules,* Science **302**, 2101–2103 (2003) – Cited on page 2.

21. M. W. Zwierlein, C. A. Stan, C. H. Schunck, S. M. F. Raupach, S. Gupta, Z. Hadzibabic & W. Ketterle, *Observation of Bose-Einstein Condensation of Molecules,* Phys. Rev. Lett. **91**, 250401 (2003) – Cited on page 2.

22. S. Demokritov, V. Demidov, O. Dzyapko, G. Melkov, A. Serga, B. Hillebrands & A. Slavin, *Bose–Einstein condensation of quasi-equilibrium magnons at room temperature under pumping,* Nature **443**, 430 (2006) – Cited on page 2.

23. J. Kasprzak, M. Richard, S. Kundermann, A. Baas, P. Jeambrun, J. M. J. Keeling, F. M. Marchetti, M. H. Szymańska, R. André, J. L. Staehli, V. Savona, P. B. Littlewood, B. Deveaud & L. S. Dang, *Bose-Einstein condensation of exciton polaritons,* Nature **443**, 409–414 (2006) – Cited on page 2.

24. R. Su, S. Ghosh, J. Wang, S. Liu, C. Diederichs, T. C. Liew & Q. Xiong, *Observation of exciton polariton condensation in a perovskite lattice at room temperature,* Nat. Phys. **16**, 301–306 (2020) – Cited on page 2.

25. K. Huang, *Introduction to Statistical Physics* (Taylor & Francis, London, 2001) – Cited on pages 2, 26.

26. M. Planck, *Ueber das Gesetz der Energieverteilung im Normalspectrum,* Annalen der Physik **4**, 533–563 (1901) – Cited on page 2.

27. W. Ketterle, D. S. Durfee & D. M. Stamper-Kurn, *Making, probing and understanding Bose-Einstein condensates,* arXiv:cond-mat/9904034v2 (1999) – Cited on page 2.

28. R. Chiao, *Bogoliubov dispersion relation for a photon fluid: Is this a superfluid?,* Optics Communications **179**, 157 (2000) – Cited on page 2.

29. J. Klärs, F. Vewinger & M. Weitz, *Thermalization of a two-dimensional photonic gas in a 'white wall' photon box,* Nat. Phys. **6**, 512 (2010) – Cited on page 2.

30. J. Klärs, J. Schmitt, F. Vewinger & M. Weitz, *Bose-Einstein condensation of photons in an optical microcavity,* Nature **468**, 545 (2010) – Cited on page 3.

31. T. Damm, J. Schmitt, Q. Liang, D. Dung, F. Vewinger, M. Weitz & J. Klärs, *Calorimetry of a Bose–Einstein-condensed photon gas,* Nat. Commun. **7**, 11340 (2016) – Cited on page 3.

32. J. Schmitt, T. Damm, D. Dung, C. Wahl, F. Vewinger, J. Klärs & M. Weitz, *Spontaneous Symmetry Breaking and Phase Coherence of a Photon Bose-Einstein Condensate Coupled to a Reservoir,* Phys. Rev. Lett. **116**, 033604 (2016) – Cited on page 3.

33. D. Dung, C. Kurtscheid, T. Damm, J. Schmitt, F. Vewinger, M. Weitz & J. Klärs, *Variable potentials for thermalized light and coupled condensates,* Nature Photon. **11**, 565–569 (2017) – Cited on page 3.

34. C. Kurtscheid, D. Dung, E. Busley, F. Vewinger, A. Rosch & M. Weitz, *Thermally condensing photons into a coherently split state of light,* Science **366**, 894–897 (2019) – Cited on page 3.

35. E. Busley, L. E. Miranda, A. Redmann, C. Kurtscheid, K. K. Umesh, F. Vewinger, M. Weitz & J. Schmitt, *Compressibility and the equation of state of an optical quantum gas in a box,* Science **375**, 1403–1406 (2022) – Cited on page 3.

36. J. Marelic & R. A. Nyman, *Experimental evidence for inhomogeneous pumping and energy-dependent effects in photon Bose-Einstein condensation,* Phys. Rev. A **91**, 033813 (2015) – Cited on page 3.

37. S. Greveling, K. L. Perrier & D. van Oosten, *Density distribution of a Bose-Einstein condensate of photons in a dye-filled microcavity,* Phys. Rev. A **98**, 013810 (2018) – Cited on page 3.

38. M. Vretenar, C. Toebes & J. Klärs, *Modified Bose-Einstein condensation in an optical quantum gas,* Nat. Commun. **12**, 5749 (2021) – Cited on page 3.

39. R. C. Schofield, M. Fu, E. Clarke, I. Farrer, A. Trapalis, H. S. Dhar, R. Mukherjee, J. Heffernan, F. Mintert, R. A. Nyman & R. F. Oulton, *Bose-Einstein Condensation of Light in a Semiconductor Quantum Well Microcavity,* arXiv:2306.15314v1 (2023) – Cited on page 3.

40. M. Pieczarka, M. Gebski, A. N. Piasecka, J. A. Lott, A. Pelster, M. Wasiak & T. Czyszanowski, *Bose-Einstein condensation of photons in a vertical-cavity surface-emitting laser,* arXiv:2307.00081v2 (2023) – Cited on page 3.

41. R. Weill, A. Bekker, B. Levit & B. Fischer, *Bose-Einstein condensation of photons in an erbium-ytterbium co-doped fiber cavity,* Nat. Commun. **10**, 747 (2019) – Cited on page 3.

42. A. E. Siegman, *Lasers* (University science books, Sausalito, 1986) – Cited on page 3.

43. R. Sauerbrey, *Ultraviolet, Vacuum-ultraviolet, and X-ray lasers,* in *Electro-Optics Handbook* (eds R. Waynant & M. Ediger) 2nd ed. (McGraw-Hill, 2000) – Cited on page 3.

44. C. Wahl, R. Brausemann, J. Schmitt, F. Vewinger, S. Christopoulos & M. Weitz, *Absorption spectroscopy of xenon and ethylene–noble gas mixtures at high pressure: towards Bose–Einstein condensation of vacuum ultraviolet photons,* Appl. Phys. B **122**, 296 (2016) – Cited on page 3.

45. C. Wahl, M. Hoffmann, T. vom Hövel, F. Vewinger & M. Weitz, *Vacuum-ultraviolet absorption and emission spectroscopy of gaseous, liquid, and supercritical xenon,* Phys. Rev. A **103**, 022831 (2021) – Cited on page 3.

46. C. Wahl, *Absorptions- und Emissionsspektroskopie an superkritischem, flüssigem und gasförmigem Xenon im Vakuum-Ultravioletten Spektralbereich,* PhD thesis (Rheinische Friedrich-Wilhelms-Universität Bonn, 2019) – Cited on pages 3, 20, 21, 29, 30, 33, 34, 44, 51.

47. J. Klärs, *Bose-Einstein-Kondensation von paraxialem Licht,* PhD thesis (Rheinische Friedrich-Wilhelms-Universität Bonn, 2011) – Cited on pages 5, 11, 19.

48. L. De Broglie, *Recherches sur la théorie des quanta (Research on the Theory of the Quanta),* PhD thesis (1924) – Cited on page 8.

49. C. Kittel & H. Kroemer, *Thermal Physics* 2nd ed. (W. H. Freeman and Company, New York, 2002) – Cited on page 9.

50. J. Lakowicz, *Principles of Fluorescence Spectroscopy* 3rd ed. (Springer US, New York, 2006) – Cited on pages 12, 13, 25.

51. G. G. Stokes, *XXX. On the change of refrangibility of light,* Phil. Trans R. Soc. **142**, 463–562 (1852) – Cited on page 12.

52. M. Kasha, *Characterization of electronic transitions in complex molecules,* Discuss. Faraday Soc. **9**, 14–19 (1950) – Cited on page 13.

53. E. H. Kennard, *On The Thermodynamics of Fluorescence,* Phys. Rev. **11**, 29–38 (1918) – Cited on page 14.

54. B. Stepanov, *Universal relation between the absorption spectra and luminescence spectra of complex molecules,* Dokl. Akad. Nauk SSSR. **112**, 839 (1957) – Cited on page 14.

55. R. Martin & R. Quimby, *Experimental evidence of the validity of the McCumber theory relating emission and absorption for rare-earth glasses,* J. Opt. Soc. Am. B **23**, 1770–1775 (2006) – Cited on pages 14, 15.

56. D. A. Sawicki & R. S. Knox, *Universal relationship between optical emission and absorption of complex systems: An alternative approach,* Phys. Rev. A **54**, 4837–4841 (1996) – Cited on page 14.

57. R. van Metter & R. Knox, *On the relation between absorption and emission spectra of molecules in solution,* Chemical Physics **12**, 333 (1976) – Cited on page 15.

58. R. Knox, *Excited-State Equilibration and the Fluorescence-Absorption Ratio,* Acta Physica Polonica A **95**, 85 (1999) – Cited on page 15.

59. R. S. Knox, J. S. Brown, P. D. Laible & M. F. Talbot, *Part of the fluorescence of chlorophyll a may originate in excited triplet states,* Photosynthesis research **60**, 165–177 (1999) – Cited on page 15.

60. T. Ockenfels, P. Roje, T. vom Hövel, F. Vewinger & M. Weitz, *Spectroscopy of high-pressure rubidium-noble-gas mixtures,* Phys. Rev. A **106**, 012815 (2022) – Cited on page 15.

61. Y. B. Band & D. F. Heller, *Relationships between the absorption and emission of light in multilevel systems,* Phys. Rev. A **38**, 1885–1895 (1988) – Cited on page 15.

62. D. P. Landau & K. Binder, *A Guide to Monte Carlo Simulations in Statistical Physics* 3rd ed. (Cambridge University Press, Cambridge, 2009) – Cited on page 16.

63. H. Du, R.-C. A. Fuh, J. Li, A. Corkan & J. Lindsey, *PhotochemCAD: A computer-aided design and research tool in photochemistry,* Photochemistry and Photobiology **68**, 141 (1998) – Cited on pages 16, 20.

64. E. Busley, *Investigation of Paraxial Light Concentration and Homogeneously Trapped Two-Dimensional Optical Quantum Gases,* PhD thesis (Rheinische Friedrich-Wilhelms-Universität Bonn, 2022) – Cited on page 19.

65. D. Magde, R. Wong & P. Seybold, *Fluorescence Quantum Yields and Their Relation to Lifetimes of Rhodamine 6G and Fluorescein in Nine Solvents: Improved Absolute Standards for Quantum Yields,* Photochemistry and Photobiology **75**, 327 (2007) – Cited on page 20.

66. Laseroptik GmbH, *Reflektivitätsdiagramm B-17957,* 2021 – Cited on page 20.

67. W. Demtröder, *Experimentalphysik 3: Atome, Moleküle und Festkörper* 2nd ed. (Springer, Berlin, Heidelberg, 2000) – Cited on pages 21, 24, 25.

68. S. Wang, K. Hou & H. Heinz, *Accurate and compatible force fields for molecular oxygen, nitrogen, and hydrogen to simulate gases, electrolytes, and heterogeneous interfaces,* J. Chem. Theory Comput. **17**, 5198–5213 (2021) – Cited on page 22.

69. A. D. Becke, *Density-functional thermochemistry. II. The effect of the Perdew–Wang generalized-gradient correlation correction,* J. Chem. Phys. **97**, 9173–9177 (1992) – Cited on page 22.

70. T. A. Halgren, *The representation of van der Waals (vdW) interactions in molecular mechanics force fields: potential form, combination rules, and vdW parameters,* J. Am. Chem. Soc. **114**, 7827–7843 (1992) – Cited on page 22.

71. M. Selg, *Visualization of rigorous sum rules for Franck-Condon factors: spectroscopic applications to Xe_2,* Journal of Molecular Spectroscopy **220**, 187–200 (2003) – Cited on pages 22, 28.

72. N. Böwering, M. Bruce & J. Keto, *Collisional deactivation of two-photon laser excited xenon $5p^5 6p$. I. State-to-state reaction rates,* J. Chem. Phys. **84**, 709–714 (1986) – Cited on pages 22, 28, 31.

73. P. M. Morse & E. C. G. Stueckelberg, *Diatomic Molecules According to the Wave Mechanics I: Electronic Levels of the Hydrogen Molecular Ion,* Phys. Rev. **33**, 932–947 (1929) – Cited on page 24.

74. P. M. Morse, *Diatomic Molecules According to the Wave Mechanics. II. Vibrational Levels,* Phys. Rev. **34**, 57–64 (1929) – Cited on page 24.

75. M.-C. Castex, *Experimental determination of the lowest excited Xe_2 molecular states from VUV absorption spectra,* J. Chem. Phys. **74**, 759–771 (1981) – Cited on page 25.

76. J. Wieser, A. Ulrich, A. Fedenev & M. Salvermoser, *Novel pathways to the assignment of the third rare gas excimer continua,* Optics Communications **173**, 233–245 (2000) – Cited on page 26.

77. E. W. Lemmon, I. H. Bell, M. L. Huber & M. O. McLinden, *Thermophysical Properties of Fluid Systems,* in *NIST Chemistry WebBook, Standard Reference Database Number 69* (eds P. Linstrom & W. Mallard) (National Institute of Standards and Technology, Gaithersburg MD, 2023) – Cited on pages 26, 27, 39.

78. W. Ramsay, *Sir William Ramsay – Nobel Lecture,* `https://www.nobelprize.org/prizes/chemistry/1904/ramsay/facts/`, Nobel Prize Outreach AB, Sept. 4, 2023 – Cited on page 26.

79. A. G. W. Cameron, *Abundances of the elements in the solar system,* Space Sci. Rev. **15**, 121–146 (1973) – Cited on page 26.

80. S. S. Shcheka & H. Keppler, *The origin of the terrestrial noble-gas signature,* Nature **490**, 531–534 (2012) – Cited on page 26.

81. P. Di Gangi, *The Xenon Road to Direct Detection of Dark Matter at LNGS: The XENON Project,* Universe **7** (2021) – Cited on page 26.

82. M. Patterson, J. Foster, T. Haag, V. Rawlin, G. Soulas & R. Roman, *NEXT: NASA's Evolutionary Xenon Thruster,* American Institute of Aeronautics and Astronautics (2002) – Cited on page 26.

83. Z. Jin, O. Piazza, D. Ma, G. Scarpati & E. De Robertis, *Xenon anesthesia and beyond: pros and cons,* Minerva anestesiologica **85**, 83–89 (2019) – Cited on page 26.

84. T. Doiron, *20 °C—A Short History of the Standard Reference Temperature for Industrial Dimensional Measurements,* Journal of research of the National Institute of Standards and Technology **112**, 1 (2007) – Cited on page 26.

85. Wolfram Research Inc., *Mathematica, Version 12.1,* Query: "Phase diagram of xenon", Champaign IL, 2023 – Cited on page 27.

86. J. Sansonetti & W. Martin, *Handbook of Basic Atomic Spectroscopic Data,* in *NIST Chemistry WebBook, Standard Reference Database Number 108* (National Institute of Standards and Technology, Quantum Measurement Division, PML, 2023) – Cited on pages 27, 28, 47, 51, 56, 57.

87. M. Castex, *Absorption spectra of Xe–rare gas mixtures in the far uv region (1150–1500 Å): High resolution analysis and first quantitative absorption measurements,* J. Chem. Phys. **66**, 3854–3865 (1977) – Cited on pages 29, 31, 32, 65.

88. G. Nowak & J. Fricke, *The heteronuclear excimers ArKr*, ArXe* and KrXe,* J. Phys. B: Atom. Mol. Phys. **18**, 1355 (1985) – Cited on pages 29, 32, 65.

89. B. Borovich, V. Zuev & D. Stavrovsky, *Pressure-induced ultraviolet absorption in rare gases: Absorption coefficients for mixtures of Xe and Ar at pressures up to 40 atm in the vicinity of 147 nm,* Journal of Quantitative Spectroscopy and Radiative Transfer **13**, 1241–1249 (1973) – Cited on pages 30, 62.

90. J. B. Gerardo & A. W. Johnson, *Photoattenuation in the extreme red wings of Xe and Kr resonant lines,* Phys. Rev. A **10**, 1204–1211 (1974) – Cited on page 30.

91. B. L. Borovich, V. Zuev & D. Stavrovskii, *A contribution to the problem of an optically pumped ultraviolet Xe_2 laser: photoluminescence spectrum and quantum efficiency of gaseous xenon,* Soviet Journal of Quantum Electronics **4**, 1138 (1975) – Cited on page 30.

92. K. Fujii, Y. Endo, Y. Torigoe, S. Nakamura, T. Haruyama, K. Kasami, S. Mihara, K. Saito, S. Sasaki & H. Tawara, *High-accuracy measurement of the emission spectrum of liquid xenon in the vacuum ultraviolet region,* Nuclear Instruments and Methods in Physics Research Section A: Accelerators, Spectrometers, Detectors and Associated Equipment **795**, 293–297 (2015) – Cited on page 30.

93. W. Gornik, S. Kindt, E. Matthias & D. Schmidt, *Two-photon excitation of xenon atoms and dimers in the energy region of the $5p^5 6p$ configuration,* J. Chem. Phys. **75**, 68–74 (1981) – Cited on pages 31, 56.

94. T. D. Raymond, N. Böwering, C.-Y. Kuo & J. W. Keto, *Two-photon laser spectroscopy of xenon collision pairs,* Phys. Rev. A **29**, 721–734 (1984) – Cited on pages 31, 56.

95. N. Böwering, M. Bruce & J. Keto, *Collisional deactivation of two-photon laser excited xenon $5p^5 6p$. II. Lifetimes and total quench rates,* J. Chem. Phys. **84**, 715–726 (1986) – Cited on page 31.

96. C. A. Whitehead, H. Pournasr, M. R. Bruce, H. Cai, J. Kohel, W. B. Layne & J. W. Keto, *Deactivation of two-photon excited $Xe(5p^5 6p,\ 6p',\ 7p)$ and $Kr(4p^5 5p)$ in xenon and krypton,* J. Chem. Phys. **102**, 1965–1980 (1995) – Cited on page 31.

97. W. Gornik, S. Kindt, E. Matthias, H. Rinneberg & D. Schmidt, *Off-Resonant E2 Transition Observed in Two-Photon Absorption in Xe I,* Phys. Rev. Lett. **45**, 1941–1944 (1980) – Cited on page 31.

98. W. Gornik, E. Matthias & D. Schmidt, *Two-photon excitation of the lowest g states in Xe_2,* J. Phys. B: Atom. Mol. Phys. **15**, 3413 (1982) – Cited on page 31.

99. J. C. Miller, *Two-photon resonant multiphoton ionization and stimulated emission in krypton and xenon,* Phys. Rev. A **40**, 6969–6976 (1989) – Cited on page 31.

100. S. Kröll & W. K. Bischel, *Two-photon absorption and photoionization cross-section measurements in the $5p^5 6p$ configuration of xenon,* Phys. Rev. A **41**, 1340–1349 (1990) – Cited on page 31.

101. J. Keto, H. Cai, M. Kykta, C. Lei, T. Möller & G. Zimmerer, *Two-photon spectroscopy of xenon dimers in supersonic jets,* J. Chem. Phys. **107**, 6080–6093 (1997) – Cited on page 31.

102. M. Stellpflug, M. Johnsson, I. Petrov & T. Halfmann, *Investigation of auto-ionizing states in xenon by resonantly enhanced multi-photon ionization,* The European Physical Journal D-Atomic, Molecular, Optical and Plasma Physics **23**, 35–42 (2003) – Cited on page 31.

103. M. McCann, C. Chen & M. Payne, *Two-photon (vacuum ultraviolet + visible) spectroscopy of argon, krypton, xenon, and molecular hydrogen,* J. Chem. Phys. **89**, 5429–5441 (1988) – Cited on pages 31, 43.

104. M. Meyer, M. Gisselbrecht, A. Marquette, C. Delisle, M. Larzillière, I. Petrov, N. Demekhina & V. Sukhorukov, *Two-colour studies of the even-parity autoionization series $5p^5_{1/2} nl'(l = p,\ f)$ in atomic xenon,* J. Phys. B: At. Mol. Opt. Phys. **38**, 285 (2005) – Cited on page 31.

105. Y. Salamero, A. Birot, H. Brunet, H. Dijols, J. Galy, P. Millet & J. Montagne, *Energy transfer kinetics of the VUV emissions for Kr–Xe mixtures,* J. Chem. Phys. **74**, 288–296 (1981) – Cited on page 32.

106. F. Marchal, P. Berejny, N. Sewraj, Y. Salamero & P. Millet, *Energy transfers in Kr–Xe mixtures following selective multiphotonic excitation of Kr ($^3P_1$). Temporal analysis in Kr–Xe mixtures,* J. Phys. B: At. Mol. Opt. Phys. **37**, 1279 (2004) – Cited on page 32.

107. G. Ledru, F. Marchal, N. Merbahi, J. Gardou & N. Sewraj, *Study of the formation and decay of KrXe* excimers at room temperature following selective excitation of the xenon 6s states,* J. Phys. B: At. Mol. Opt. Phys. **40**, 1651 (2007) – Cited on page 32.

108. H. Brunet, A. Birot, H. Dijols, J. Galy, P. Millet & Y. Salamero, *Spectroscopic and kinetic analysis of the VUV emissions of argon and argon-xenon mixtures. II. Energy transfer in Ar-Xe mixtures,* J. Phys. B: Atom. Mol. Phys. **15**, 2945 (1982) – Cited on page 32.

109. P. Millet, A. Birot, H. Brunet, H. Dijolis, J. Galy & Y. Salamero, *Spectroscopic and kinetic analysis of the VUV emissions of argon and argon-xenon mixtures. I. Study of pure argon,* J. Phys. B: Atom. Mol. Phys. **15**, 2935 (1982) – Cited on page 32.

110. W. Wieme & J. Lenaerts, *Quenching of excited Xe* ($^3P_2$, $^3P_1$, $^1P_1$) states in a neon–xenon mixture,* J. Chem. Phys. **72**, 2708–2712 (1980) – Cited on page 32.

111. D. E. Freeman, K. Yoshino & Y. Tanaka, *Vacuum ultraviolet absorption spectra of binary rare gas mixtures and the properties of heteronuclear rare gas van der Waals molecules,* J. Chem. Phys. **67**, 3462–3481 (1977) – Cited on pages 32, 78.

112. G. N. Gerasimov, *Optical spectra of binary rare-gas mixtures,* Physics-Uspekhi **47**, 149 (2004) – Cited on page 32.

113. K. Watanabe, E. C. Y. Inn & M. Zelikoff, *Absorption Coefficients of Oxygen in the Vacuum Ultraviolet,* J. Chem. Phys. **21**, 1026–1030 (1953) – Cited on page 33.

114. K. Watanabe & M. Zelikoff, *Absorption Coefficients of Water Vapor in the Vacuum Ultraviolet,* J. Opt. Soc. Am. **43**, 753–755 (1953) – Cited on page 33.

115. A. Zaidel & E. Shreider, *Vacuum Ultraviolet Spectroscopy* (Ann Arbor-Humphrey Science Publishers, Ann Arbor, London, 1970) – Cited on page 33.

116. R. Brausemann, *Vacuum Ultraviolet Spectroscopy of High Pressure Atomic and Molecular Gases,* Master thesis (Rheinische Friedrich-Wilhelms-Universität Bonn, 2016) – Cited on page 33.

117. M. Hoffmann, *Vacuum Ultraviolet Spectroscopy of Gaseous, Liquid and Supercritical Xenon,* Master thesis (Rheinische Friedrich-Wilhelms-Universität Bonn, 2018) – Cited on page 34.

118. W. Graf, *Private Kommunikation,* Feinmechanische Werkstatt am Institut für Angewandte Physik der Universität Bonn, 2023 – Cited on page 34.

119. Korth Kristalle GmbH, *Magnesiumfluorid (MgF_2),* `https://www.korth.de/material/detail/Magnesiumfluorid`, Aug. 24, 2023 – Cited on page 35.

120. Korth Kristalle GmbH, *Saphir (Al_2O_3),* `https://www.korth.de/material/detail/Saphir`, Aug. 24, 2023 – Cited on page 35.

121. AirLiquide, *Xenon N48 Halogenfrei,* `https://mygas.airliquide.de/catalog-gas-products/xenon-n48-halogenfrei`, Aug. 21, 2023 – Cited on page 36.

122. J. A. Giordmaine & R. C. Miller, *Tunable Coherent Parametric Oscillation in $LiNbO_3$ at Optical Frequencies,* Phys. Rev. Lett. **14**, 973–976 (1965) – Cited on page 39.

123. J. M. Gray, J. Bossert, Y. Shyur, B. Saarel, T. C. Briles & H. Lewandowski, *Characterization of a vacuum ultraviolet light source at 118 nm,* J. Chem. Phys. **154** (2021) – Cited on pages 41, 42.

124. R. Miles & S. Harris, *Optical third-harmonic generation in alkali metal vapors,* IEEE Journal of Quantum Electronics **9**, 470–484 (1973) – Cited on page 41.

125. G. Bjorklund, *Effects of focusing on third-order nonlinear processes in isotropic media,* IEEE Journal of Quantum Electronics **11**, 287–296 (1975) – Cited on page 41.

126. J. F. Ward & G. H. C. New, *Optical Third Harmonic Generation in Gases by a Focused Laser Beam,* Phys. Rev. **185**, 57–72 (1969) – Cited on page 41.

127. D. Meschede, *Optik, Licht und Laser* 3rd ed. (Vieweg + Teubner, Wiesbaden, 2008) – Cited on pages 42, 44.

128. M. J. Dodge, *Refractive properties of magnesium fluoride,* Appl. Opt. **23**, 1980–1985 (1984) – Cited on page 44.

129. P. Laporte, N. Damany & H. Damany, *Pulsed-laser-generated rare-gas plasma as a light source in the vacuum ultraviolet,* Opt. Lett. **12**, 987–989 (1987) – Cited on pages 46, 77.

130. M. Kaku, T. Higashiguchi, S. Kubodera & W. Sasaki, *Vacuum ultraviolet argon excimer production by use of an ultrashort-pulse high-intensity laser,* Phys. Rev. A **68**, 023803 (2003) – Cited on page 47.

131. T. M. Di Palma & A. Borghese, *Characterization of a UV–VUV light source based on a gas-target ns-laser-produced plasma,* Nuclear Instruments and Methods in Physics Research Section B: Beam Interactions with Materials and Atoms **254**, 193–199 (2007) – Cited on page 47.

132. M. Kaku, Y. Sato & S. Kubodera, *Quasi-point incoherent ArF* excimer emission source at 193 nm using a laser-produced plasma,* Appl. Phys. B **107**, 85–89 (2012) – Cited on page 47.

133. C. Palmer, *Diffraction Grating Handbook–Richardson Gratings* 7th ed. (Newport Corporation, Rochester, 2014) – Cited on page 49.

134. G. Grynberg & B. Cagnac, *Doppler-free multiphotonic spectroscopy,* Reports on Progress in Physics **40**, 791 (1977) – Cited on page 51.

135. K. Bonin & T. McIlrath, *Two-photon electric-dipole selection rules,* J. Opt. Soc. Am. B **1**, 52–55 (1984) – Cited on page 51.

136. M. R. Bruce, W. B. Layne, C. A. Whitehead & J. W. Keto, *Radiative lifetimes and collisional deactivation of two-photon excited xenon in argon and xenon,* J. Chem. Phys. **92**, 2917–2926 (1990) – Cited on page 52.

137. M. Göppert-Mayer, *Über Elementarakte mit zwei Quantensprüngen,* Annalen der Physik **401**, 273–294 (1931) – Cited on page 54.

138. N. Böwering, C.-Y. Kuo, T. Raymond & J. Keto, *Spectral Line Shapes from Two-Photon Excitation of Xenon,* in *Spectral line shapes* (ed K. Burnett) 927–943 (De Gruyter, Berlin, Boston, 1983) – Cited on page 56.

139. J. Paul, Y. Kaneda, T.-L. Wang, C. Lytle, J. V. Moloney & R. J. Jones, *Doppler-free spectroscopy of mercury at 253.7 nm using a high-power, frequency-quadrupled, optically pumped external-cavity semiconductor laser,* Opt. Lett. **36**, 61–63 (2011) – Cited on page 58.

140. S. Sadegh, M.-H. Yang, C. G. L. Ferri, M. Thunemann, P. A. Saisan, A. Devor & Y. Fainman, *Measurement of the relative non-degenerate two-photon absorption cross-section for fluorescence microscopy,* Opt. Express **27**, 8335–8347 (2019) – Cited on page 58.

141. M. Kubista, R. Sjöback, S. Eriksson & B. Albinsson, *Experimental correction for the inner-filter effect in fluorescence spectra,* Analyst **119**, 417–419 (1994) – Cited on pages 66, 68.

142. U. Vogl, *Kollektive Effekte und stoßinduzierte Redistributionskühlung in dichten atomaren Gasen,* PhD thesis (Rheinische Friedrich-Wilhelms-Universität Bonn, 2010) – Cited on page 72.

143. H. K. Hughes, *Beer's law and the optimum transmittance in absorption measurements,* Appl. Opt. **2**, 937–945 (1963) – Cited on page 78.

144. N. Allard & J. Kielkopf, *The effect of neutral nonresonant collisions on atomic spectral lines,* Rev. Mod. Phys. **54**, 1103–1182 (1982) – Cited on page 80.

145. F. Huybrechts, *Two-photon spectroscopy of gaseous and supercritical xenon and development of a high pressure optical microcavity for VUV photon condensation,* Master thesis (Rheinische Friedrich-Wilhelms-Universität Bonn, 2021) – Cited on page 87.

146. T. Ockenfels, F. Vewinger & M. Weitz, *Sapphire optical viewport for high pressure and temperature applications,* Rev. Sci. Instrum. **92**, 065109 (2021) – Cited on page 87.

147. W. Graf, *Private Kommunikation,* Feinmechanische Werkstatt am Institut für Angewandte Physik der Universität Bonn, 2021 – Cited on page 88.

148. J. Yang, *Schrittmotor-basierte Steuerung eines Hochdruck-Resonators für Experimente zur Photonen Bose-Einstein-Kondensation,* Bachelor thesis (Rheinische Friedrich-Wilhelms-Universität Bonn, 2022) – Cited on page 88.

149. G. Racah, *On a New Type of Vector Coupling in Complex Spectra,* Phys. Rev. **61**, 537–537 (1942) – Cited on page 89.

150. C. Haridass, H. Major, P. Misra & X. Han, *Laser Optogalvanic Spectroscopy of Discharge Plasmas in the Ultraviolet Region,* in *Ultraviolet spectroscopy and UV lasers* (eds P. Misra & M. A. Dubinskii) (Marcel Dekker, New York, 2002) – Cited on page 89.

Danksagung

Ich möchte mich zum Schluss dieser Arbeit bei allen Personen bedanken, die das Entstehen selbiger möglich gemacht haben. Besonderer Dank gilt

- Prof. Dr. Martin Weitz für die Möglichkeit, an diesem tollen und immer wieder faszinierenden Experiment zu arbeiten,
- Prof. Dr. Stefan Linden für die unkomplizierte Übernahme der Zweitbegutachtung der Dissertation,
- Priv.-Doz. Dr. Stefan Förste und Prof. Dr. Olav Schiemann für die Komplettierung der Promotionskommission,
- Dr. Frank Vewinger für seine beständige Unterstützung bei fachlichen Problemen aller Art,
- Dr. Christian Wahl, der mir „sein“ Experiment überließ und mir insbesondere in der Anfangsphase der Promotion viel Hilfreiches darüber mit auf den Weg gegeben hat,
- Dr. Till Ockenfels, mit dem ich über die Jahre hinweg das Labor geteilt habe und der für jede Fachsimpelei zur Verfügung stand,
- Eric Boltersdorf, der sich im Rahmen seiner Masterarbeit bestens mit dem Experiment vertraut gemacht hat und in dessen Hände ich dieses nun voller Zuversicht übergebe,
- Marvin Hoffmann und Franz Huybrechts, mit denen ich im Rahmen ihrer Masterarbeiten am Experiment zusammenarbeiten durfte,
- den Mitarbeitenden aus der Verwaltung und den Werkstätten des Instituts, welche mir viel Arbeit abgenommen und mich bei allen organisatorischen und technischen Herausforderungen unterstützt haben,
- meinen Eltern Rüdiger und Sigrid für die Begleitung auf meinem bisherigen Lebensweg,
- meiner wunderbaren Freundin Karo. Danke für deine Geduld und deine immerwährende moralische Unterstützung, die so manchen anstrengenden Tag im Labor gleich weniger schlimm gemacht haben.